DNA Origami Nanoforks: A Platform for Cytochrome C Single Molecule Surface Enhanced Raman Spectroscopy

Amr Mostafa

Doctoral Thesis

In fulfillment of the requirements for the degree

Doctor rerum naturalium (Dr. rer. Nat.)

In the scientific discipline "Physical Chemistry"

Submitted to the Faculty of Science

Of the University of Potsdam

Potsdam, April 2024

Abstract

This thesis presents a comprehensive exploration of the application of DNA origami nanofork antennas (DONAs) in the field of spectroscopy, with a particular focus on the structural analysis of Cytochrome C (CytC) at the single-molecule level. The research encapsulates the design, optimization, and application of DONAs in enhancing the sensitivity and specificity of Raman spectroscopy, thereby offering new insights into protein structures and interactions.

The initial phase of the study involved the meticulous optimization of DNA origami structures. This process was pivotal in developing nanoscale tools that could significantly enhance the capabilities of Raman spectroscopy. The optimized DNA origami nanoforks, in both dimer and aggregate forms, demonstrated an enhanced ability to detect and analyze molecular vibrations, contributing to a more nuanced understanding of protein dynamics.

A key aspect of this research was the comparative analysis between the dimer and aggregate forms of DONAs. This comparison revealed that while both configurations effectively identified oxidation and spin states of CytC, the aggregate form offered a broader range of detectable molecular states due to its prolonged signal emission and increased number of molecules. This extended duration of signal emission in the aggregates was attributed to the collective hotspot area, enhancing overall signal stability and sensitivity.

Furthermore, the study delved into the analysis of the Amide III band using the DONA system. Observations included a transient shift in the Amide III band's frequency, suggesting dynamic alterations in the secondary structure of CytC. These shifts, indicative of transitions between different protein structures, were crucial in understanding the protein's functional mechanisms and interactions.

The research presented in this thesis not only contributes significantly to the field of spectroscopy but also illustrates the potential of interdisciplinary approaches in biosensing. The use of DNA origami-based systems in spectroscopy has opened new avenues for research, offering a detailed and comprehensive understanding of protein structures and interactions. The insights gained from this research are expected to have lasting implications in scientific fields ranging from drug development to the study of complex biochemical pathways. This thesis thus stands as a testament to the power of integrating nanotechnology, biochemistry, and spectroscopic techniques in addressing complex scientific questions.

Zusammenfassung

Diese Dissertation präsentiert eine umfassende Untersuchung der Anwendung von DNA-Origami-Nanogabelantennen (DONAs) im Bereich der Spektroskopie, mit einem besonderen Fokus auf der strukturellen Analyse von Cytochrom C (CytC) auf Einzelmolekülebene. Die Forschung umfasst das Design, die Optimierung und die Anwendung von DONAs zur Steigerung der Sensitivität und Spezifität der Raman-Spektroskopie und bietet somit neue Einblicke in Proteinstrukturen und -interaktionen.

Die erste Phase der Studie beinhaltete die sorgfältige Optimierung von DNA-Origami-Strukturen. Dieser Prozess war entscheidend für die Entwicklung von Nanowerkzeugen, die die Fähigkeiten der Raman-Spektroskopie erheblich verbessern könnten. Die optimierten DNA-Origami-Nanogabeln, sowohl in Dimer- als auch in Aggregatform, zeigten eine verbesserte Fähigkeit, molekulare Schwingungen zu detektieren und zu analysieren, was zu einem nuancierteren Verständnis der Proteindynamik beitrug.

Ein Schlüsselaspekt dieser Forschung war die vergleichende Analyse zwischen den Dimer- und Aggregatformen von DONAs. Dieser Vergleich zeigte, dass beide Konfigurationen effektiv Oxidations- und Spin-Zustände von CytC identifizieren konnten, wobei die Aggregatform aufgrund ihrer längeren Signalemission und der erhöhten Anzahl von Molekülen ein breiteres Spektrum an detektierbaren molekularen Zuständen bot. Die verlängerte Dauer der Signalemission in den Aggregaten wurde auf den kollektiven Hotspot-Bereich zurückgeführt, der die Gesamtsignalstabilität und -empfindlichkeit erhöhte.

Darüber hinaus ging die Studie auf die Analyse der Amid-III-Bande unter Verwendung des DONA-Systems ein. Zu den Beobachtungen gehörte eine vorübergehende Verschiebung der Frequenz der Amid-III-Bande, was auf dynamische Veränderungen in der Sekundärstruktur von CytC hindeutete. Diese Verschiebungen, die auf Übergänge zwischen verschiedenen Proteinstrukturen hindeuteten, waren entscheidend für das Verständnis der funktionellen Mechanismen und Interaktionen des Proteins.

Die in dieser Dissertation präsentierte Forschung leistet nicht nur einen bedeutenden Beitrag zum Gebiet der Spektroskopie, sondern veranschaulicht auch das Potenzial interdisziplinärer Ansätze in der Biosensorik. Der Einsatz von DNA-Origami-basierten Systemen in der Spektroskopie hat neue Wege für die Forschung eröffnet und bietet ein detailliertes und umfassendes Verständnis von Proteinstrukturen und -interaktionen. Die aus dieser Forschung gewonnenen Erkenntnisse werden voraussichtlich langfristige Auswirkungen auf wissenschaftliche Bereiche haben, die von der Arzneimittelentwicklung bis hin zur Untersuchung komplexer biochemischer Prozesse reichen. Diese Dissertation steht somit als Zeugnis für die Kraft der Integration von Nanotechnologie, Biochemie und spektroskopischen Techniken bei der Beantwortung komplexer wissenschaftlicher Fragen.

Contents

List of Abbreviations

2D	2 Dimensions
3D	3 Dimensions
A	Adenine
AFM	Atomic Force Microscopy
ATP	Adenosine Triphosphate
Au	Gold
AuNP	Gold Nanoparticles
C	Cytosine
CDA	Coupled Dipole Approximation
DDA	Discrete Dipole Approximation
DNA	Deoxyribonucleic Acid
DONA	DNA Origami Nanofork Antenna
DTPA	Dithiol Phosphoramidite
DX	DNA Double-Crossover
EDTA	Ethylenediaminetetraacetic Acid
FDTD	Finite-Difference Time-Domain
FRET	Förster Resonance Energy Transfer
G	Guanine
HS	High Spin
LS	Low Spin
LSPR	Localized Surface Plasmon Resonance
MWCO	Molecular Weight Cut-off
NF	NanoFork
NP	Nanoparticles
NR	Normal Raman

POC	Point of Care
RNA	Ribonucleic Acid
RT	Room Temperature
SARS-COV-2	Severe Acute Respiratory Syndrome Coronavirus 2
SEF	Surface-Enhanced Fluorescence
SERS	Surface-Enhanced Raman Scattering
SM	Single Molecule
SMSERS	Single Molecule Surface-Enhanced Raman Scattering
T	Thymine
TAE	Tris Base, Acetic Acid, and EDTA Buffer
TCEP	Tris (2-Carboxyethyl) Phosphine
UV	Ultraviolet
UVRR	Ultraviolet Resonance Raman

1. Introduction

The journey of nanotechnology began with Richard Feynman's often-quoted 1959 lecture, "There's Plenty of Room at the Bottom", where he envisaged the potential for manipulating matter at the atomic and molecular scale[1]. Nanotechnology, coined later by Norio Taniguchi in 1974[2], encompassed Feynman's vision of engaging matter at the nanoscale, typically between 1 and 100 nanometers. This diverse field has extended its tendrils into numerous scientific disciplines, producing an array of innovations that have revolutionized our understanding of the physical world. Even now, as we stand over six decades after Feynman's lecture, we continue to explore the depths of that "room at the bottom", incessantly probing the limits of our knowledge and abilities.

Nanotechnology has emerged as a rapidly growing multidisciplinary field, encompassing various scientific and engineering disciplines, and unlocking a wide range of applications in medicine, electronics, energy production, and environmental protection. The development of nanoscale materials and devices has been facilitated by significant advances in fabrication techniques, such as top-down approaches like lithography[3] and bottom-up methods like self-assembly[4]. These methods enable precise control over material properties and structures, leading to novel devices and materials with unique characteristics and functions[5].

As nanotechnology has evolved, so too has the field of single-molecule measurements, which offer unprecedented insights into the behavior, structure, and function of individual molecules[6]. Single-molecule techniques, such as fluorescence spectroscopy, atomic force spectroscopy, and Raman spectroscopy[7], have revolutionized biophysics and chemistry by revealing the stochastic nature of molecular processes and uncovering rare events and transient states that would be masked in ensemble-based measurements[8]. These techniques have been particularly valuable in studying biological systems, providing a more detailed understanding of molecular interactions, conformational changes, and the impact of environmental factors on biomolecular function[9].

One of the most exciting developments in nanotechnology is the invention of Deoxyribonucleic acid (DNA) origami, a technique that leverages the unique properties of DNA to create custom-designed nanostructures and nanodevices[10,11]. DNA origami relies on the self-assembly of a long single-stranded DNA scaffold, which is folded into a desired shape by hybridization with a set of shorter synthetic "staple" strands[12]. The programmable nature, structural stability, and biocompatibility of DNA origami have opened up numerous applications[13]. DNA origami has been particularly valuable in the development of biosensors, allowing researchers to create highly specific and sensitive devices for detecting a variety of target molecules[14].

A fascinating intersection of these advancements is the study of single-molecule surface-enhanced Raman spectroscopy (SMSERS) using DNA origami as a scaffold[15,16]. This approach combines the sensitivity of SERS with the precision of DNA origami to investigate the behavior, structure, and interactions of individual molecules, such as the vital protein Cytochrome C (CytC)[17]. Modern SMSERS techniques have been optimized for the detection and study of individual CytC molecules[18]. Noble metal nanostructures, often silver or gold, are predominantly used as SERS substrates due to their ability to greatly enhance the Raman signal[19,20]. Nanofabrication techniques such as DNA origami have been developed and refined to design SERS-active structures with hot spots that enhance Raman scattering[21]. Isotopically labeled CytC has also been introduced to further help differentiate single molecule signals from the bulk responses[22].

As the field of nanotechnology continues to advance, it is expected that the combination of SMSERS and DNA origami will find broader applications in the study of various biomolecular systems, offering unprecedented insights into their structure-function relationships[23,24]. This approach has the potential to revolutionize our understanding of the molecular processes governing life, with broad implications for the development of novel therapeutics, diagnostics, and materials[25].

Overall, the synergistic combination of plasmonic nanostructures, single-molecule measurements, and DNA origami presents a powerful platform for investigating the behavior, structure, and function of individual biomolecules, such as CytC, with unprecedented precision and sensitivity. As researchers continue to push the boundaries of nanotechnology and single-molecule techniques, we can expect a deeper understanding of the molecular processes governing life, with significant implications for various fields, including medicine, materials science, and energy production[26].

In revisiting Feynman's foresight about the opportunities at the "bottom" one understands that exploring these 'small' domains illuminates a universe of potential. This potential is not merely confined to advancing scientific inquiry but also extends to broad practical applications with the capacity to shape the future of our society.

In this thesis, I have embarked on a comprehensive exploration of DNA origami technology and its applications in creating sophisticated functional materials. The central focus of my research is the versatile DNA Origami Nanofork Antenna (DONA), designed for facilitating label-free single-molecule surface-enhanced Raman scattering (SM SERS). This innovative structure enables significant signal enhancements, allowing for single-molecule SERS measurements, accommodating molecules of different sizes at various excitation wavelengths[27].

The thesis begins with a detailed examination of the design and assembly process of DONA structures, highlighting their ability to create complex arrangements of gold (Au) nanoparticles on DNA origami nanostructures. The intricate design of the nanofork (NF), featuring a rectangular base with two arms connected by a DNA double helix bridge, serves as an anchor point for target analyte molecules. This allows for precise placement into the plasmonic gap of the nanoparticles, optimizing SERS signal enhancement.

The primary objectives of my study were to assess the functionality and effectiveness of the DNA origami NF in various applications. Key questions addressed include the capability of the NF in enhancing Raman signals, the stability and precision of the structure, and particularly its suitability for the study of single-molecule CytC. This focus on CytC, a crucial protein in the electron transport chain, represents a significant portion of the research, exploring its behavior at the nanoscale level.

My findings, detailed across several chapters, demonstrate the successful application of the DNA origami NF in assembling nanoparticles and complex analyte molecules with nanoscale precision. Through oxDNA simulations, I have explored the structural dynamics of the NF, identifying the most suitable bridge length for optimal performance. The concluding chapters highlight the significant achievements of this research, including the ability to conduct label-free detection of single CytC protein via SERS. The study also underscores the versatility of DONA structures in facilitating both resonant and nonresonant SM SERS measurements, offering a novel platform for the direct, chemically specific, and label-free optical detection of single molecular entities.

This research contributes to the field by presenting new insights and methodologies for studying biomolecular reactions at the single-molecule level, potentially enabling the development of various types of nanomachines and advancing our understanding of chemical reaction pathways.

2. Theoretical background

2.1.1. Structural DNA Nanotechnology

The journey of structural DNA nanotechnology can be traced back to the monumental discovery of the DNA double helix structure by James Watson and Francis Crick in 1953[28], based on experimental data obtained by Rosalind Franklin which laid the foundation for understanding the molecular basis of life[29]. As our knowledge of DNA expanded, researchers recognized its potential as a programmable material for constructing nanoscale structures. This vision was brought to life in 1982 by Nadrian Seeman, the pioneer of DNA nanotechnology, who proposed the concept of using DNA as a building block for creating complex geometries[30]. The field took a significant leap forward with the advent of DNA origami, a groundbreaking technique developed by Paul Rothemund in 2006[11]. This method enabled the folding of long single-stranded DNA molecules into custom shapes and patterns with the help of short, synthetic DNA strands known as staples. Since then, structural DNA nanotechnology has flourished, opening new possibilities for designing and manipulating materials at the nanoscale[31].
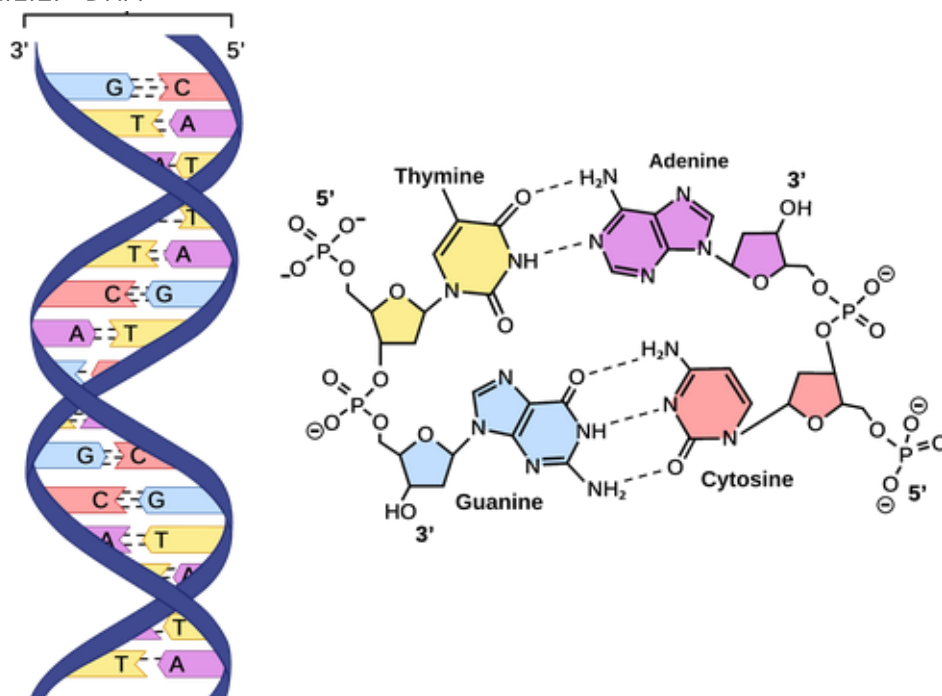
2.1.2. DNA

Figure 1 Schematic representation of the DNA and chemical structure of the Watson Crick base pairs, showing the phosphate group, sugar ring, hydrogen bonds, and the four different nucleobases in different colors (A: adenine, T: thymine, G: guanine, C: cytosine)[32].

DNA the hereditary material in all known living organisms, plays a quintessential role in directing and influencing biological functions. Structurally, DNA is a complex molecule known as a polynucleotide, composed of nucleotide monomers[33]. Each nucleotide is a combination of a pentose sugar (deoxyribose), a phosphate group, and one of four nitrogenous bases: adenine (A), thymine (T), cytosine (C), or guanine (G)[34]. These nucleotides are connected in a sugar-phosphate backbone, creating a spiraling ladder-like formation known as a double helix[28] (Figure 1).

In this structure, two strands of DNA intertwine to form a helix, with the sugar-phosphate backbone on the exterior and the nitrogenous bases on the interior, facing each other. The interaction between these bases, through hydrogen bonds, constitutes base pairing, a hallmark of DNA structure[34]. The specificity of this pairing—adenine always with thymine, and cytosine always with guanine, following the Watson-Crick base pairing rules—grants DNA its stability and its ability to accurately store and transmit genetic information[28,35].

Notably, in its most common form, known as B-DNA, the double helix is right-handed with about 10.5 base pairs per turn. Each base pair is oriented perpendicular to the axis of the molecule, and the major and minor grooves are formed by the alternating, twisting backbone[36]. This B-DNA form exists under physiological conditions and is overwhelmingly favored in the cellular environment, distinguished by its highly regular, predictable geometry. However, it should be acknowledged that DNA can adopt other conformations, such as A-DNA and Z-DNA, under certain conditions, which highlight its structural versatility[37].

Understanding the intricacies of DNA's structure is critical, as it provides a comprehensive view of how this molecule carries out its biological functions. Furthermore, the predictability and programmability that emerge from DNA's structural characteristics have rendered it a material of choice for creating complex nanostructures[38].

2.1.3. DNA Nanostructures

DNA nanostructures represent a revolutionary shift in how we perceive and utilize DNA molecules. Far from being just a passive repository of genetic information, DNA has shown its versatility as an engineering material at the nanoscale. In a pioneering paper by Seeman and Kallenbach in 1983, they conceptualized the idea of using DNA's predictable base pairing and its geometric attributes to create programmable, self-assembling nanostructures[30]. This foundational work provided a proof-of-concept for DNA-based construction and opened the door for further exploration into creating complex, precisely defined structures using DNA.
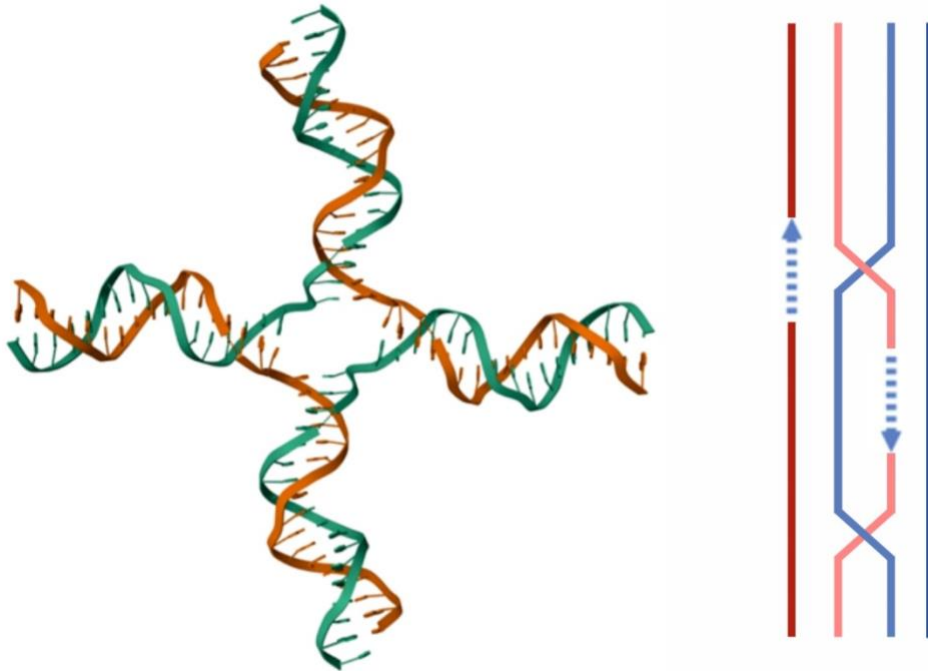
Figure 2 Schematic of a Holliday junction on the left and a DNA double-crossover (DX) on the right.)

One remarkable development in this field has been the design of rigid DNA nanostructures[37]. The realization of these constructs was enabled through a technique known as the DNA double-crossover (DX) motif, a system where two DNA helices are interlinked at two points by four crossover points[39] (Figure 2). This forms a rigid, planar structure that offers enhanced stability compared to the classic single crossover design. The predictable and robust nature of DX motifs has allowed for the formation of larger, two-dimensional lattices and three-dimensional crystals.

2.1.4. DNA Origami
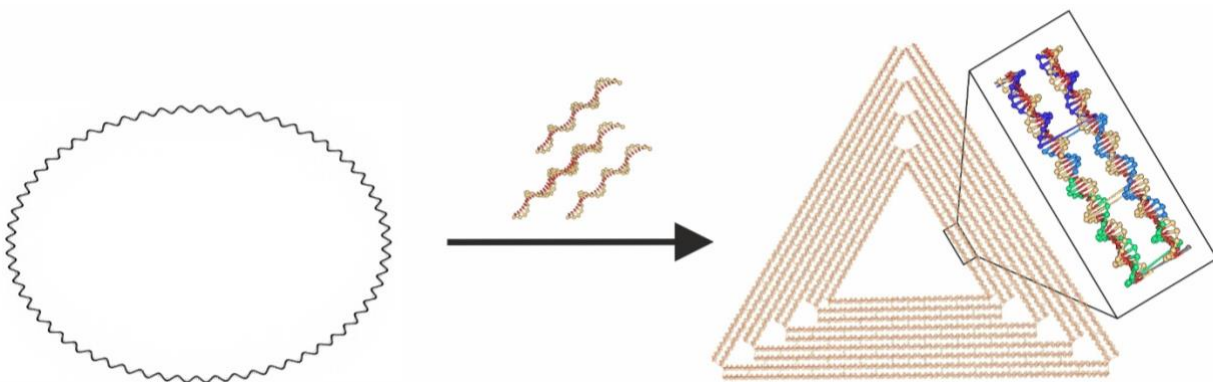
Figure 3 Illustration of the folding of a DNA origami nanostructure. Each staple strand has a unique nucleotide sequence and thus binds at a specific position of the scaffold strand, this results in the scaffold strand being folded into the desired design[40].

The DNA origami technique, a revolutionary breakthrough in the field of structural DNA nanotechnology, is fundamentally a method of folding a long, single-stranded DNA molecule (typically a viral genome) into a desired shape with the aid of numerous short, 'staple' strands (Figure 3). The term "origami" is derived from the Japanese art of paper folding, illustrating the conceptual similarity of creating intricate structures from a single material through a series of folds.

Introduced by Paul Rothemund in 2006, DNA origami has significantly expanded the potential of DNA-based nano-construction. By using a single-stranded DNA template, usually the M13mp18 bacteriophage genome, and a multitude of short, custom-synthesized staple strands, DNA origami enables the creation of complex, high-resolution, two and three-dimensional shapes and patterns[11]. This approach capitalizes on the predictable and specific nature of DNA base pairing, with the staple strands designed to fold the long, single-stranded DNA scaffold into a precise structure.

In practice, the assembly of DNA origami structures is typically performed through a process called thermal annealing. This involves heating the mixture of the scaffold and staple strands to a high temperature, then gradually cooling it over a period of hours or days. The cooling process allows the staple strands to bind, or 'hybridize,' to specific regions of the scaffold strand, guided by the rules of Watson-Crick base pairing. Consequently, the scaffold strand is gradually 'folded' into the desired structure[39].

The intricate design process involved in creating DNA origami structures necessitates the use of specialized software tools, which have been instrumental in advancing the field. These programs allow researchers to model the desired nanostructures, generate scaffold and staple sequences, and even simulate the folding process. Some of the prominent software programs include caDNAno[41], CanDo[42], and oxDNA[43].

CaDNAno, for instance, is an open-source software tool that simplifies the design of three-dimensional DNA origami structures. It employs a graphical interface that aids in visualizing the DNA nanostructure and subsequently provides an automatic assignment of staple strands. SARSE (Sequence-structure Assignment in RNA/DNA through Secondary structure Elements), on the other hand, was initially developed for RNA, but its capabilities extend to DNA structures, including complex three-dimensional DNA origami[43].

Furthermore, CanDo (Computational Analysis of Nanoscale Deformation in Origami) provides a web-based platform for predicting the 3D solution shape, mechanical flexibility, and assembly of both DNA origami and DNA brick structures. It leverages a coarse-grained mechanical model that captures the salient features of DNA mechanics and geometry, providing more detailed insights into the structural behavior of DNA origami designs. Additionally, oxDNA is a coarse-grained model that accurately captures the thermodynamic, structural, and mechanical properties of DNA nanostructures[44].

Since its inception, DNA origami has proven to be a remarkably versatile technique, enabling the fabrication of a wide range of nanoscale objects, devices, and even dynamic systems, with precision and complexity that were previously unimaginable[45]. It has been used to create myriad shapes, such as smiley faces, maps, and even complex three-dimensional structures like boxes and polyhedra[46]. Furthermore, DNA origami has seen applications in numerous areas[47], for instance, DNA origami creation of nanoscale rulers for super-resolution microscopy by labeling specific positions with fluorescent dyes[48]. The assembly of intricate Förster resonance energy transfer (FRET) constructs, facilitates the study of energy pathways between donor and acceptor molecules[49]. Further, the G-quadruplex structures on DNA origamis have been utilized to study hemin[50]. DNA damage from electron and UV radiation has been visualized using biotin-modified staples[51,52]. Finally, DNA origami has been employed to assemble plasmonic nanostructures, subsequently used to enhance the sensitivity of surface-enhanced Raman scattering (SERS) substrates[17] and surface-enhanced fluorescence (SEF) techniques[49].

2.2.RAMAN Scattering and Plasmonics

2.2.1.   RAMAN Scattering
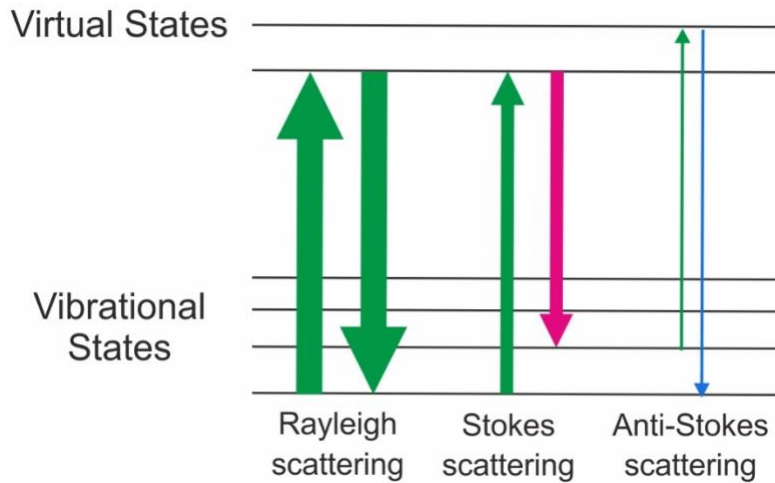
Figure 4 Schematic of Jablonski diagrams depicting the mechanisms of Rayleigh and Raman scattering. The diagrams highlight both Stokes (where the photon loses energy) and anti-Stokes (where the photon gains energy) processes in Raman scattering.

Raman scattering, a key aspect of Raman spectroscopy, occurs through a two-photon process. In this process, incident light interacts with the electrons of a molecule, inducing an oscillating dipole that then reradiates a photon. When the emitted photon possesses a different energy than the incident light, the scattering is termed inelastic, distinguishing it from other light-molecule interactions like absorption[53].

When monochromatic light, typically from a laser source, interacts with a molecule, the majority of it is scattered elastically, termed Rayleigh scattering, maintaining its initial energy. In contrast, a minuscule portion of the light (approximately 1 in 10 million photons) undergoes a change in energy upon interaction with the molecular structure (Figure 4). This results in a frequency shift of the scattered light, capturing the essence of the Raman effect[54] . This frequency shift, or Raman shift, is represented by:

$$\Delta\backslash\nu \ = \ \nu_0 - \ \nu_s \tag{1}$$

Where (ν_0) stands for the frequency of the incident light and ν_s denotes the frequency of the scattered light.

There are two primary categories of Raman scattering[54]:

1. In Stokes Raman scattering: the system is initially in its ground vibrational state. During this process, the incident photon is scattered inelastically. This interaction results in a transfer of energy to the molecule, elevating it to a higher vibrational level. Consequently, the scattered photon emerges with reduced energy (or, equivalently, a lower frequency) compared to the incident photon.

2. Anti-Stokes Raman scattering: Conversely, in this scenario, the system starts off at an excited vibrational state. Interaction with the incident photon allows the system to revert to a lower vibrational state, emitting a photon with augmented energy (or a higher frequency) compared to the incident photon.

Delving deeper, from a classical perspective, Raman scattering can be envisaged as a molecule acting like an oscillating dipole $(\vec{p_0})$, induced by the impinging electromagnetic wave$(E = E_0 \cos(\omega_0 t))$. This dynamic can be expressed as:

$$\vec{p_0} = \alpha E = \alpha E_0 \cos(\omega_0 t) \tag{2}$$

Here, (α) signifies the polarizability tensor, illustrating the molecular response to an external electric field, the (E_0) is the amplitude of the electric field of the incident light and the (ω_0) is the angular frequency of the incident light.

This polarizability tensor (α) undergoes modulation due to molecular vibrations. It relates to the vibrational coordinate q through:

$$\alpha = \alpha_0 + \left(\frac{\partial \alpha}{\partial q}\right)_0 q \tag{3}$$

During a molecular vibration, the coordinate (q) oscillates with the frequency (ω_{vib}) described as:

$$q = q_0 \cos(\omega_{vib} t) \tag{4}$$

Merging these expressions, the time-dependent change in the induced dipole moment $(\vec{p_0})$, becomes:

$$\vec{p_0} = \left(\alpha_0 + \left(\frac{\partial \alpha}{\partial q} \right)_0 q_0 \cos(\omega_{vib}t) \right) E_0 \cos(\omega_0 t) \tag{5}$$

Exploiting trigonometric identities, particularly the product-to-sum formula for cosine functions, we can split the expression above into three components:

-Rayleigh scattering:

$$\vec{p_0} = \alpha_0 E_0 \cos(\omega_0 t) \tag{6}$$

- Stokes scattering:

$$\vec{p_0} = \frac{1}{2} \left(\frac{\partial \alpha}{\partial q} \right)_0 q_0 E_0 \cos\big((\omega_0 - \omega_{vib})t\big) \tag{7}$$

- Anti-Stokes scattering:

$$\vec{p_0} = \frac{1}{2} \left(\frac{\partial \alpha}{\partial q} \right)_0 q_0 E_0 \cos\big((\omega_0 + \omega_{vib})t\big) \tag{8}$$

The intensity (I) of scattered light in Raman processes relates to the induced dipole moment (P) as:

$$I \propto \left| \vec{P} \right|^2 \tag{9}$$

Contrastingly, when discussing the scattering intensity's dependence on molecular polarizability, the term (Q) emerges. This (Q) represents the normal modes of molecular vibration coordinates, encapsulating all the collective vibrational modes of the molecule. It is a more generalized term, indicating the comprehensive set of vibrational states that the molecule can assume. The change in the induced dipole moment, related to these normal modes, is represented as ($\partial P / \partial Q$) , where (P) is the dipole moment and (Q) the collective vibrational coordinates. Therefore, while (q) is specific to individual vibrational modes, (Q) encompasses the entire spectrum of normal vibrational modes of the molecule.

From a theoretical perspective, the Raman cross-section, ($\sigma(v)$), quantifies the probability or efficiency of Raman scattering occurring for a molecule when illuminated by light of a specific frequency. In simple terms, it measures how likely it is for a photon of a given frequency (or wavelength) to be scattered inelastically by a molecule. The Raman cross-section is related to the polarizability of the molecule and the frequency of the light. This relationship can be expressed as follows:

$$\sigma(v) \propto |\alpha|^2 \cdot v^4 \tag{10}$$

In practical scenarios, however, the Raman cross-section is derived using a different formula, which relates the intensity of the scattered light ($I_{scattered}$), the area of the sample illuminated (*A*), the intensity of the incident light ($I_{incident}$), the number of molecules in the illuminated volume (*N*), and the path length of the light through the sample (*L*). This practical formulation of the Raman cross-section is given by:

$$\sigma = \frac{I_{scattered} \times A}{I_{incident} \times N \times L} \tag{11}$$

For a vibration to be "Raman active", it's imperative there's a polarizability change during the vibration, distinguishing it from infrared spectroscopy, which demands a dipole moment change. Lastly, while Raman scattering offers invaluable insights into molecular vibrations, factors such as temperature, incident light intensity, and laser power play pivotal roles, necessitating meticulous calibration and experimental condition control.

2.2.2. Optical Properties of Metals

Metals are widely known for their excellent electrical conductivity, but their optical properties also play a crucial role in various technological and scientific fields, ranging from optoelectronics, plasmonics, to nanophotonics. This stems from their unique interactions with electromagnetic radiation, distinguished by both absorptive and reflective characteristics, collectively termed optical properties[54]. We will delve into the intricate world of optical properties of metals, with a special focus on absorption, reflection, refraction, and dispersion, supported by an examination of the relevant mathematical foundations that govern these phenomena.

One of the most prominent optical properties of metals is their high reflectivity, which is due to the free movement of conduction electrons that form a 'sea' of charge carriers. When light, an electromagnetic wave, impinges on the surface of a metal, these free electrons oscillate coherently, leading to the reflection of light[55]. The complex permittivity (or dielectric function) ε(ω), where ω is the angular frequency of light, provides a critical measure of this interaction[54].

The Drude model, a foundational theory in solid-state physics, describes the behavior of electrons in metals as classical, free particles subjected to occasional collisions, providing insight into the electrical and thermal properties of metals. In terms of the Drude model, the complex permittivity is given by:

$$E(\omega) = \varepsilon_{\infty} - \frac{\omega_p^2}{\omega^2 + i\gamma\omega} \tag{12}$$

where ε_∞ is the high-frequency permittivity, ω_p^2 is the plasma frequency, and γ is the damping constant (or collision frequency). In metals, the real part of the permittivity is generally negative, leading to the reflective characteristic.

Transmission of light through a metal, however, is typically negligible due to absorption by the free electrons, contributing to the metal's opaque nature. The absorption coefficient $\alpha(\omega)$ provides a quantitative measure of the amount of light absorbed upon traversing through a material and is related to the imaginary part of the complex permittivity as follows:

$$\alpha(\omega) = \frac{\omega}{2c} \operatorname{Im}\left[\sqrt{\varepsilon(\omega)}\right] \tag{13}$$

where c is the speed of light, and $\operatorname{Im}\left[\sqrt{\varepsilon(\omega)}\right]$ refers to the imaginary part of the square root of the complex permittivity.

Although metals are not generally associated with refractive phenomena, they can show refractive behavior under certain circumstances (for instance, thin metallic films or nanostructured metals). The complex refractive index N is used to describe this phenomenon, expressed as:

$$N = n + ik \tag{14}$$

where n is the refractive index, and k is the extinction coefficient. These quantities can be calculated from the complex permittivity ε as follows:

$$n = \operatorname{Re}\left[\sqrt{\varepsilon(\omega)}\right] \tag{15}$$

$$k = \operatorname{Im}\left[\sqrt{\varepsilon(\omega)}\right] \tag{16}$$

where $\operatorname{Re}\left[\sqrt{\varepsilon(\omega)}\right]$ and $\operatorname{Im}\left[\sqrt{\varepsilon(\omega)}\right]$ are the real and imaginary parts of the square root of the complex permittivity, respectively.

Lastly, dispersion, or the frequency-dependent response of a material to light, is an essential optical property in metals. It can significantly influence both the phase and group velocities of light, thereby impacting the optical device's performance. This property is encapsulated within the complex permittivity and refractive index, described above.

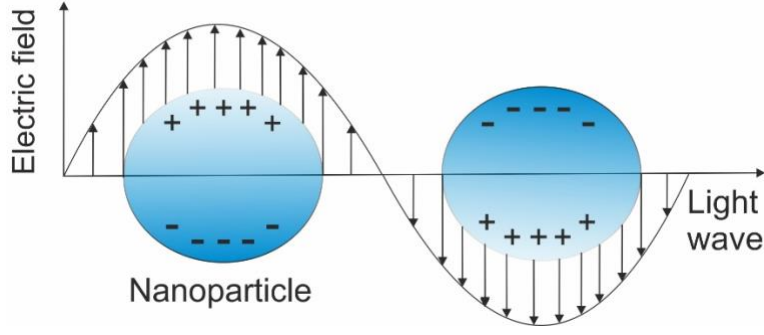### 2.2.3. Localized Surface Plasmon Resonance (LSPR)

Figure 5 Schematic of a localized surface plasmon.

Localized Surface Plasmon Resonance (LSPR) is a unique optical property of metallic nanoparticles that have drawn significant interest due to their potential applications in biosensing, medical diagnostics, photothermal therapy, and enhanced spectroscopies. In essence, LSPR is a resonant oscillation of conduction electrons induced by the interaction of light with nanoparticles (Figure 5), predominantly those made of noble metals like gold and silver, where the size of particles is much smaller than the wavelength of incident light[55].

At the heart of the LSPR phenomenon is the optical property of metals known as the complex dielectric function $\varepsilon(\omega)$, which we previously examined. It is the frequency-dependent response of the material to an electric field and plays a vital role in determining the LSPR response[56].

In the context of LSPR, we can define the condition for resonance, i.e., when the frequency of the incident light matches the natural frequency of the surface plasmons. According to Mie's theory, which describes light scattering from spherical particles[57], the LSPR condition for a spherical nanoparticle in a non-absorbing medium is given by:

$$\text{Re}[\varepsilon_m(\omega)] = -2\varepsilon_d \tag{17}$$

where $\varepsilon_m(\omega)$ is the frequency-dependent complex dielectric function of the metal and ε_d is the real, frequency-independent dielectric constant of the surrounding medium (usually air or water).

LSPR is an extremely sensitive phenomenon, influenced by changes in the local environment. The LSPR shift, defined as the change in the resonance frequency due to an alteration in the local environment, provides a crucial measure of this sensitivity. It can be quantified by differentiating the LSPR condition, yielding:

$$\frac{\Delta\lambda}{\lambda} = \frac{\Delta\varepsilon_d}{2(\varepsilon_d + 2\varepsilon_m)} \tag{18}$$

where $\Delta\lambda$ is the change in the resonance wavelength, and $\Delta\varepsilon_d$ is the change in the dielectric constant of the surrounding medium.

Another key feature of LSPR is the intense field enhancement in the vicinity of the metallic nanoparticle. This is commonly expressed as the near-field enhancement factor $\left|\frac{E}{E_0}\right|^2$, where E and E_0 are the local and incident electric fields, respectively. In the quasi-static approximation (i.e., the particle size is much smaller than the wavelength of light), for a nanoparticle at resonance, this factor is given by:

$$\left|\frac{E}{E_0}\right|^2 = \left|\frac{3\varepsilon_d}{\varepsilon_m + 2\varepsilon_d}\right|^2 \tag{19}$$

These relations provide a fundamental understanding of LSPR and form the basis for the design of plasmonic sensors, wherein changes in the local environment—such as the adsorption of biomolecules on the nanoparticle surface—induce a measurable shift in the LSPR frequency. The LSPR is influenced by particle shape, aggregation, and the interplay of various damping mechanisms[57].

The shape of a nanoparticle is a vital parameter, as it profoundly influences the plasmon resonance condition. Beyond spherical particles, the LSPR condition cannot be expressed in a simple analytical form. However, a general insight is that deviation from a spherical shape induces multipolar plasmon modes and leads to a shift and broadening of the LSPR peak. These changes stem from the fact that the spatial confinement of the electron cloud varies for different shapes, altering the restoring force in the oscillating system of electrons[57]. Advanced numerical methods, such as finite-difference time-domain (FDTD) simulations, are typically employed to calculate the LSPR spectra for non-spherical particles[57].

The impact of damping mechanisms is another critical factor affecting the LSPR spectra. In essence, damping accounts for the energy loss during the oscillation of conduction electrons. Two primary sources of damping exist - radiative and non-radiative damping. Radiative damping corresponds to the re-radiation of energy as scattered light, while non-radiative damping is attributed to various intraband and interband electronic transitions, phonon interactions, and electron-surface scattering[58].

The total damping rate, γ, is given by the sum of the radiative, γ_{rad}, and non-radiative, $\gamma_{\text{non-rad}}$, damping rates:

$$\gamma = \gamma_{\text{rad}} + \gamma_{\text{non-rad}} \tag{20}$$

Damping affects both the resonance position and the linewidth of the LSPR peak. Higher damping rates cause a redshift in the resonance peak and lead to a broader LSPR peak due to a shorter lifetime of the plasmon resonance.

In the context of LSPR sensing, a broader peak corresponds to a lower sensing resolution, underscoring the importance of managing damping in the design of plasmonic sensors.

The phenomenon of aggregation also adds a layer of complexity to the LSPR behavior. When nanoparticles come into close proximity, their individual plasmon modes can couple, leading to the appearance of new collective modes, often referred to as bonding and antibonding modes. These modes result in a broadening and splitting of the LSPR spectra, a phenomenon also known as plasmon hybridization. It's worth mentioning that the orientation of particles relative to each other can significantly influence the coupling strength and consequently the LSPR response.

2.2.4. Plasmonic Coupling
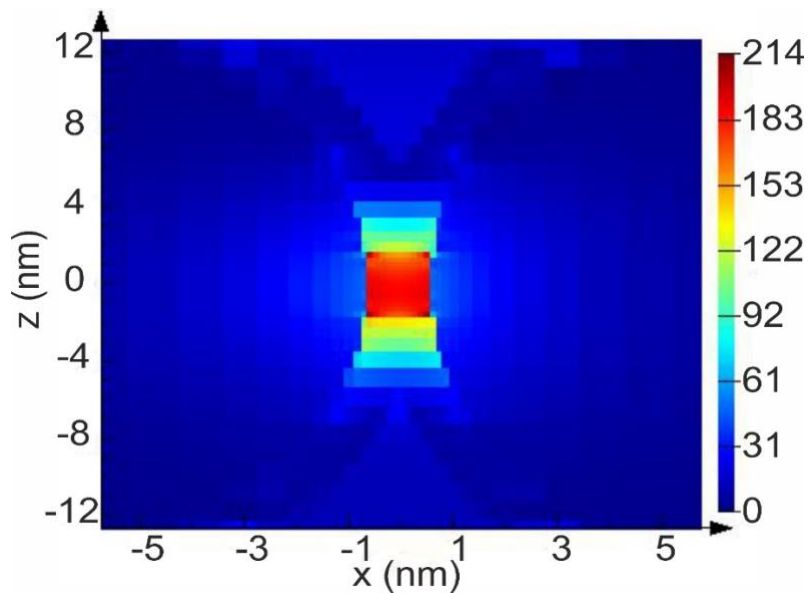
Figure 6 Simulation showing the hotspot between two AuNPs.

Plasmonic coupling is a fundamental aspect of plasmonics. It describes how the localized surface plasmon resonances (LSPRs) of nearby nanoparticles interact, leading to collective oscillations that alter the optical response of the nanoparticle system[59]. This phenomenon is key to numerous applications, such as surface-enhanced Raman scattering (SERS), plasmonic waveguiding, and high-resolution imaging[58].

The principle behind plasmonic coupling is the near-field interactions between particles. When nanoparticles are brought close together, their individual electromagnetic fields begin to overlap, causing their LSPRs to interact. This results in a change in the resonance condition, which can be experimentally observed as a shift in the extinction spectrum[60].

16

In a mathematical sense, plasmonic coupling can be explained through the concept of dipole-dipole interaction[58]. In the case of two identical spherical nanoparticles separated by a distance d (center-to-center), using the quasi-static approximation, the coupling-induced shift in the resonance wavelength, $\Delta\lambda$, can be expressed as:

$$\Delta\lambda = \lambda_{\text{isolated}} \left[\frac{\lambda_p}{\lambda_p - \lambda_{\text{isolated}}}\right] \left(\frac{R}{d}\right)^3 \tag{21}$$

Here, $\lambda_{\text{isolated}}$ is the plasmon resonance wavelength of a lone nanoparticle, λ_p is the plasma wavelength of the metal, and R is the nanoparticle's radius. This equation illustrates that the coupling-induced shift in the resonance wavelength is inversely proportional to the cube of the distance between particles, indicating a strong reliance on the particle spacing.

This model is simplified, considering only two particles and assuming the interaction is a dipolar one. For assemblies of particles that are more complex, or interactions that go beyond the dipole approximation, more advanced models such as the coupled dipole approximation (CDA) or discrete dipole approximation (DDA) may be needed.

In addition to causing a spectral shift, plasmonic coupling can also significantly amplify the local electromagnetic field in the area between the particles, commonly referred to as a "hot spot"(Figure 6). The intensity enhancement factor $\left|\frac{E}{E_0}\right|^2$ at the hot spot can be approximated as:

$$\left|\frac{E}{E_0}\right|^2 \approx \left[\frac{\lambda}{2\pi d}\right]^4 \left[\frac{\text{Im}(\varepsilon_m)}{\varepsilon_m + 2\varepsilon_d}\right]^2 \tag{22}$$

Here, ε_m is the complex dielectric function of the metal, ε_d is the dielectric constant of the surrounding medium, and d is the size of the gap.

2.2.5. Surface Enhanced Raman Scattering (SERS)

Surface-Enhanced Raman Scattering (SERS) is a powerful spectroscopic technique that capitalizes on the enhanced electromagnetic fields due to localized surface plasmon resonances (LSPRs) in metallic nanostructures. In essence, SERS amplifies the inherently weak Raman scattering signals by several orders of magnitude, often up to 10^6 - 10^{10} times, allowing for the detection and identification of single

molecules[61]. The underlying principle of SERS lies in the synergy between the chemical and electromagnetic enhancements occurring at the surface of nanostructured metals[62].

The SERS enhancement factor (EF), a critical parameter quantifying the amplification of the Raman signal, can be modeled as a product of an electromagnetic enhancement (EF_{EM}) due to the LSPRs and a chemical enhancement (EF_{Chem}) due to charge transfer mechanisms[63]:

$$EF = EF_{EM} \times EF_{Chem} \tag{23}$$

The electromagnetic enhancement, EF_{EM}, arises from the intensified electric field |E|^2 at the metal surface. In a simple model, considering a single hotspot formed due to plasmonic coupling, the electromagnetic enhancement factor can be approximated as:

$$EF_{EM} = \left| \frac{E}{E_0} \right|^4 \tag{24}$$

where $\left| \frac{E}{E_0} \right|$ is the field enhancement factor at the hotspot.

The chemical enhancement, (EF_{Chem}), though generally less significant compared to the electromagnetic enhancement, is non-negligible, especially for certain molecules that can form a charge-transfer complex with the metal surface. This enhancement is more challenging to quantify mathematically due to its dependence on the specific molecule-metal interaction, but it typically ranges from 1 to 10^3.

Therefore, the overall SERS enhancement can be substantial, allowing for the ultra-sensitive detection of molecules. The key to SERS is the fine-tuning of nanoparticle properties (such as size, shape, material, and interparticle distance) to optimize the LSPR and, thus, the electromagnetic field enhancement.

It's worth noting that the frequency shift in the Raman scattering, also known as the Raman shift, is a characteristic of the particular molecule and provides a "fingerprint" for its identification[64]. It is given by:

$$\Delta v = v_i - v_s \tag{25}$$

Where v_i is the frequency of the incident light and v_s is the frequency of the scattered light. This shift corresponds to the energy difference between the initial and final states of the molecule's vibrational modes.

In conclusion, SERS is a powerful analytical tool that enables the study of molecular interactions at nanostructured metal surfaces. Its high sensitivity and specificity make it an invaluable technique in a wide range of applications, including analytical chemistry, materials science, biomedicine, and environmental science[65]. In the following chapters, we will explore these applications in more detail, together with experimental and theoretical methods to optimize the SERS effect.
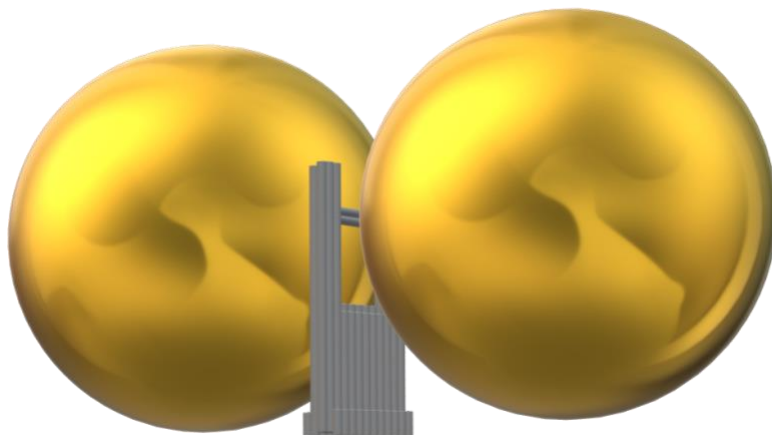
2.2.6. DNA-Assisted Plasmonics

Figure 7 3D model of the Nf with two AuNPs each attached on one side of the NF.

DNA-Assisted plasmonics is an emerging and rapidly expanding field that leverages the inherent properties of DNA, coupled with the plasmonic effects of metallic nanoparticles, to create functional structures and systems with controlled optical properties. This innovative approach capitalizes on the unique attributes of DNA, such as its programmability, self-assembly capabilities, and biocompatibility, to precisely engineer nanoparticle assemblies with well-defined geometries, thereby manipulating their plasmonic behaviors[66].

Key to DNA-assisted plasmonics is the concept of DNA origami, which employs a long, single-stranded DNA, known as the scaffold, along with a set of short, staple strands that guide the folding of the scaffold into desired shapes[11]. These DNA structures can serve as templates to organize plasmonic nanoparticles into predefined spatial configurations, controlling their collective optical response (Figure 7).

A fundamental aspect of DNA-assisted plasmonics is the precise control of the interparticle distance, which strongly influences the plasmonic coupling, as discussed in previous sections[17,67]. The shift in the resonance wavelength due to plasmonic coupling in a DNA-mediated assembly of two nanoparticles can be described by a previously mentioned equation. In this context, the center-to-center distance between the nanoparticles, denoted as "d", can be precisely tuned by the DNA length. Other terms in the equation represent the radius of the nanoparticle, the plasmon resonance wavelength of an isolated nanoparticle, and the plasma wavelength of the metal.

Furthermore, the field enhancement factor at the hot spot formed between the particles, influenced by DNA-mediated nanoparticle positioning, can be represented by another equation that we discussed

earlier. This equation takes into consideration various parameters including the dielectric function of the metal and the dielectric constant of the surrounding medium[68].

Importantly, in addition to serving as a structural scaffold, DNA can also play a role in the chemical enhancement aspect of SERS, especially when considering DNA sequences with specific metal-binding properties.

DNA-assisted plasmonics also provides a versatile platform for creating dynamic systems, where the plasmonic response can be modulated by DNA conformational changes triggered by external stimuli, such as temperature, pH, or specific biomolecular interactions[69].

While the full potential of DNA-assisted plasmonics is still being realized, the ability to program the assembly of plasmonic nanostructures using DNA provides an unprecedented level of control over their optical properties. This holds significant promise for the development of advanced optical devices, sensors, and bioimaging tools[70]. In the following sections, we will delve into the practical aspects of designing and fabricating DNA-based plasmonic systems, as well as the broad spectrum of their potential applications.

2.2.7. Functionalization of DNA Origami Structures

Building on the foundational concept of DNA origami introduced earlier, a key aspect of this technology lies in its potential for functionalization with a diverse array of chemical moieties. This capability enables the attachment of various functional groups or nanoparticles to predetermined sites on the origami structure, thus extending its utility. Precise spatial control is achieved by designing specific binding sites into the DNA scaffold, allowing for the organized and programmable arrangement of attached molecules or particles[40].

The range of entities that can be conjugated to DNA origami structures is extensive. It includes metallic nanoparticles, fluorescent labels, enzymes, and small therapeutic molecules, among others. The methods of attachment vary, encompassing covalent bonding, electrostatic interactions, and affinity-based binding such as biotin-streptavidin systems. This functionalization is instrumental for applications in fields like biosensing, targeted drug delivery, and the development of nanoscale electronic components, capitalizing on the unique characteristics of the attached moieties[71].

In the context of this thesis, a major focus is placed on CytC, a key protein involved in the electron transport chain. The integration of CytC with DNA origami presents an opportunity to study its properties in a controlled and precise manner, opening new avenues for understanding its role in cellular processes and its potential in nanotechnology-based applications.

2.3. Cytochrome C

CytC is a small, highly conserved, and vital protein found universally in the mitochondria of eukaryotic cells and in the bacterial cytoplasm. This globular protein possesses a molecular weight of approximately 12,000 Daltons and is comprised of a single polypeptide chain of roughly 100 amino acids[72]. This protein contains a covalently attached heme prosthetic group, which consists of an iron ion coordinated in a porphyrin ring (*Figure 8*). This heme group is a critical element for CytC's fundamental biological function: facilitating electron transfer during the process of oxidative phosphorylation[73]. Oxidative phosphorylation, a core segment of cellular respiration, is the metabolic pathway in which cells use enzymes to oxidize nutrients, thereby releasing energy to produce adenosine triphosphate (ATP), the primary energy currency within cells[74].
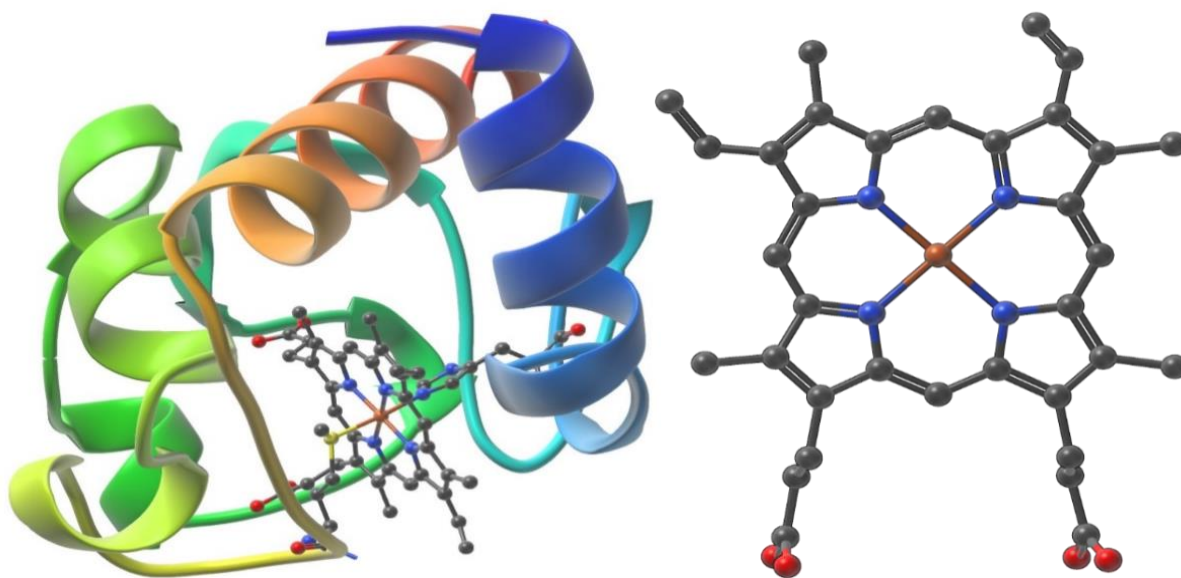
Figure 8 (Left) Schematic view of CytC structure with the heme unit in the center. The iron ion is coordinated to four nitrogen atoms provided by a porphyrin ring, forming a plane. The fifth and sixth coordination sites are perpendicular to this plane. The fifth position is usually attached to a nitrogen atom from a histidine residue and the sixth position is usually occupied by a methionine sulfur. (Right) Molecular view of the heme unit with the iron ion in the center; Iron (orange), Nitrogen (Blue), Carbon (Black), Oxygen (Red).

Evolutionarily, CytC is intriguing due to the high degree of conservation in its primary structure across an immense array of organisms, spanning the simplest unicellular organisms to the most complex multicellular life forms, suggesting a universal requirement for this protein in the biological realm[75]. This sequence conservation renders CytC a critical tool for comparative genomics and phylogenetic studies, providing important insights into the evolutionary relationships among diverse species[76].

Within the multi-step framework of oxidative phosphorylation, CytC plays a specific and indispensable role as an electron shuttle within the electron transport chain. This chain is a sequence of redox-driven protein complexes embedded in the inner mitochondrial membrane. Specifically, CytC accepts an electron from the bc1 complex (Complex III), facilitated by a series of electron carriers. Subsequently, CytC transfers this electron to the CytC oxidase complex (Complex IV) [77]. This redox reaction is strongly linked with the transport of protons across the inner mitochondrial membrane, which results in the establishment of a proton motive force. This electrochemical gradient is subsequently harnessed by ATP synthase to drive the synthesis of ATP, the primary energy currency within cells[74].

Interestingly, the role of CytC extends beyond this life-sustaining process of ATP synthesis. It also plays a critical function in the initiation of apoptosis, a highly regulated mechanism of programmed cell death. Apoptosis is a cellular response to certain types of stress signals, ensuring the removal of damaged, infected, or unwanted cells in an orderly manner[77]. In response to these cellular stress signals, CytC can be liberated from the mitochondrial intermembrane space into the cytosol. Once in the cytosol, CytC triggers the formation of the apoptosome, a protein complex that initiates a proteolytic cascade culminating in cell demise[78]. This function is essential for maintaining cellular homeostasis and preventing the uncontrolled proliferation of potentially oncogenic cells. Any dysregulation in this process is often implicated in a wide range of pathologies, including various forms of cancer[79].

Despite the extensive understanding of the biochemical and biophysical properties of CytC, multiple areas remain ripe for investigation. The intricate role of CytC in apoptotic signaling[80], the molecular mechanisms regulating its cellular location and function[81], as well as the potential extra-mitochondrial functions of CytC, all constitute active areas of investigation. Thus, CytC continues to occupy a central position in cellular and molecular biology research, symbolizing the exquisite complexity of life's processes at the cellular level.

Regarding CytC, Raman spectroscopy has been widely used to study the protein's secondary structure and the state of the heme group[82]. The technique provides detailed information about the protein's conformation under various conditions, such as different pH levels[83] or in the presence of various ligands[84]. Raman spectroscopy has also been used to study the interaction of CytC with the mitochondrial membrane, providing insights into the protein's function in apoptosis[85].

In recent years, the use of SERS in studying CytC has gained significant attention. Due to the high sensitivity and specificity of SERS, it can provide detailed information about the protein at very low concentrations, even down to the single-molecule level[86]. This is particularly advantageous when studying proteins like CytC, which can be challenging to study in high concentrations due to their propensity to aggregate. SERS has been used to study the changes in CytC structure during the process of apoptosis, providing insights into the early stages of this crucial cellular process[87].

Despite the significant progress made in using Raman spectroscopy and SERS to study CytC, there are still many challenges and opportunities in this field. One of the main challenges is interpreting the complex Raman spectra of proteins. The spectra are often characterized by overlapping bands corresponding to different vibrational modes, making it challenging to assign specific bands to specific structural features[88]. Recent advances in computational methods and algorithms for spectral analysis are providing new tools to address this challenge.

Another exciting opportunity is the use of SERS to study CytC in live cells. Although this is technically challenging due to the difficulty of delivering the SERS substrates into cells and the potential toxicity of these substrates, recent advances in nanoparticle technology are making this increasingly feasible. Such studies could provide unprecedented insights into the dynamics of CytC in its natural environment[89].

Raman spectroscopy and SERS also offer exciting opportunities for the development of new diagnostic tools. For example, since changes in the Raman spectrum of CytC are associated with the early stages of apoptosis, this could potentially be used to develop new methods for early cancer detection[90]. Similarly, changes in the SERS spectra of CytC have been associated with neurodegenerative diseases like Alzheimer's, suggesting potential applications in neurology[91].

The advent of single-molecule analysis using SERS opens a multitude of exciting opportunities in the study of CytC. The possibility of analyzing individual molecules rather than an ensemble average can provide more detailed and nuanced insights into the structure, function, and dynamic behavior of this vital protein[92]. Given the heterogeneity inherent in biological systems, single-molecule analysis offers the ability to capture these variations and observe phenomena that might otherwise be obscured in ensemble measurements[93].

For example, single-molecule SERS can potentially reveal heterogeneous behaviors in the population of CytC molecules in terms of their binding interactions, conformational changes, and redox states[94,95]. This kind of information could further our understanding of how individual CytC molecules function in the

23

electron transport chain and the initiation of apoptosis. These insights could provide valuable information about the range of normal behaviors for CytC, as well as any deviations associated with disease states.

Moreover, the ability to monitor individual CytC molecules in real-time offers the opportunity to observe dynamic changes in the protein's structure and interactions. Such dynamic observations can provide a wealth of information about the mechanisms of protein function and regulation, as well as the protein's interactions with other cellular components[96].

Furthermore, single-molecule SERS could be used to study the interactions of CytC with potential drugs or inhibitors at the individual molecule level. This could lead to a more detailed understanding of how these substances interact with the protein and could aid in the design and optimization of therapeutics.

In conclusion, the opportunity for single-molecule analysis of CytC using SERS offers a powerful new approach to further unravel the intricacies of this vital protein. The ability to study individual molecules could shed light on the inherent heterogeneity of biological systems, the dynamic nature of protein function, and the interactions of proteins with other molecules. These insights could ultimately lead to an improved understanding of the cellular mechanisms of life and disease and could potentially inform the design of new therapeutic strategies.

3. Materials & Methods

3.1. Materials

Table 1 List of materials.

Name	Company
100 kDa MWCO Amicon filters, 0.5 mL	Merck
10x TAE buffer (0.4 M Tris, 0.4 M Acetate, 0.01 M EDTA)	SIGMA Aldrich
60 nm goldspheres, bare (citrate)	NanoComposix
ACCESS-NC-A AFM probes	SCHAEFER-TEC
Agarose powder	SIGMA Aldrich
AuNP DNA coating strands	IDT
Cytochrome c from bovine heart	SIGMA Aldrich
Heraeus Fresco 17 centrifuge	Thermo Fisher Scientific
HORIBA OmegaScope with a LabRAM HR evolution	HORIBA
Glycerol	SIGMA Aldrich
Mica wafer "V1" 15 mm x 15 mm ca. 0,16 mm	Plano
Nanofork DNA staple strands	SIGMA Aldrich
ParafilmM	Carl Roth
Primus 25 Thermocycler	Peqlab/VWR
Magnesium chloride	SIGMA Aldrich
Neutravidin coated glass slides	Polyan
Sandwich assay DNA strands	Metabion
Sodium chloride	SIGMA Aldrich
Silicon wafer	Siegert wafer
Single-stranded scaffold DNA, type p7249 (M13mp18)	Tilibit nanosystems
TCEP solution	SIGMA Aldrich

3.2. Methods

3.2.1. DNA Origami NF Assembly

The DNA origami fork is self-assembled in one pot. (Figure 11) A mixture of 2.5 nM circular scaffold strand M13mp18 (consisting of 7,249 nucleotides, as referred to in Table of Materials) and 100 nM of 201 short oligonucleotides (indicated in Table) were combined in a 1x TAE buffer supplemented with 15 mM $MgCl_2$. To achieve the desired volume, ultrapure water was added to bring the total volume of the solution to 100 μL.

Following the preparation of the solution, an annealing process was carried out. This process involved subjecting the solution to a temperature gradient in a thermocycler. Initially, the solution was rapidly heated to 80 °C. The solution was then cooled gradually from 80 °C to 20 °C at a rate of 1 °C every 12 minutes. This was followed by further cooling from 20 °C to 16 °C at 1 °C per 6 minutes and an abrupt cooling down from 16 °C to 8 °C.

The next step was to purify the mixture from excess staples. This was done using 100 kDa molecular weight cut-off (MWCO) Amicon filters. We added 100 µL of the DNA origami solution to the Amicon filters and supplemented it with 400 µL of ultrapure water. The solution was then centrifuged at 6,000 x g for 8 min at room temperature (RT). The filtrate was discarded by removing the filter and flipping the tube to let the wash-out flow into the sink. The filter was then loaded with another 400 µL of ultrapure water and centrifuged again. This process was repeated once more.

Lastly, to retrieve the purified nanostructure solution, we flipped the filter upside down into a new tube and centrifuged it at 1,000 x g for 2 min at room temperature (RT), in accordance with the manufacturer's instructions. The resulting solution can be stored in a fridge at 8 °C for up to 2 weeks.

3.2.2. AFM Measurements
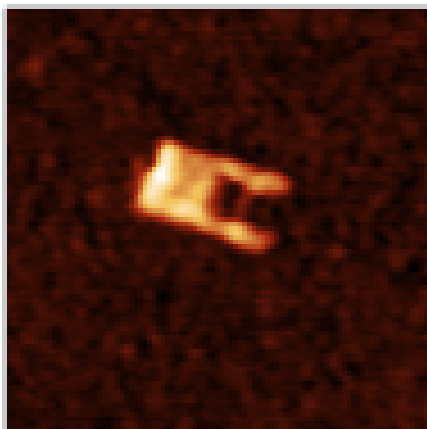
Figure 9 AFM image of the NF.

The procedure of Atomic Force Microscopy (AFM) imaging was carried out using a FlexAFM equipped with a C3000 controller from Nanosurf. The technique employed was tapping mode, and imaging was conducted in air utilizing a Tap 150 Al-G cantilever. This cantilever operates at a resonance frequency of 150 kHz and has a spring constant of 5 N/m and a tip size of 10 nm. Two types of substrates were utilized for imaging purposes: mica sourced from Plano and silicon provided by Siegert Wafer. The silicon used was of 100 orientation and was p-doped with boron.

Preliminary inspections to verify the shapes of DNA origami nanostructures were executed on mica. This was accomplished by adding 2 µL of the sample and 18 µL of a 15 mM $MgCl_2$ solution to the freshly cleaved mica, then allowing it to incubate for 2 minutes. The mica was then rinsed twice using a washing mix (1:1 ethanol-to-water) and dried with compressed air.

For the analysis of the fork structures, Si wafers were used. Prior to use, these silicon wafers were prepared by roughly cutting them into squares of 0.5 cm on each side. They were then cleaned twice using the washing mix, dried with compressed air, and plasma treated for 10 minutes. A 5 µL sample and 15 µL of a 50 mM $MgCl_2$ solution were added to the Si wafer, which was left in a wet chamber for 30 minutes. The substrate was subsequently rinsed 2 times with 1 mL of the washing mix and dried using compressed air.

In order to conduct the NFs analysis, images were captured of a 3 µm x 3 µm area at a scan speed of approximately 0.8 s/line, 512 data points/line. The proportional gain (P-Gain) and integral gain (I-Gain) were set between the ranges of 1000 and 1500. The resulting images were then processed and displayed using Gwyddion, an open-source software (Figure 9).

For the AFM measurements of the colocalization measurements, the HORIBA system was used (Table 1). Tapping mode (in the system as AC mode) in air was used with ACCESS-NC-A cantilever which operates at a resonance frequency of 300 kHz and spring constant of 45 N/m. The images captured were of 30 µm x 30 µm, the scan rate was set to 1 Hz and 1200 data points/line. All other parameters were automatically controlled by the software, including adjusting the scan rate to provide the best image quality (Figure 10).
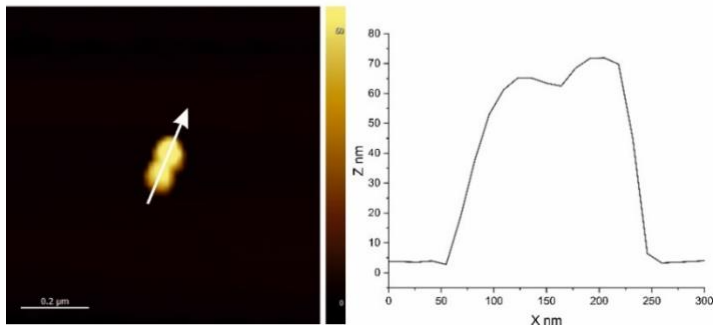
A)
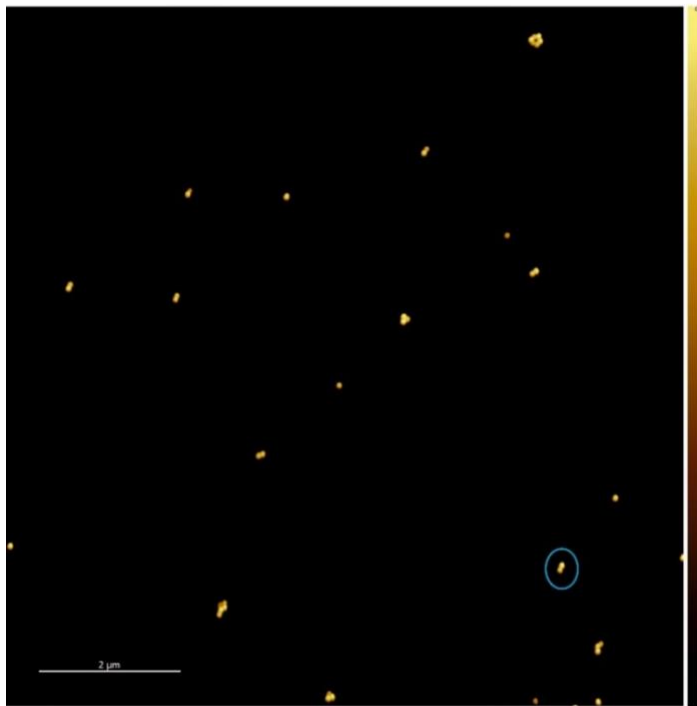
B)

Figure 10 A) AFM image of the DONAs B) A close up of one of the DONAs and a cross-section the height profile[97].

3.2.3. DNA Origami NanoAntenna (DONA)

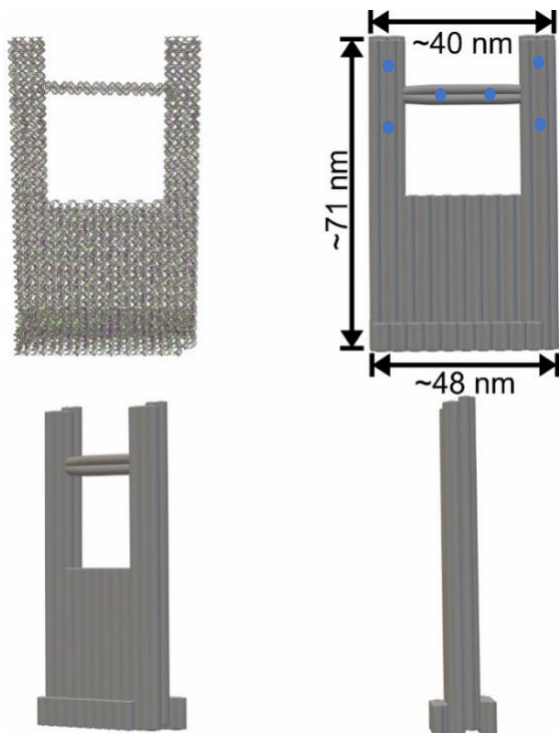#### 3.2.3.1. DNA Origami NF Assembly

Figure 11 Top left is a OxDNA model of the NF. The other three are different views of a 3D model of the NF (The blue circles represent the NF and AuNP attachment points).

The procedure followed is identical to that detailed in section (3.2.1) with the exception that the middle bridge strand is replaced with one modified with pyridine (Table 2), to bind CytC. Upon collection of NFs solution, a solution of CytC is added to it, aiming for a final concentration of 100 µM of CytC, and incubated at RT for 30 min. Following the incubation, the mixture undergoes a single round of purification and is subsequently collected using Amicon filters with a molecular weight cut-off (MWCO) of 100 kDa.

Table 2 List of extra DNA strands.

Strand	Sequence
AuNP DNA coating strand 1	5DTPA-TTT TTT TTT TTT TTT TTT TTT TTT
AuNP DNA coating strand 2	GTT GTT GTT GTT GTT GTT GTT GTT-3DTPA
Nanofork bridge strand #161 (Pyridine (T3))	4-Pyridine acetic acid (C5)-TTTAAAGCACTAAATCGGAACCCTTGAATCGGCCAACGCGCGGGG
AuNP DNA long coating strand 1	5DTPA-GGT TTT TTT TTT TTT TTT TTT TTT TTT
AuNP DNA long coating strand 2	GTT GTT GTT GTT GTT GTT GTT GTT TTT-3DTPA

3.2.3.2. Gold Nanoparticle (AuNP) Coating

We employed a modified version of Liu et al.'s protocol to coat the AuNPs[98]. The protocol involves freezing the AuNP-DNA solution during the coating process. Initially, we centrifuged 400 µL of a 60 nm diameter AuNP solution (obtained commercially as per Table of Materials) at 3,500 x g for 5 min at room temperature (RT). The supernatant was carefully removed with a pipette, and the resulting pellet was resuspended in 25 µL of ultrapure water, giving us a final AuNP concentration of ~0.3 nM.

Next, we added 1 µL of 100 mM TCEP solution to 4 µL of thiol-modified DNA (100 µM as supplied by the manufacturer; see Table of Materials) and allowed it to incubate for 10 min at room temperature (RT). Following incubation, we added this 5 µL mixture to the concentrated AuNP solution obtained in the earlier step. The mixture was then vortexed for 5 s and frozen for at least 2 hours at -20 °C.

After thawing at RT, we centrifuged the mixture at 3,500 x g for 5 min at room temperature (RT) to remove the excessively added coating DNA. The supernatant was again carefully removed with a pipette, and the pellet was resuspended in 10 µL of water.
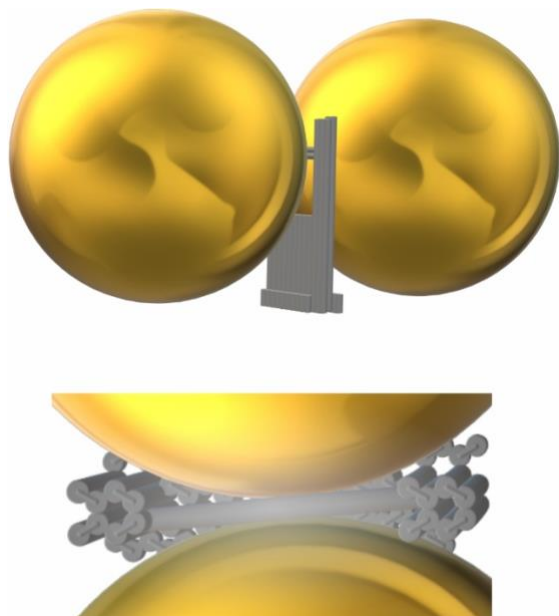
3.2.3.3. DONA Assembly

Figure 12 Top) Schematic of fully formed DONA. Bottom) Top view of DONA.

For DONA (Figure 12) assembly, we mixed the coated AuNP solution with the DNA NF solution at a molar concentration ratio of 1.5:1 respectively. We then added $MgCl_2$ to attain a final concentration of 4 mM,

using a 50 mM MgCl$_2$ stock solution. The final volume of the mixture was adjusted to 20 µL using ultrapure water. The DONAs were hybridized by applying a temperature gradient in a thermocycler. The solution was rapidly heated to 40 °C, then cooled gradually from 40 °C to 20 °C at 1 °C per 10 minutes, and then rapidly cooled from 20 °C to 8 °C Gel Electrophoresis
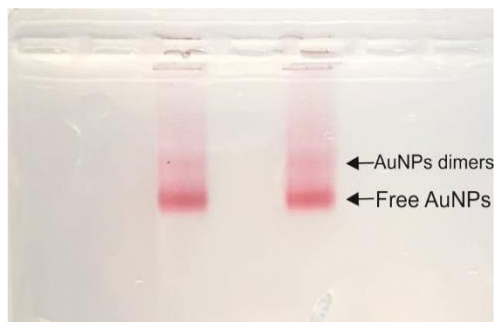
Figure 13 Agarose gel Showing the separation of DONAs from the free AuNPs in the sample. Both wells are the same sample.

The DONAs were purified from the unbound nanoparticles in the solution via agarose gel electrophoresis (Figure 13). To prepare the 1% agarose gel, 0.8 g of agarose was dissolved in 80 mL of 1x TAE supplemented with 5 mM MgCl$_2$. Then, 2.25 µL of loading buffer (containing 30% glycerol, 13 mM MgCl$_2$; see Table of Materials) was added to 18 µL of the DONA solution to achieve a final MgCl2 concentration of 5 mM. The gel was run for 60 min at 70 V in an ice water bath with a running buffer of 1x TAE supplemented with 5 mM MgCl$_2$. The band of interest was then cut out and placed on a paraffin plastic film-wrapped microscopy slide. The squeezed liquid was collected into a 500 µL tube using a pipette.

3.2.4. Colocalization of AFM and Raman Measurements[97]

Figure 14 Sketch of the Omegascope Showing the top and side illumination/collection light path. The top illumination is used for our SERS measurements.

31

For colocalization of AFM and Raman measurements (Figure 15), a silicon chip was plasma-treated for 10 min. The purified DONA solution (10 µL) plus 10 µL of 100 mM MgCl2 were then incubated o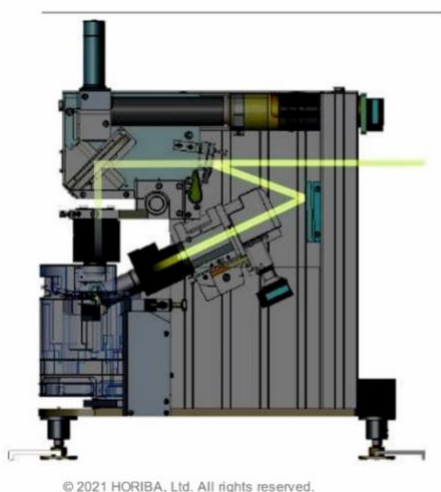n the chip for 3 h in a wet chamber. The chip was washed twice with the washing mix and dried with compressed air. The chip was then taped onto a magnetic disc and inserted into the instrument for imaging. The instrument in use was HORIBA OmegaScope with a LabRAM HR evolution (Figure 14). To initialize the system the desired laser was auto calibrated, and the laser spot is placed exactly at the apex of the AFM cantilever.

Before commencing the measurements, it is essential to adjust the position of the Raman excitation laser to align precisely with the apex of the Atomic Force Microscope (AFM) probe. This alignment ensures the accuracy and consistency of the measurements. The instrumentation is sophisticated and allows for precise control and manipulation of the experimental setup. The system is operated using LabSpec and AIST software, which provide a user-friendly interface for managing both the Raman microscope and the AFM components.

Following the completion of the AFM imaging, a crucial step is the retraction of the AFM tip. This retraction is necessary to ensure that the tip does not obstruct the path of the Raman laser during subsequent measurements. To achieve this, we employ a macro function titled "Probe away," which is programmed into the system (Figure 16). This function automatically retracts the AFM tip to a safe position. Importantly, this step guarantees that for any selected point in the AFM image, the Raman laser's position will be accurately aligned with no offset, ensuring precise correlation between the AFM and Raman data.

The final step involves selecting appropriate parameters for the Raman measurements. These parameters include the laser wavelength, the power of the laser, and the accumulation time. It is crucial to tailor these settings based on the specific characteristics of the sample being measured. The choice of wavelength, power, and time significantly affects the quality and relevance of the Raman data, and hence, careful consideration and adjustment of these parameters are imperative to achieve optimal results.
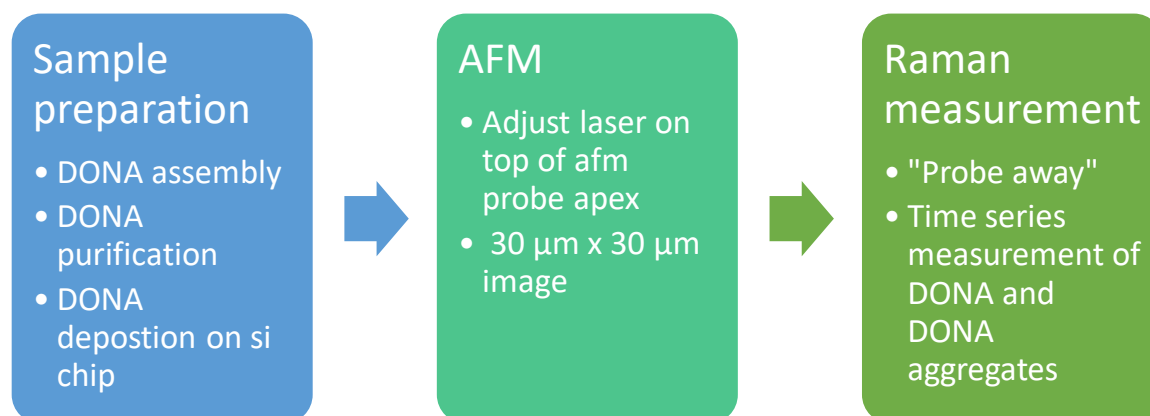

Figure 15 Workflow for the colocalization of AFM and Raman measurements.
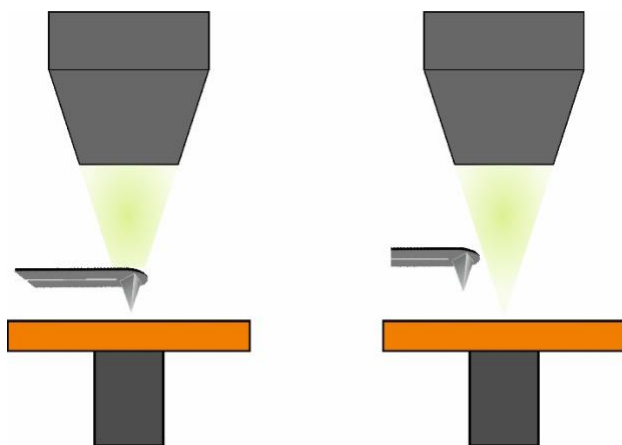
Raman Measurements

Figure 16 Schematic of the objective and the sample holder of the Omegascope. Left is the setup during the AFM imaging. Right is the setup after using the "Probe away" function, showing the AFM cantilever position which allows the laser to fall directly on the sample.

For the Raman measurements, precise targeting of the DONA or aggregates is crucial. This targeting is accomplished using the AFM image as a reference. By employing the "move cursor" function in the software, the cursor is accurately positioned over the selected DONA or aggregate. This step ensures that the Raman laser focuses on the exact area of interest, critical for obtaining relevant and precise spectroscopic data.

The final phase of the process involves carefully selecting the laser wavelength, power, and accumulation time, which are crucial parameters that vary depending on the sample's specific characteristics. In the case of single DONA measurements, the parameters chosen were a 660 nm laser wavelength, a power setting of 3.5 mW, and an integration time of 0.1 seconds, spanning a total measurement period of 300 seconds (Total of 3000 measurements). This setup is designed to optimize the detection and analysis of single-molecule signals. Conversely, for measurements involving aggregates, a slight adjustment is made to these parameters to accommodate the different optical properties of the aggregates. The laser wavelength is maintained at 660 nm, but the power is reduced to 1.4 mW. The integration time remains unchanged at 0.1 seconds, over the same duration of 300 seconds. These adjustments are necessary to accurately capture the distinct Raman signatures of aggregates, differing from those of single DONAs.

3.2.5. Sandwich Assay

A sandwich assay is a type of immunoassay that detects the presence of a specific target molecule (an antigen) within a sample. It uses two antibodies that are designed to bind to different parts (epitopes) of the target molecule[99]. In this specific case, we use two partially complementary DNA strands to detect SARS-CoV-2 Spike DNA. One of these partially complementary DNA strands is attached to the bottom of our modified AuNPs.

The AuNPs were coated using the same method described in section 3.2.3.2 with the difference of using the AuNP coating strand from Table 3. AuNPs with a total volume of 25 µl, were mixed with 4 µl each of target spike DNA and surface DNA. This mixture was incubated for 10 minutes at a temperature of 37 °C. After this initial incubation, the solution was allowed to rest at room temperature (RT) for an additional 20 minutes. Subsequently, a 5 µl aliquot of the sample, combined with 10 µl of 1x TAE supplemented with 750 mM NaCl buffer, was placed onto an avidin-coated glass surface. This was followed by a rinse using a 1:1 mixture of water and ethanol, after which the surface was blow dried using compressed air.

Table 3 List of sandwich assay DNA strands.

Strand	Sequence
AuNP coating strand	Thiol-C6-(Tamra-dT)TC AAG GTC ACT ACC ACT AGT
Surface strand	AAT AAT AAG AAA ATA AAC AT-Biotin
Spike DNA	ATG TTT ATT TTC TTA TTA TTT CTT ACT CTC ACT AGT GGT AGT GAC CTT GA

4. Results and Discussion

The DNA origami NF, a meticulously designed structure intended for single-molecule Raman measurements. The unique shape of the NF, featuring a wider base, was specifically chosen to ensure stability, especially when the base is functionalized for surface attachment. Meanwhile, its open top design allows for the addition of reagents or molecules during measurements, facilitating real-time monitoring. The design process of the NF was facilitated by cadnano, a specialized software tool used for the design of three-dimensional DNA structures. It provides a user-friendly interface for creating complex DNA geometries, essential for precise nanoscale construction. Additionally, the modeling of the NF's mechanical properties and stability was performed using the CanDo (Computer-aided Design of DNA Origami) software. CanDo employs a sophisticated algorithm to predict the structural behavior of DNA origami designs, offering valuable insights into their mechanical robustness and feasibility for experimental applications. This combination of advanced design and modeling tools was pivotal in realizing the NF's potential as a platform for advanced Raman spectroscopy techniques.

4.1. Fork Optimization

The process of optimizing a complex molecular structure such as the NF is both intricate and iterative. As the field of nanotechnology has evolved, DNA origami has become a valuable tool for precise molecular design. In this setting, our efforts to optimize the NF stemmed from practical needs and the natural progression of our research.
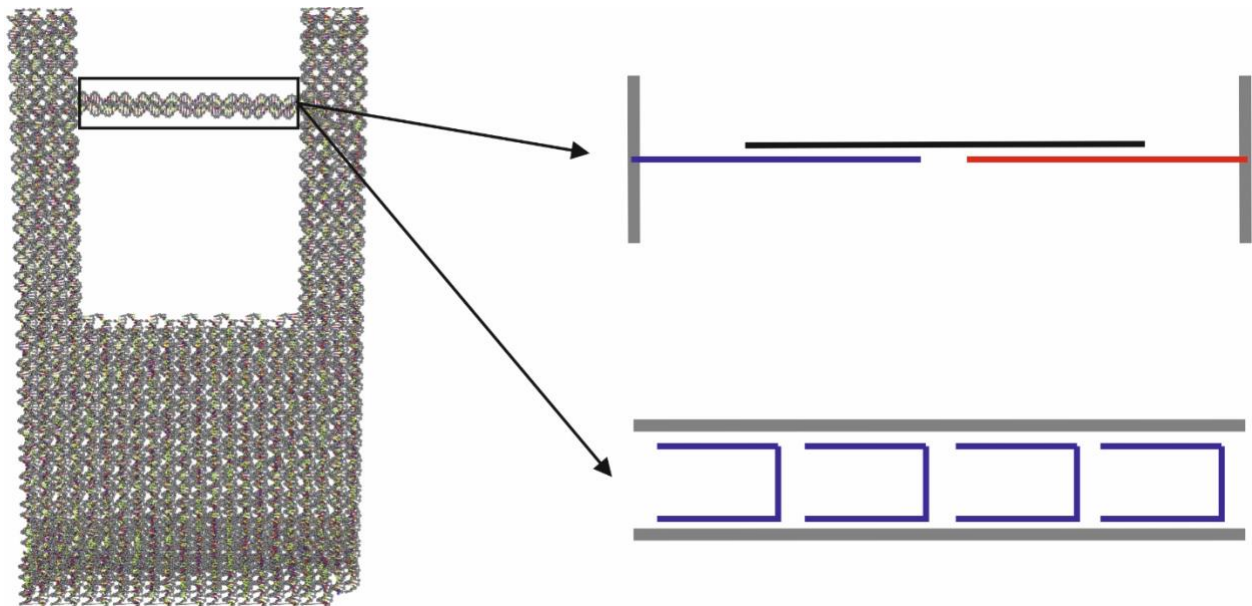

Figure 17 Left OxDNA model of the NF. On the top right a schematic zoomed in view of the NF bridges. The top side is the original design, the bridge was constructed using 3 different partially complementary strands that are attached to sides of the arms. Bottom side is the modified design, where the scaffold runs top and bottom and are held together with 4 different crossovers.

The initial attempt involved a design where the bridge of the fork was made from three distinct DNA strands (Figure 17). This design aimed to utilize the natural complementarity of DNA for stability. However, practical results deviated from theoretical expectations. The bridge, composed of multiple strands, proved to be insufficiently stable. Atomic Force Microscopy (AFM) imaging highlighted this issue; images often showed indistinct or missing bridges in the fork structures, as exemplified in Figure 18, where the bridge is absent in all the NFs. This instability could be attributed to either the bridge breaking under the stress exerted by the flexible arms of the fork or a low efficiency in bridge formation during the folding process of the fork.
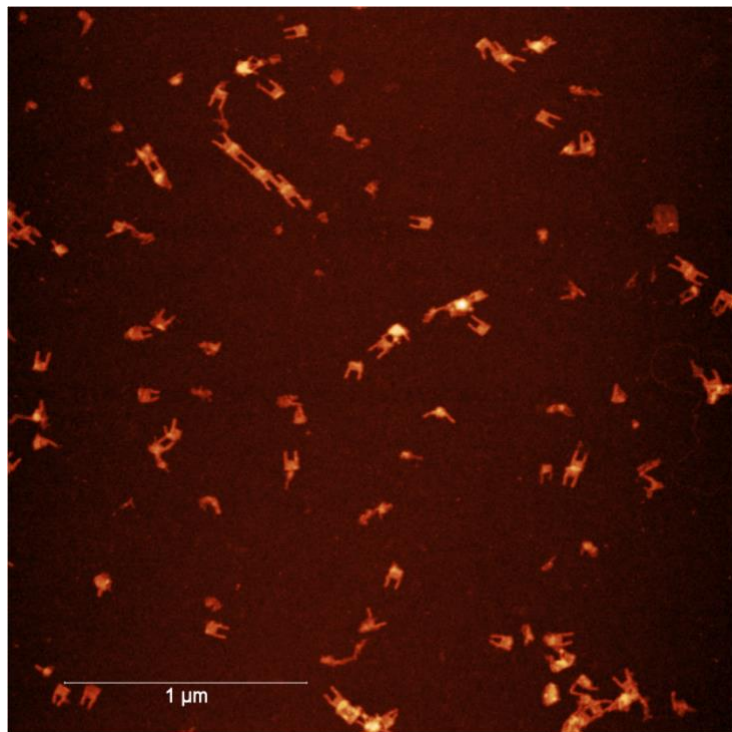
Figure 18 AFM image of the original NF with the 3 individual strands bridge.

In light of these observations, a design modification was deemed essential. We considered the inherent stability of DNA's double-helix structure, capitalizing on this we integrated the bridge directly into the DNA scaffold (Figure 17). The revised design employed a two-loop strategy, with one loop residing inside one of the NF arms. This strategy allowed us to include the bridge in the scaffold route without the need to completely redesign the NF from the ground up. The initial observation was that the bridge was visible in AFM imaging for most of the NFs (

Figure 19).

Yet, the journey of optimization did not end there. While the integrated bridge offered more stability, the overall structure, especially the longer variant of the fork, remained flexible. Such flexibility, while occasionally desirable, was not optimal for our applications. To address this, we turned to computational methods. OxDNA, a powerful tool for DNA simulations, was employed to model and analyze different fork

sizes and configurations, which was done by Dr. Antonio Suma. These in-depth simulations provided invaluable insights, directing us towards a shorter, more stable bridge design, comprising 90 nucleotides, a reduction from the initial 120 nucleotides.
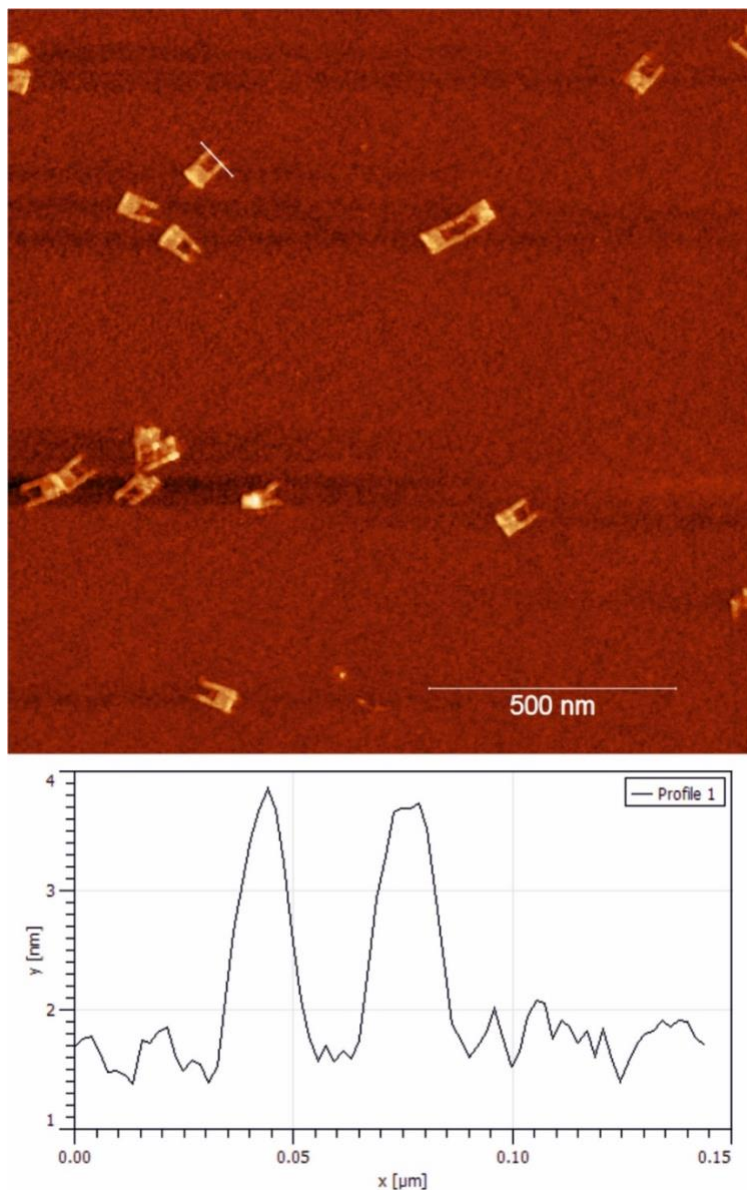
Figure 19 Top AFM image of the redesigned fork that includes the bridge in the scaffold routing. Bottom a height profile of the NF arms that is used to calculate the distance between them. The white line that crosses the top of the NF is where the height profile is taken.

With this refined design in hand, the final step was empirical validation. A comprehensive AFM imaging was initiated, capturing detailed images of the various fork designs. This included the fork without a bridge, the newly designed short fork, and the long fork. From the AFM images the distance between the fork arms was measured using Gwyddion software (Figure 19). The imaging results were then meticulously

compared with the simulated predictions, forming a holistic understanding of the NF's behavior, both in silico and in vitro (Figure 20).
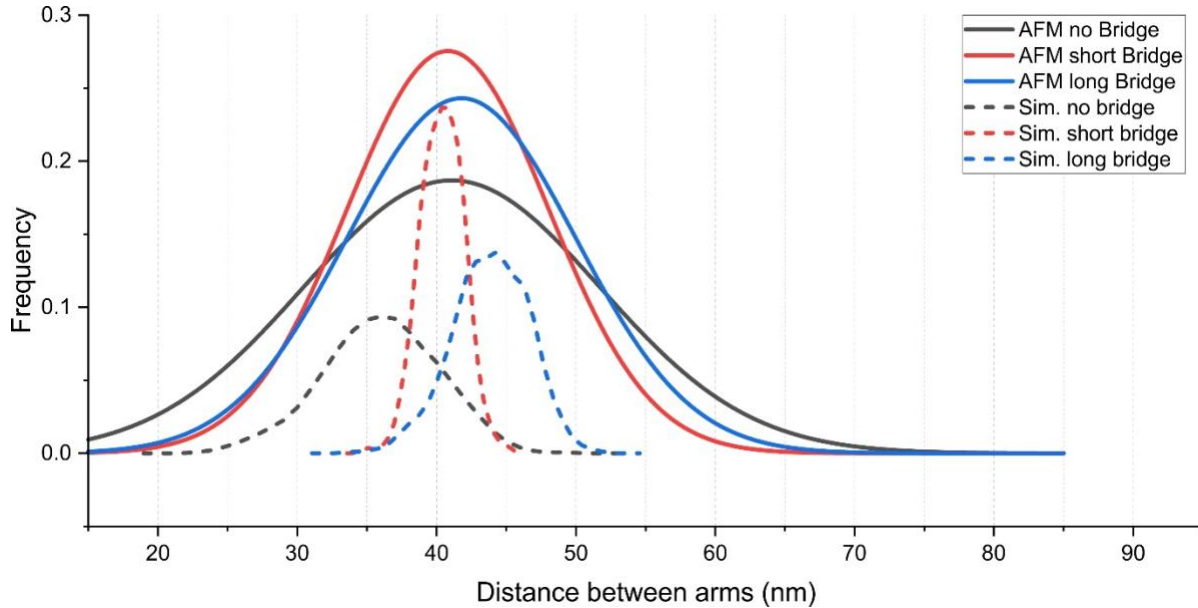
Figure 20 Plot showing the distributions of the simulated and experimental NFs.

To compare the simulated and experimental NFs, we utilize the Full Width at Half Maximum (FWHM) of the distribution (*Table 4*). The FWHM provides a measure of the spread or variability of the particle sizes. In the simulated NFs, the No Bridge design exhibits a moderate FWHM of 10.1 nm, indicating a certain level of variability in the predicted spatial distribution. The Short Bridge design demonstrates a strikingly narrow FWHM of 4.0 nm. This suggests a high degree of predictability and potential rigidity in the spatial arrangement of this design, as foreseen by the simulation. In contrast, the Long Bridge configuration displays a slightly broader FWHM (6.8 nm), suggesting a slightly higher degree of variability compared to the short bridge.

Table 4 Analysis of the simulated and experimental NF arm distance.

	Median (nm)	FWHM (nm)
AFM no Bridge	41.3	25.2
AFM short Bridge	40.9	17.0
AFM long Bridge	41.8	19.3
Sim. no bridge	36.5	10.1

Sim. short bridge	40.2	4.0
Sim. long bridge	43.2	6.8

Transitioning to the experimental observations, we see a different picture. The No Bridge design, while showing a moderate FWHM in simulation, exhibits a significantly larger FWHM (25.2 nm) in real-world measurements. This suggests that real-world interactions and factors not fully captured in the simulation might introduce greater variability. Similarly, the Short Bridge design also displays a larger experimental FWHM (17.0 nm) compared to its simulated counterpart, further highlighting potential discrepancies between the model and reality. Consistent with this trend, the Long Bridge design has an FWHM of 19.3 nm, indicating a noticeable degree of variability in the experimental setting.
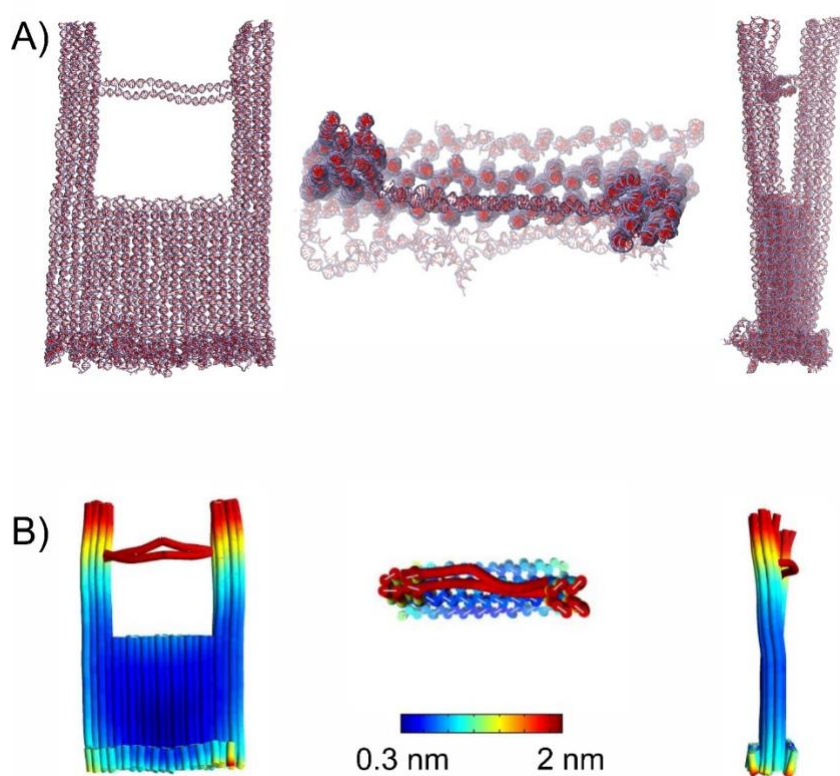
Figure 21 Comparison of oxDNA and CanDo NF simulation. A) front, top and sideview respectively of the NF oxDNA simulations[86](Simulations done by Dr. Antonio Suma). B) front, top and sideview respectively of the NF CanDo simulations.

In the process of designing and optimizing NFs, different simulation tools offer unique advantages at various stages. Cando and oxDNA are two such tools, each with their specific strengths (Figure 21).

Cando, known for its granular approach, is particularly useful during the initial phases of design. It provides critical insights into the flexibility of the NF's arm and bridge, which are essential components of the structure. By employing Cando simulations early on, it can be assessed how flexible these parts are, ensuring that the NFs are functional and robust. Additionally, Cando is adept at identifying potential weak spots or areas of increased flexibility in the base of the NF, which is crucial for ensuring the structural integrity and functionality of the NF.

On the other hand, oxDNA offers a more detailed analysis of the dynamics of NFs. This makes it an invaluable tool in the optimization phase of the design process. With oxDNA, one can delve deeper into the NF's behavior, allowing for more detailed measurements, such as the precise distance between the arms of the NF. This level of detail is crucial for fine-tuning the NF design to meet specific requirements and ensuring optimal performance in its intended applications.

Overall, both Cando and oxDNA play pivotal roles in the design and optimization of DNA origami NanoForks, each contributing unique insights that are vital for the development of these sophisticated nanostructures.

DNA origami technology is characterized by its precision in nanoscale assembly. Recent advancements have significantly enhanced the methodologies involved in origami design, synthesis, functionalization, and characterization. The development of software tools for designing DNA origami structures has been a game-changer in this field. First-generation tools like caDNAno were instrumental for designing various 2D and 3D structures, albeit requiring extensive manual input and expertise.

The evolution to second-generation design software marked a leap towards user-friendliness, significantly reducing the technical knowledge required. Tools like vHelix stand out for their ability to automatically generate staple sequences from 3D designs, integrating simulation platforms that predict the folding of designed structures in standard DNA origami folding buffers[100]. The latest in software development includes platforms like Adenita and ATHENA, which merge features from both first and second-generation tools, offering versatile and user-friendly interfaces for a wide range of design possibilities, including multilayered structures and lattice-based wireframes[101].

Recent advancements have significantly enhanced our ability to create and manipulate DNA nanostructures for various applications[102]. DNA origami enables the bottom-up self-assembly of prescribed DNA nanoobjects[103]. This process involves multiple short synthetic DNA strands binding to different regions of a DNA scaffold, folding it into a desired shape. The design of these structures can be intricate, as they often involve converting the target shape into cylinders representing DNA double helices,

connected by crossovers at specific intervals[104,105]. The most commonly used scaffold is the M13 virus genome, valued for its well-identified sequence and commercial availability[106].

One key area of development in DNA origami is in building larger DNA structures[107]. This can be achieved by either using longer[108] DNA scaffolds or through hierarchical assembly of DNA origami monomers[109]. While longer scaffolds provide a straightforward solution, they pose challenges like increased internal secondary structures, which reduce folding yield, and higher construction costs. Hierarchical assembly, on the other hand, uses origami monomers with programmed connectors to form larger structures more cost-effectively.

Another innovative approach in DNA origami is the use of DNA bricks. This method, pioneered by Yin and colleagues[110], bypasses the limitations imposed by the DNA scaffold in traditional origami methods. It involves the assembly of hundreds of single-stranded tiles (SSTs) into finite and fully addressable DNA structures through local interactions, enabling the creation of large and intricate 2D and 3D DNA nanostructures. Unlike traditional DNA origami, which uses a mix of biological and synthetic materials, this modular assembly strategy employs entirely synthetic strands, offering greater flexibility and control over the design of the structures.

These developments in DNA origami design, optimization, and assembly methods have expanded the potential applications of DNA nanostructures. They allow for more complex and larger-scale constructions, paving the way for advanced applications in fields like nanotechnology, biomedicine, and materials science[111]. The ongoing research and innovation in this area continue to push the boundaries of what can be achieved with DNA as a building material at the nanoscale.

DNA Origami is used in nanofabrication, nanophotonics, and nanoelectronics is particularly noteworthy. In the realm of catalysis, DNA origami provides a structured environment for catalysts, enhancing their efficiency and specificity[112]. In computation, DNA origami structures offer a novel platform for the development of molecular machines and computational elements[113]. The technology's application in bioimaging and drug delivery highlights its potential in biomedical fields, where its precision and controllability can lead to breakthroughs in targeted therapy and diagnostics[114]. Additionally, DNA origami's role in biophysics provides valuable insights into molecular interactions and dynamics[115,116].

The DNA origami NF within our system showcases remarkable potential for a variety of applications, particularly in fields that require high precision at the nanoscale. Its design, allowing for the precise placement of chemical species at nanometer distances, is especially advantageous for single-molecule

studies. The ability to achieve sub-5-nm resolution in positioning distinct molecules opens up new possibilities in molecular sensing and analysis.

One of the primary applications of our DNA origami NF is in the field of Raman spectroscopy. Its precise molecular positioning capabilities enhance the accuracy and sensitivity of Raman spectroscopic analysis, making it an ideal tool for studying single-molecule interactions and behaviors. This precision is crucial for observing subtle changes in molecular structures and dynamics, which is essential for understanding complex biochemical processes.

Our DONA exemplifies state-of-the-art advancements in DNA origami technology, particularly in its application versatility. The DONA system's ability to assemble Au or Ag nanoparticle dimers with varying gap sizes, down to as small as 1.17 nm, facilitates significant enhancements in surface-enhanced Raman scattering (SERS) signals, allowing for single-molecule SERS measurements. This capability extends to accommodating molecules of different sizes at various excitation wavelengths, demonstrating the system's adaptability to diverse experimental requirements.

The DONA's design ensures the precise placement of a wide range of molecules into the SERS hot spots. This includes not only small molecules and DNA but also more complex biomolecules such as CytC and horseradish peroxidase. The system's flexibility in accommodating molecules of different dimensions within the gap between Au nanoparticles is a testament to its innovative design and effectiveness. Even with larger gap sizes, DONA structures are capable of producing single-molecule signals, illustrating the balance between accommodating larger molecules and maintaining sufficient field enhancement for effective SERS measurements.

Molecular dynamics simulations using the oxDNA model have been crucial in optimizing the NF structure. These simulations have provided insights into the effects of bridge length on the DNA arms' positioning and the overall stability of the structure. The choice of a 90 nt bridge length, as opposed to a longer 120 nt bridge, has been shown to offer more precise positioning and reduced fluctuation, crucial for the accurate placement of target molecules at the plasmonic junction.

In practical applications, our DNA origami NF has demonstrated its efficacy in SERS measurements of complex proteins like CytC and horseradish peroxidase, using Au DONA structures. The ability to achieve detailed SERS spectra of these proteins, with clear distinction of specific Raman bands, underscores the system's capability in label-free detection and analysis of single molecules and proteins, even under non resonant conditions. This adaptability and precision in molecular detection pave the way for new insights into biomolecular interactions and reactions at the single-molecule level.

4.1.1. DONA Optimization
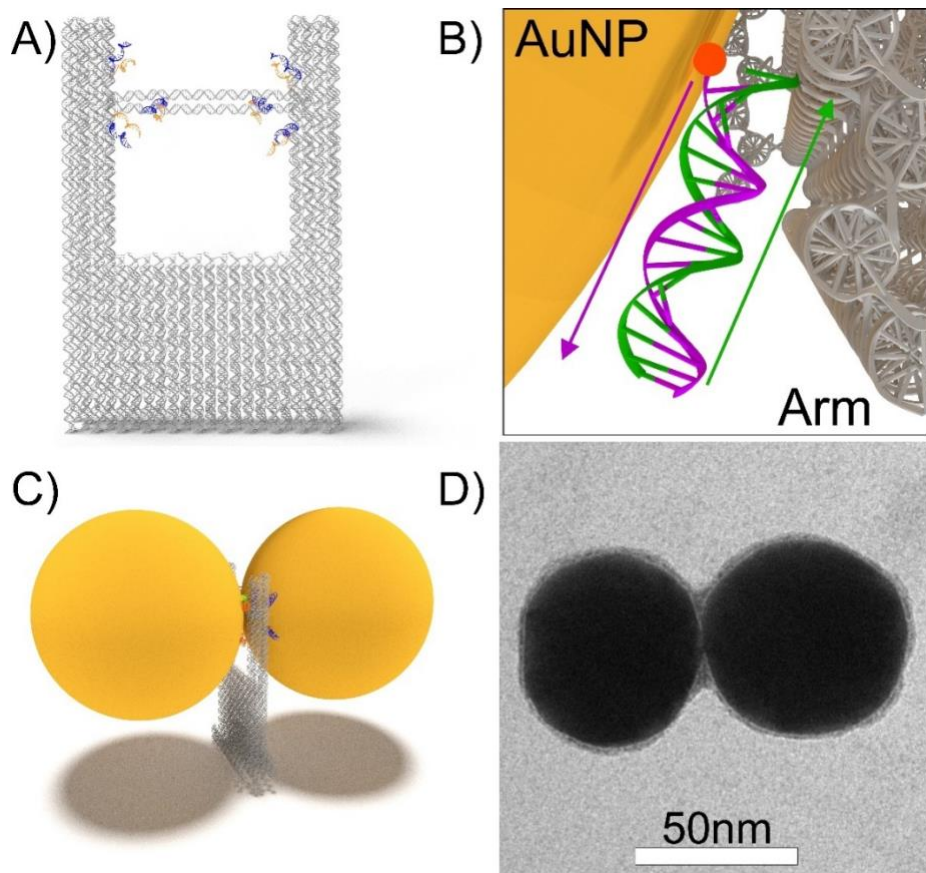
Figure 22 A) NF model showing the 12 AuNP capture strands blue and orange for each face of the fork. B) A close up of the capture strands after DONA formation showing that the DNA is designed in a zipper formation, with the arrows showing the 5' to 3' direction. C) model of the DONA. D) TEM image of the DONA[117].

In the sophisticated design of the DONAs, careful consideration is given to the placement and tuning of AuNPs capture points to create an optimal detection environment. Specifically, six distinct AuNP capture points are strategically positioned on each face of the NF (Figure 22). This precise arrangement is crucial for ensuring that the AuNPs are ideally located, facilitating the formation of a hotspot right at the center of the NF bridge. This central hotspot is key for effective sensing and analysis.

Moreover, the design allows for the adjustment of the hotspot volume by varying the length of the capture strands. This flexibility in tuning the hotspot size is particularly advantageous when dealing with larger target molecules. By extending the length of these capture strands, the hotspot can be expanded, thereby accommodating bigger molecules within its range.
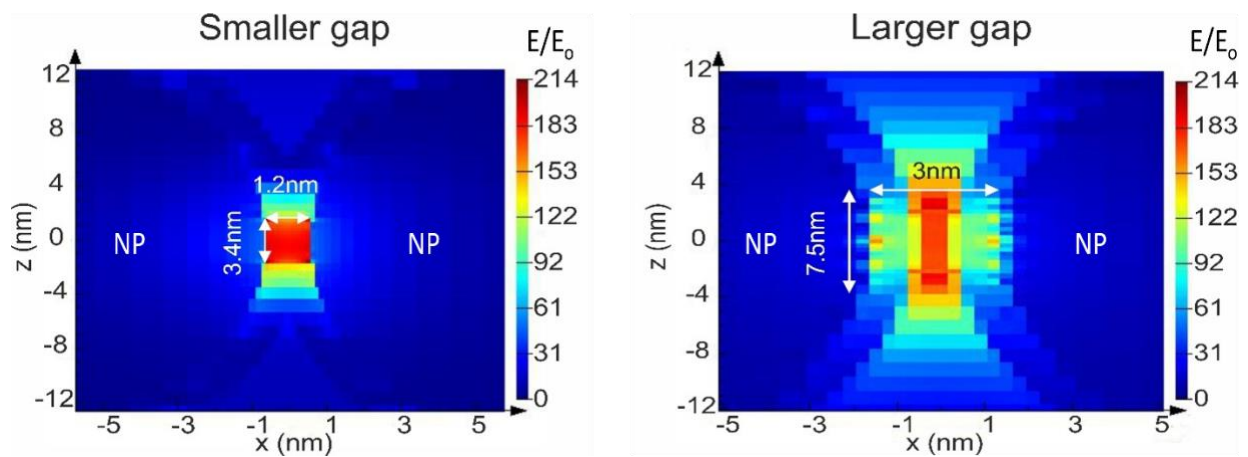
Figure 23 Simulation showing two different gap sizes 1.2 nm and 3 nm respectively, with the red color being the SM detection zone[117](simulations done by Dr. Kosti Tapio).

In addition the NFs are also designed with respect to the configuration of the capture strands (Figure 22). These strands are typically arranged in a zipper configuration, which is a crucial design choice. The zipper configuration ensures that the strands are in close proximity to each other, which is vital for maintaining a stable and consistent hotspot. This proximity effectively reduces fluctuations, leading to more reliable and accurate sensing.

However, this design is not rigid and can be adapted based on specific requirements. For situations where additional length and flexibility are needed, the capture strands can be reconfigured into a parallel alignment. This alternative setup allows the strands to extend further, providing greater flexibility. This flexibility can be particularly beneficial when targeting larger or more complex molecules, as it allows for a broader interaction space within the NF.

By offering the option to switch between zipper and parallel configurations, the NF design demonstrates remarkable versatility. This adaptability ensures that the NF can be fine-tuned for a wide range of applications, catering to the diverse needs of molecular sensing and analysis.
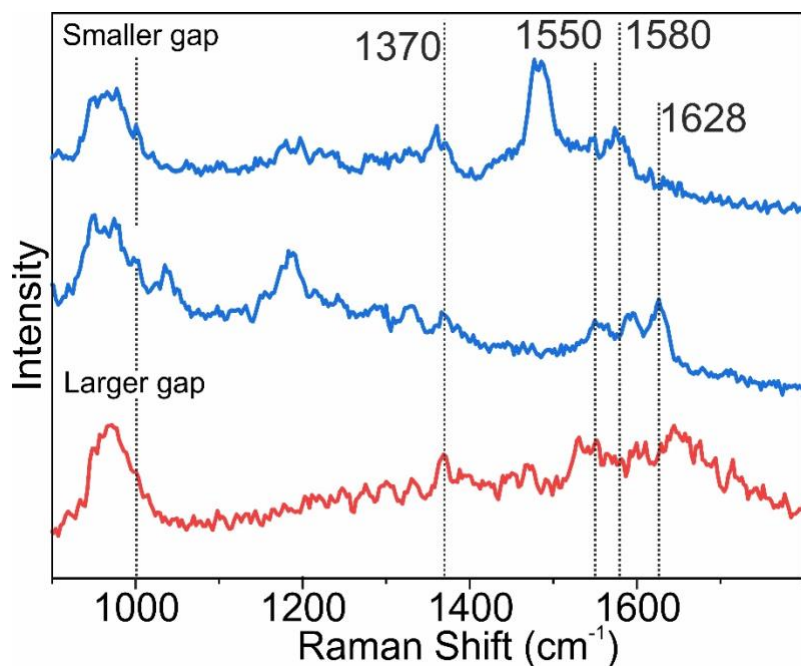
Figure 24 CytC SERS spectra from DONAs with smaller gap (1.2 nm) and larger gap (3 nm). The vertical lines are expected CytC strong peaks[117].

The analysis of CytC SERS spectra used DONAs with two gap sizes: 1.2 nm and 3 nm (Figure 23). Both DONAs had a zipper configuration, but the 3 nm gap design included a spacer before the zipper sequence. The results from both configurations indicated the presence of the expected CytC peaks, which confirms the effectiveness of DONAs in capturing the characteristic spectral features of CytC. However, a notable difference was observed in the signal strengths. The DONA with the smaller gap size of 1.2 nm yielded a stronger SERS signal (Figure 24). This enhanced signal can be attributed to the closer proximity of the AuNPs in the smaller gap, which creates a more concentrated and effective hotspot for SERS activity.

In contrast, the larger gap size of 3 nm in the DONA configuration resulted in an overall weaker SERS signal. This decrease in signal strength is likely due to the reduced electromagnetic field enhancement, as the larger gap leads to less effective plasmonic coupling between the AuNPs. This lesser coupling diminishes the intensity of the hotspot, thereby affecting the signal strength of the SERS spectra.

These findings highlight the critical role of gap size in the design of DONAs for SERS applications. The gap size directly influences the plasmonic coupling and, consequently, the efficiency of SERS signal enhancement. This understanding is vital for optimizing DONA designs for specific molecular studies, such as the detailed analysis of proteins like Cytochrome C.

4.2. Cytochrome C

4.2.1. UV-Visible absorption
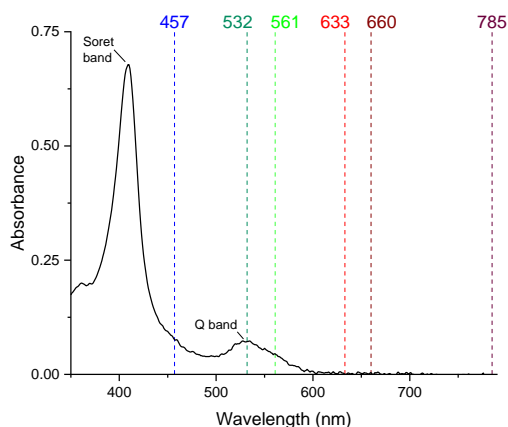
Figure 25 UV-Visible spectrum of Cytochrome C from Bovine Heart. The vertical lines represent the different lasers used for Raman scattering excitation.

UV-visible absorption spectroscopy has been effectively used to identify the oxidation states of the iron ion in CytC[118]. The ferric (Fe^{3+}) state of the iron ion in CytC is accompanied by a distinctive Soret band, a distinctive absorption feature in the visible and near-ultraviolet region. In the ferric (Fe3+) state of CytC, this band is particularly prominent, appearing at a wavelength of 408 nm, as illustrated in Figure 25. The presence of this Soret band serves as a definitive indicator of the ferric state of the iron ion.

Additionally, the absorption spectrum of CytC reveals another key spectral feature, the Q band, typically found in proteins containing a heme group. This band was observed at a wavelength of 530 nm, further elucidating the electronic transitions within the protein. Alongside these, a third spectral characteristic at 695 nm, however it was not observed in our measurements..

The combination of these spectral markers – the pronounced Soret band at 408 nm and the Q band at 530 nm,– collectively facilitated a conclusive determination. They indicated that in our CytC solution, the iron ion predominantly exists in its ferric (Fe3+) state.

4.2.2. Normal Raman (NR) Spectroscopy of CytC
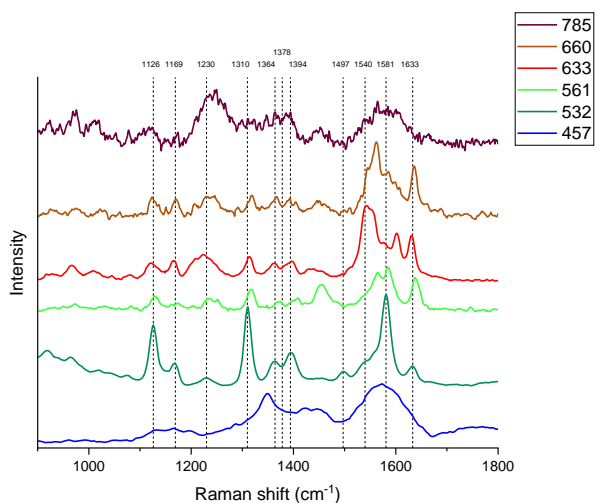
Figure 26 NR spectra of CytC powder using multiple laser wavelengths. The vertical lines represent the most prominent peaks found in the literature (Table 5)

We undertook a set of Raman experiments on powdered samples, systematically subjecting them to various laser wavelengths to assess changes in peak intensities and positions. Through this comprehensive spectral approach, we were able to contrast the results across different excitation wavelengths (Figure 26).

Our research confirmed that the laser at 532 nm yielded the optimal signal-to-noise (S/N) ratio. It was also observed that the spectral range spanning 457 nm to 633 nm offered satisfactory S/N ratios, highlighting it as an area meriting further exploration. Conversely, the S/N ratios for lasers with wavelengths of 660 nm and 785 nm were suboptimal, presumably due to their distance from the Soret band of CytC.

Notably, the 457 nm laser induced the most significant signal intensity, potentially due to the resonance Raman excitation near the Soret band at 408 nm. An intriguing finding was the nearly identical spectra generated by the 633 nm and 660 nm lasers. Conversely, the spectra from the 457 nm and 532 nm lasers were akin. The spectral data from the 561 nm laser appeared to be intermediate between these clusters.

One hypothesis for these patterns is the closeness of the 633 nm and 660 nm lasers to the Q band at 695 nm. In contrast, the congruence in spectra between the 457 nm and 532 nm lasers might arise from their proximity to the 530 nm Q band. The positioning of the 561 nm laser, influenced by both bands, may explain its distinct, median spectral placement.

48

An additional distinction among the lasers pertains to their distance from the resonance of CytC. Lasers with wavelengths of 633 nm, 660 nm, and 785 nm exhibited subdued peaks for the heme unit. In contrast, there was a pronounced presence of peaks in the range of 1180 cm^-1 to 1350 cm^-1, which might be ascribed to the peptide backbone of CytC[119]. This behavior starkly contrasts with what was observed for the lasers at 457 nm, 532 nm, and 561 nm.

Table 5 Comparison of NR CytC peaks in literature and measured sample.

Normal Raman in cm^{-1}					Band assignment
514 nm[120]		**532 nm**[121]		Our result	
Oxidized	Reduced	Oxidized (LS)	Oxidized (HS)	532 nm	
		1128	1128	1126	v_s(pyr half-ring)
1174		1169	1169	1169	v_s(pyr half-ring)
1232		1240	1233	1230	δ(CH)
1314		1314	1316	1310	δ(CH)
1375	1360	1370	1371	1364,1378	v_s(pyr half-ring)
1400		1403	1406	1394	v(pyr quarter-ring)
1408					v(pyr quarter-ring)
1501	1492	1499		1497	v(CC)
1540				1540	v(CC)
1568		1564		1556	v_{as}(CC)
1587		1585	1568	1581	v_{as}(CC)
1626					v_{as}(CC)
1640		1637	1632	1633	v_{as}(CC)

The examination of our spectral data showed alignment with peaks observed in literature when using the 532 nm laser, as detailed in Table 3. This alignment supports the reliability of our experimental methods and the consistency of our findings.

While the 532 nm laser demonstrated stable wavelength performance, we noticed minor variations in peak positions within the laser spectrum. These differences were slight, typically within a range of less than 10 wavenumbers, as shown in Figure 26. This highlights small performance differences between lasers that can lead to minimal peak shifts.

One notable difference among the lasers was the variation in peak intensity. This was expected due to the different capacities of lasers to excite various vibrational modes. Each laser, with its unique wavelength and energy output, interacts differently with the sample, leading to these variations in peak intensity. For instance, certain lasers may be more efficient at inducing specific vibrational transitions, resulting in more pronounced peaks for those transitions. Conversely, other lasers might not interact as effectively with the same modes, leading to relatively subdued peak intensities. This characteristic is fundamental to the nature of laser-induced Raman spectroscopy, where the choice of laser can significantly influence the outcome of the spectral analysis.

Regarding UV-Vis spectral analysis for determining the iron ion's oxidation state, the process was intricate. We observed overlapping peaks representing both oxidized and reduced states in the laser spectra, which complicated the interpretation of the data. Occasionally, subtle shifts in peak positions led to the iron oxidation state peak appearing at an intermediate position, particularly evident in the 561 nm laser spectrum.

Finally, the complexity inherent in bulk Raman spectra presents additional challenges in accurately identifying oxidation and spin states, as these are affected by the varying characteristics of CytC molecules.
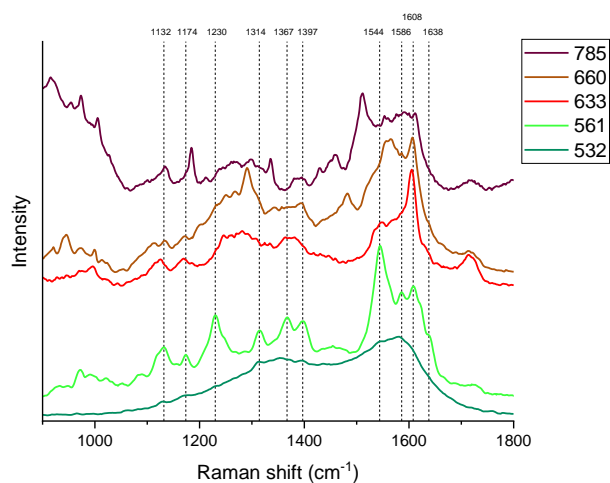
4.2.3. SERS of CytC

Figure 27 SERS spectra of CytC solution mixed with 60 nm AuNP using multiple laser wavelengths. The vertical lines represent the most prominent peaks found in the literature (Table 6).

In the subsequent phase of the study, a solution of CytC combined with 60 nm gold nanoparticles (AuNPs) was examined, utilizing various laser wavelengths to explore variations in peak intensities and positions (Figure 27).

It was observed that the 561 nm laser wavelength yielded the optimal signal-to-noise (S/N) ratio. Additionally, a range extending from 561 nm to 660 nm was found to be favorable for achieving a satisfactory S/N ratio, suggesting the effectiveness of this wavelength range in this particular system. Conversely, the lasers of 532 nm and 785 nm were noted to deliver less impressive S/N ratios.

Despite its lower S/N ratio, the highest signal intensity was recorded by the 532 nm laser. This outcome is consistent with the absorbance characteristics of CytC and the recognized enhancement region of AuNPs. Given the Soret band of CytC at 408 nm, the Q band at 530 nm, and the AuNP enhancement region between 500 nm and 800 nm, these findings were in alignment with theoretical predictions.

A further differentiation among the lasers was observed in their proximity to the resonance of CytC. Lasers operating at 633 nm, 660 nm, and 785 nm, similar to those in the previous normal Raman setup, exhibited more muted peaks for the heme unit. In contrast, an amplification of peaks within the 1180 cm^{-1} to 1350 cm^{-1} range, likely attributable to the peptide backbone of CytC, was observed[122]. This effect was even more pronounced in the SERS environment, where particularly the 660 nm laser showcased heightened peptide peaks compared to resonant Raman observations.

Table 6 Comparison of SERS CytC peaks in literature and measured sample.

SERS signals in cm^{-1}					Band assignment
532 nm[121]	532 nm[123]		Our result	Our result	
Oxidized (HS)	Oxidized	Reduced	532	561	
1131	1130	1130	1128	1132	v_s(pyr half-ring)
1166	1172	1172	1171	1174	v_s(pyr half-ring)
1232			1232	1230	δ(CH)
1315	1317	1316	1312	1314	δ(CH)
1379	1373	1363	1352,1374	1367	v_s(pyr half-ring)
1401	1403	1400	1394	1397	v(pyr quarter-ring)
1569	1569		1563		v_{as}(CC)
1580 (LS)	1585	1549	1546,1579	1544,1586	v_{as}(CC)
1628	1638	1608		1608,1638	v_{as}(CC)

In the comparative analysis conducted using the 532 nm and 561 nm lasers within the scope of SERS spectroscopy, a similarity was observed between the peaks detected and those recorded in existing literature (Table 6). The selection of the 561 nm laser for this analysis was based on its enhanced signal-to-noise ratio.

As was the case with the powder sample, a modest variability in peak positions was exhibited by the 532 nm laser, along with other lasers used, remaining within a range of less than 10 wavenumbers (Figure 22). Such variations, in line with prior observations, are attributed to subtle differences in the characteristics and performance of each laser.

Variations in peak intensity were inherently present across the laser spectrum. These discrepancies are likely the result of each laser's distinct ability to excite various vibrational modes as explained before.

The determination of the iron ion's oxidation state faced similar challenges, with the presence of concurrent peaks representing both oxidized and reduced states in certain laser spectra. Sometimes, slight shifts in peak positions resulted in the iron oxidation state peak appearing at an intermediate position, creating uncertainty in its identification. This phenomenon was particularly noticeable in the 561 nm laser spectrum.

In line with observations from the powder sample, the complexity inherent in bulk SERS spectra adds to the difficulty in accurately determining oxidation and spin states, further complicated by the presence of various CytC molecules.

For establishing a consistent reference in DONA and aggregate measurements, the 660 nm laser has been selected, as it was the primary laser engaged for these specific assessments.

4.2.4. SERS Spectra of Single CytC using DONAs
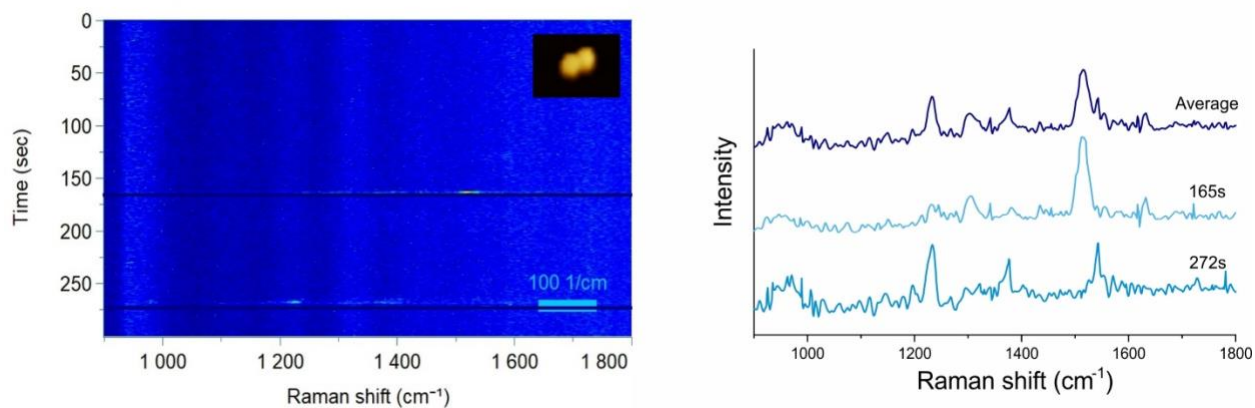
Figure 28 Left) A heat map of the time series measurement of a single DONA dimer. Inset: AFM image (325 nm x 240 nm, WxH) showing a single DONA with CytC. Right) Collected spectra from the instance seen in the measurement at different time stamps (horizontal dark blue lines in the heat map) and on top the average of the spectra.

In this phase of the analysis, single-molecule spectra were acquired from individual DONAs. The signals from these dimers were observed to be transient, typically lasting between one to three seconds, and occasionally extending up to thirty seconds (Figure 28). This transient behavior might be attributed to the CytC molecule moving in and out of the hotspot, or potentially due to the formation of new nano hotspots resulting from the high temperature-induced melting of gold nanoparticles caused by laser interaction.

Figure 29 A closer look at the collected spectrum of the DONA dimers. The orange lines represent the peaks observed in the reference sample and in literature. The purple lines represent the peaks observed in the reference sample and our dimer spectra.

When the signals were averaged over their entire observable duration, it was noted that although some individual spectra displayed identifiable CytC fingerprint peaks, no single spectrum encompassed all these peaks (Figure 29). This variation could be due to the specific orientation of the CytC molecule within the hotspot, which may influence the enhancement of different vibrational states.

In the analysis of the collective data, a more comprehensive set of CytC fingerprint peaks was evident, which corresponded closely with the SERS spectrum obtained using the 660 nm reference laser. Furthermore, within the spectral figures presented in this study, peaks denoted by purple-colored lines

were observed, which, although clearly present in our findings, have either not been previously identified or assigned in the existing literature.

Figure 30 Different time stamps from DONA dimer spectrum 5 to show the shift that occurs in the region between 1269 to 1281.

In the further analysis of dimer spectra, the focus was placed on identifying the oxidation and spin states and observing any transitions between these states. The task of pinpointing these states in the aggregate spectra was complicated by minor variations in peak positions, typically around 10 wavenumbers. A specific shift observed in the spectra, from approximately 1265 cm^{-1} to 1277 cm^{-1}, was noted to last for about 5 seconds before reverting to 1265 cm^{-1} (Figure 30). While the main peaks indicative of oxidation and spin states were discernible in the aggregate spectra, this shift did not correspond to any clearly identified states, but it is in the region for protein backbone more specifically Amide III band.

## 4.2.4.1.   SERS Spectra of CytC using Aggregates of DONAs
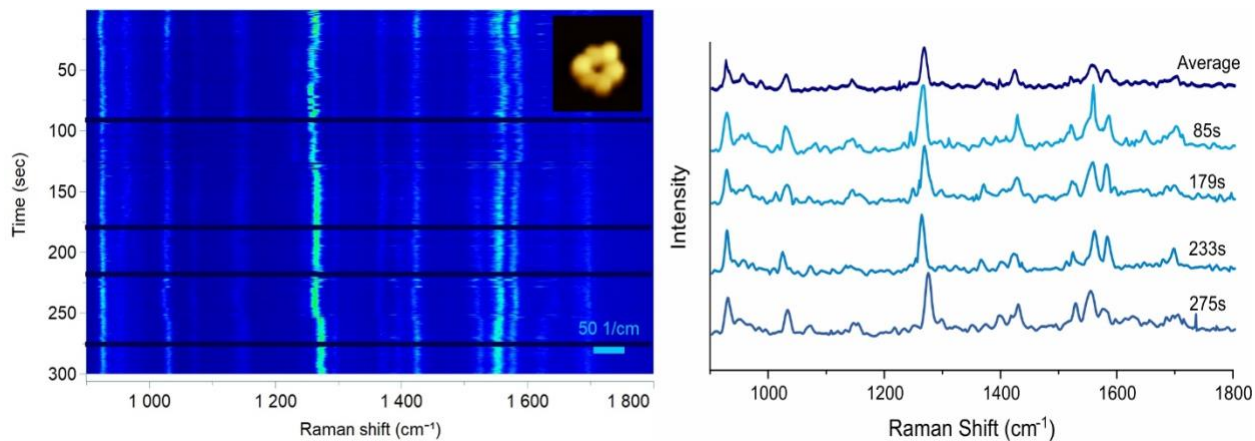
Figure 31 Left) A heat map of the time series measurement of a single DONA aggregate. Inset: AFM image (290 nm x 310 nm, WxH) showing a DONA aggregate. Right) Collected spectra from the instance seen in the measurement at different time stamps (horizontal dark blue lines in the heat map) and on top the average of the spectra.

For the measurements involving aggregates, multiple CytC spectra were collected from small aggregates consisting of DONA clusters, typically comprising 8-12 nanoparticles. The emission signals from these aggregates were observed to have a notably longer duration, in some cases lasting the entire five-minute measurement period (Figure 31). This prolonged signal duration might be attributed to a larger number of molecules in each aggregate, potentially up to six CytC molecules, or to the combined hotspot area of the aggregates that maintains a consistent level of single molecule enhancement. It is probable that both these factors contribute to this observation.
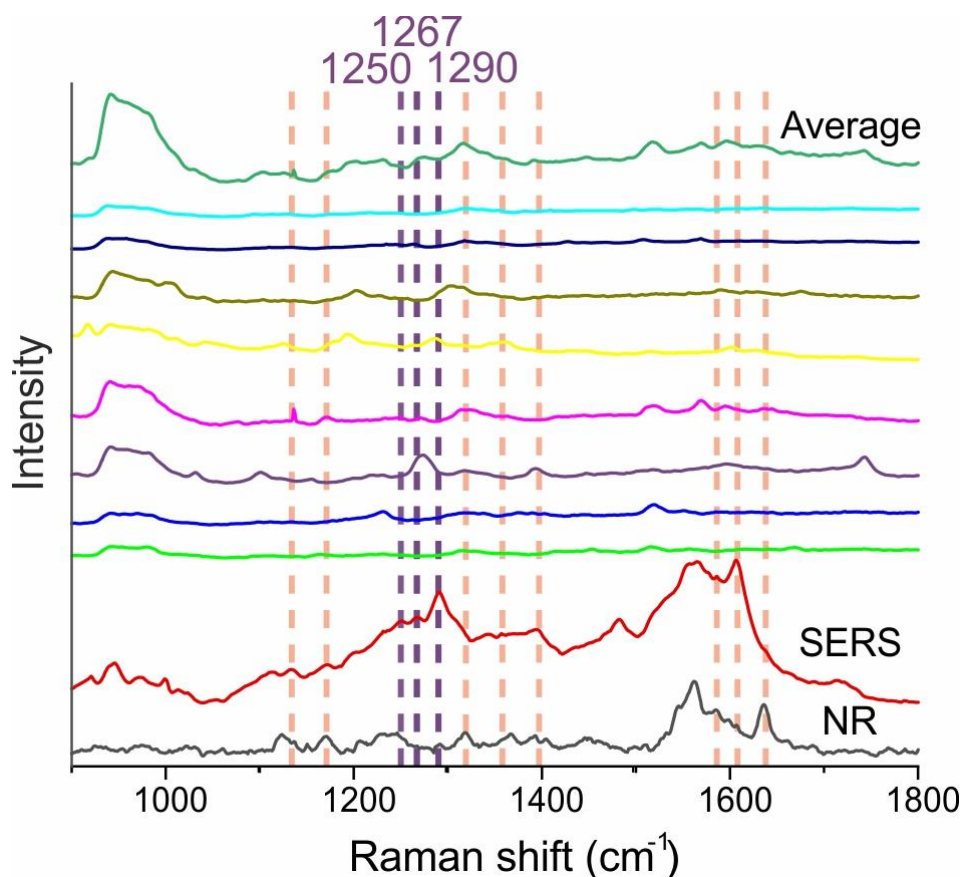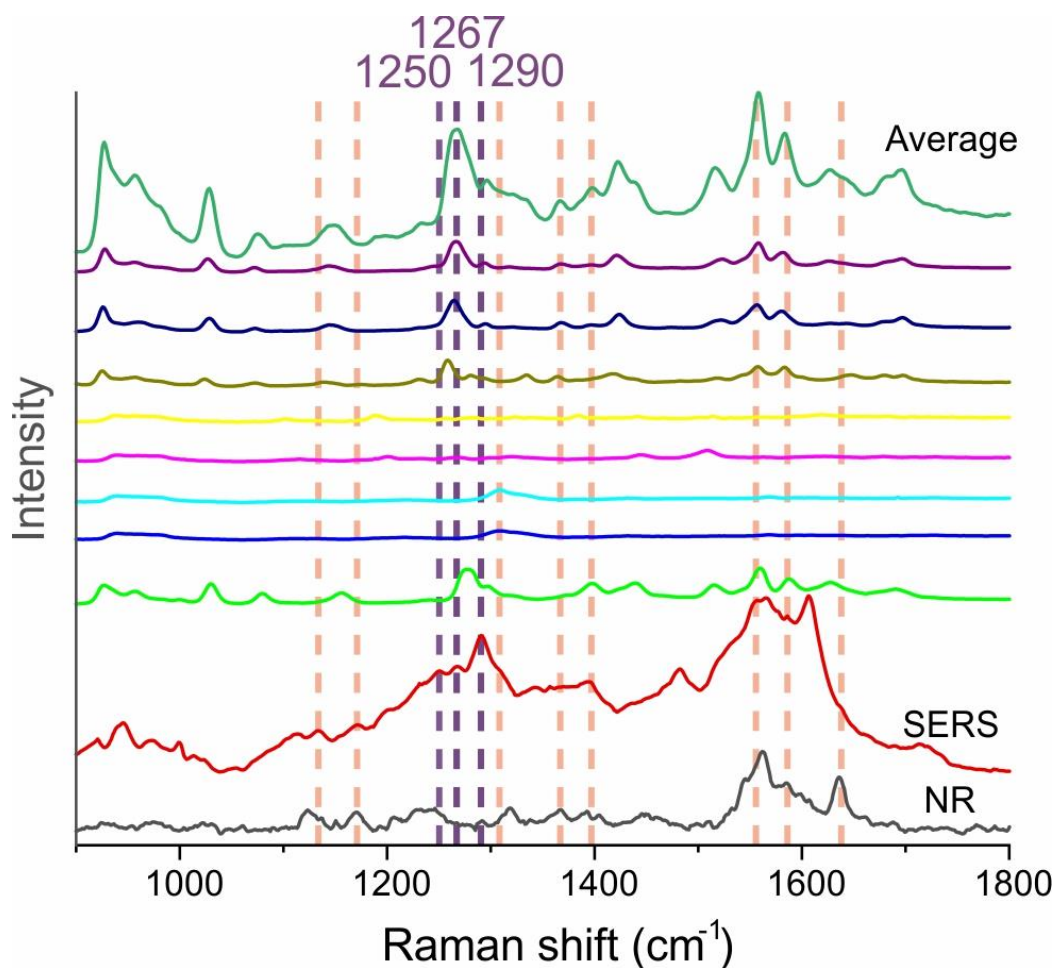
Figure 32 A closer look at the collected spectrum of the DONA aggregates. The orange lines represent the peaks observed in the reference sample and in literature. The purple lines represent the peaks observed in the reference sample and our aggregate spectra.

When the signals were averaged over the observed period, it was noted that individual spectra displayed some recognizable CytC fingerprint peaks, with some spectra even exhibiting multiple such peaks. At the aggregate level, the combined spectra revealed a broader range of CytC fingerprint peaks, which closely matched the SERS reference. Additionally, within the spectral figures of this study, peaks indicated by purple-colored lines were observed, which, although present in the measurements, have either not been previously identified or assigned in existing literature (Figure 32).
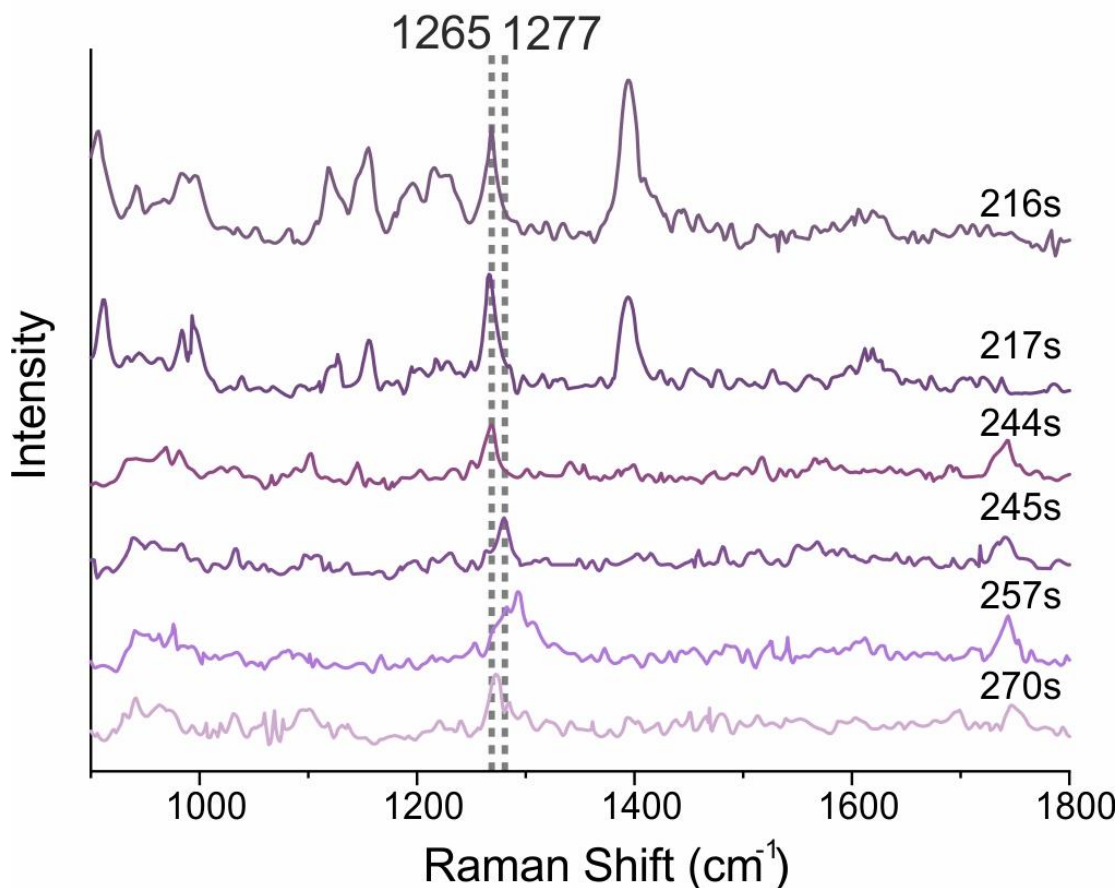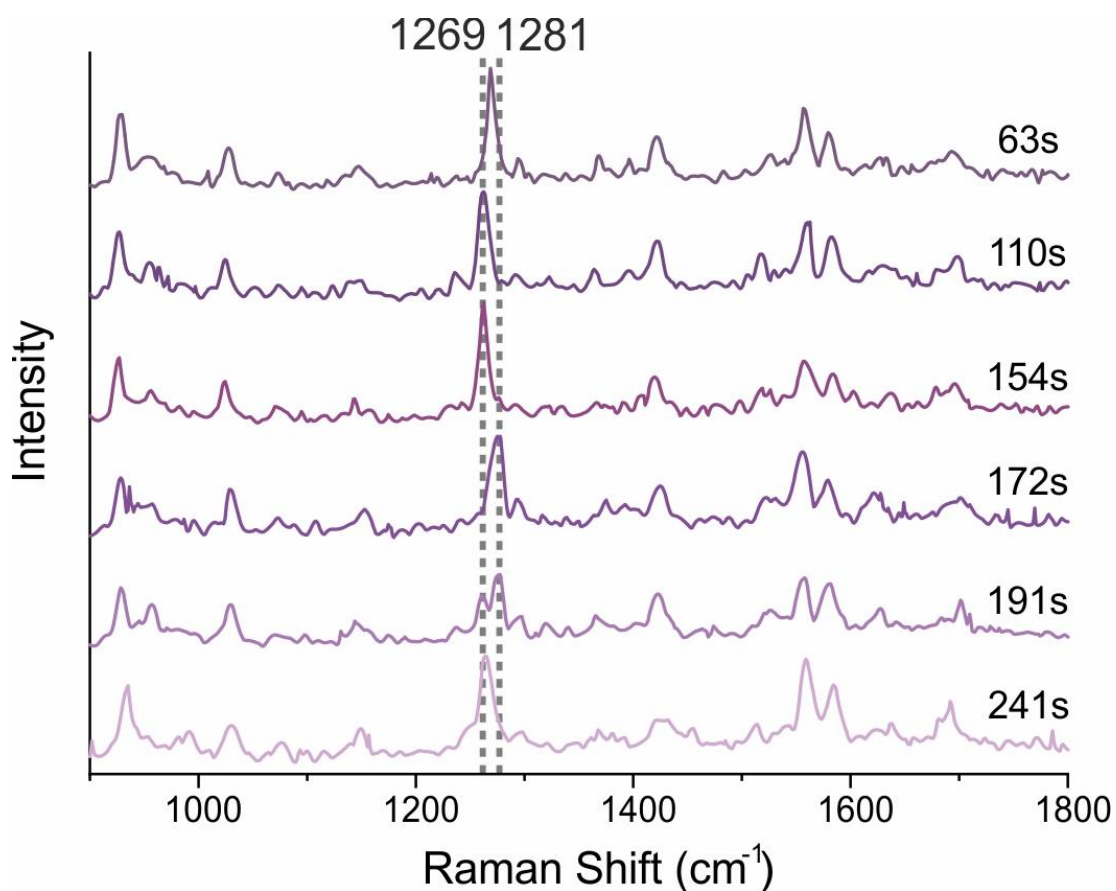
Figure 33 Different time stamps from DONA aggregate spectrum 8 to show the shift that occurs in the region between 1269 to 1281.

In the further analysis of the aggregate spectra, a methodology similar to that used with the dimer spectra was employed, focusing on identifying the oxidation and spin states and observing any transitions between these states. As observed in the dimer results, pinpointing these states in the aggregate spectra was complicated due to minor variations in peak positions, typically around 10 wavenumbers. A notable shift was recorded, where the peak position moved from approximately 1269 cm-1 wavenumbers to 1281 cm$^-$ ^{1} wavenumbers, lasting about 40 seconds before returning to 1269 cm^{-1} wavenumbers (Figure 33). Although the primary peaks indicative of oxidation and spin states were present in the aggregate spectra, this specific shift did not correspond to any identifiable states, but it is in the region for protein backbone more specifically Amide III band.

4.2.4.2.   Analysis of SM CytC

In the analysis of CytC through SERS, a detailed interpretation of the SERS spectra, reveals profound insights into the protein's structural and dynamic properties. Starting in the region of 900-950 cm^{-1}, we typically observe peaks associated with the out-of-plane ring breathing modes of the heme group. These peaks offer crucial information about the heme environment and its interactions within the protein

matrix[124]. Progressing to around 1000 cm^{-1}, there is a peak often attributed to the ring breathing of phenylalanine, shedding light on the environment surrounding phenylalanine residues in the protein[125].

At approximately 1040 cm^{-1}, a peak is observed, likely corresponding to C-C stretching vibrations, indicative of the protein's backbone structure. This provides valuable information about the overall conformation of CytC[124]. The peak near 1100 cm^{-1} is assignable to C-N stretching coupled with N-H bending, typically related to the protein's secondary structures like α-helices and β-sheets[126].

The range between 1120-1170 cm^{-1} is particularly interesting, encompassing C-H bending vibrations of methyl and methylene groups, offering insights into the conformation and environment of CytC's aliphatic side chains. A crucial region spans from 1200 to 1300 cm^{-1}, where we detect the amide III vibrations—a combination of N-H bending and C-N stretching. This region is highly sensitive to the protein's secondary structure, providing detailed insights into helical and sheet formations in CytC[127].

At around 1350 cm^{-1}, the peak typically arises from CH bending modes, reflecting information about the tertiary structure and the aliphatic amino acid residues' environment within CytC[127]. Between 1360 and 1370 cm^{-1} is the pyrrole ring stretching which can be attributed to the heme oxidation state[121]. Moving towards 1450-1460 cm^{-1}, peaks attributable to CH bending vibrations are observed, which are indicative of the dynamics of methylene groups in the protein structure[127].

A significant peak near 1580 cm^{-1}, often associated with the stretching vibrations of the heme group, is pivotal for understanding the state of the heme iron and its interaction with the surrounding protein matrix[50]. The amide I vibrations, primarily C=O stretching, appear around 1600 cm^{-1}. This peak is critical for assessing the protein's secondary structure, offering insights into the conformational state of CytC. Finally, peaks above 1600 cm^{-1} may correspond to aromatic amino acids like tyrosine and tryptophan, reflecting their environmental interactions within the CytC molecule[128].

Both the dimer and aggregate spectra were analyzed with the aim of identifying oxidation and spin states of CytC, as well as observing potential shifts between these states. In both cases, slight variations in peak positions were noted, typically around 10 wavenumbers. These variations posed challenges in precisely identifying the oxidation and spin states.

In the dimer spectra, transient signals were observed, lasting between one to three seconds and occasionally up to thirty seconds. This transient nature was attributed to the movement of the CytC molecule in and out of the hotspot or the formation of new nano hotspots. In contrast, the aggregate

spectra exhibited notably longer emission signal durations, sometimes lasting the full five-minute measurement period. This extended duration in aggregates was likely due to the higher number of molecules in each aggregate or the collective hotspot area of the aggregates.

In both dimer and aggregate spectra, individual spectra showed recognizable CytC fingerprint peaks, but no single spectrum contained all of these peaks. This was attributed to the specific orientation of the CytC molecule within the hotspot. The collective data from the aggregates presented a broader range of CytC fingerprint peaks, aligning well with the SERS reference. Additionally, both spectra contained peaks marked with purple-colored lines in the spectral figures, which were present in the measurements but not previously assigned in the literature.

A specific peak shift was observed in both dimer and aggregate spectra. In the dimer spectra, a shift from roughly 1265 wavenumbers to 1280 wavenumbers was observed, lasting about 5 seconds before reverting. In the aggregate spectra, a similar shift occurred from approximately 1262 wavenumbers to 1277 wavenumbers, lasting about 40 seconds before returning to 1265 wavenumbers. While the main peaks for oxidation and spin states were evident in both spectra, these shifts did not correspond to any discernible states.

It is important to consider the potential advantages of using an aggregate system over a DONA setup. The aggregate system, comprising clusters of multiple DONAs, offers enhanced signal stability and duration compared to single DONA configurations. The longer emission signals observed in the aggregates, sometimes lasting the entire measurement period, suggest a more sustained interaction within the hotspot. This could be due to the increased number of CytC molecules in each aggregate, which not only enhances the likelihood of capturing signals but also potentially increases the diversity of interactions within the hotspot area. This results in a more robust and consistent signal, which is crucial for detailed spectral analysis and accurate identification of specific molecular states.

Furthermore, the broader range of CytC fingerprint peaks observed in the aggregate spectra points to a more comprehensive representation of the molecule's vibrational states. This broader spectrum is likely a result of the collective hotspot area provided by the aggregates, enhancing the overall sensitivity and detection capabilities of the system.

The aggregate system also potentially mitigates the effects of transient signal behaviors and orientation-dependent variations seen in single DONAs. By having multiple interaction points within the aggregate, there is a higher probability of capturing a range of orientations and states of the CytC molecules, leading to a more complete spectral representation.

The introduction of single-molecule surface-enhanced Raman spectroscopy (SM-SERS) has revolutionized our capability to study molecular systems in-depth, offering an intricate look into individual entities like proteins. The collaboration of SM-SERS with a gold nanopore is a testament to the advancements being made in this realm. Such a combination, as demonstrated by Juan Zhou and colleagues[129], offers a fascinating window into single molecule protein segments, potentially propelling nanopore towards single-molecule (SM) protein sequencing.

Zhou's method of identifying segments of SM protein sequentially using a surface-enhanced Raman scattering-active plasmonic nanopore indicates a significant direction for SM protein sequencing. By driving CytC SMs through a gold nanopore via electric field force and observing the translocation behavior through dynamic SM SERS, we gain deeper insights into protein dynamics. This approach brings to light the pivotal role of hotspot positioning and strength in SM-SERS investigations.

The arc of progress since Nie and Emory's pioneering demonstration of single-molecule SERS in 1997 is evident[130]. From the dawn of observing individual molecular behavior, current studies emphasize hotspot enhancement and the crafting of nanoscale devices for improved signal consistency. The realm has also seen efforts directed towards creating innovative nanostructures[131] with techniques such as nanosphere lithography and electron beam lithography taking the lead. Simultaneously, there's a push for economical solutions, with a shift in focus towards materials like aluminum for plasmonic properties.

Yet, with all these advancements, the journey remains tumultuous. While innovative strategies like "shell-isolated nanoparticle-enhanced Raman spectroscopy" (SHINERS) address some limitations[132], they aren't without their caveats. Furthermore, the intricacies of data interpretation in SM-SERS persist as a challenge, although the amalgamation of machine learning offers hope for refined spectral analysis[133].

Proteins, given their intricate nature, present their own set of challenges for SM-SERS. There's also the exciting prospect of real-time monitoring of protein interactions through SERS tags[134]. Integrative approaches, combining SM-SERS with tools like atomic force microscopy, show promise in unraveling mysteries around protein-ligand interactions and folding dynamics[135]. However, the specter of inconsistent SERS substrates looms large, and devising a universal method for protein studies remains elusive[136].

This is where the DONA offers a unique perspective. By eliminating the need for external labels and harnessing the precision of DNA origami, the system promises enhanced authenticity in SM-SERS studies. Its versatility is not just rooted in its label-free approach but also in its adaptability. The modularity of DNA origami ensures a customizable approach, suited to address diverse research queries. By reducing

potential experimental artifacts and improving the robustness of the system, this method serves as a promising bridge over some of the existing gaps in the field.

In the rapidly evolving landscape of single-molecule surface-enhanced Raman spectroscopy (SM-SERS), the ability to distinctly observe peptide backbone peaks stands as a significant advantage. Our system offers this unique capability, providing an unparalleled perspective beyond the usual CytC resonance. The inherent versatility of our method, exemplified by its precision in detailing such peaks, can potentially revolutionize the way molecular behaviors are understood at the single-molecule level.

4.2.4.3.   Analysis of Amide III Band

Amide I and Amide III bands have long been critical markers in protein studies, owing to their sensitivity and specificity. The Amide III band in proteins typically appears in the Raman and infrared spectra within the wavenumber range of 1200 to 1350 cm^{-1}. This band primarily arises from the combination of N-H bending and C-N stretching vibrations of the peptide backbone, and its exact position within this range can vary depending on the specific secondary structures present in the protein, such as α-helices (1300-1350 cm^{-1}) and β-sheets (1230-1240 cm^{-1}), and random coils (1240-1260 cm^{-1}).

A review by A. Rygula et al. titled "Raman spectroscopy of proteins" elaborates on the importance of these bands in understanding protein secondary structures[137]. These bands, which primarily arise from the peptide bonds within proteins, offer rich information on the conformational states and behavior of the proteins[138].

UVRR spectroscopy has shown particular effectiveness in studying the Amide III bands, known for its enhanced sensitivity due to resonance enhancement when the excitation wavelength matches the electronic transition of the molecule[139]. However, UVRR has limitations, such as the risk of photodegradation[140] and an averaging effect over ensemble measurements that may obscure detailed molecular behaviors[141].

UVRR spectroscopy boasts enhanced sensitivity, a feature primarily attributed to the resonance enhancement that transpires when the excitation wavelength is in harmony with an electronic transition of the molecule[142]. This resonance effect intensifies Raman scattering, enabling the detection of even subtle changes in molecular structures, this sensitivity is complemented by UVRR's specificity[143]. By targeting distinct electronic transitions, UVRR can selectively amplify certain vibrational modes, offering a clear vantage point for observing bands, particularly the likes of amide III. However, one must be wary when using UVRR, as the ultraviolet light employed carries the inherent risk of photodegradation or photobleaching of the sample over extended measurements[144]. Additionally, while UVRR provides a broad

overview of the sample, focusing on ensemble measurements, its perspective averages out across the entire sample. This averaging can sometimes obscure minute but crucial molecular behaviors. Furthermore, while UVRR is versatile in terms of the range of samples it can analyze, it might demand adjustments or calibrations contingent on the specific molecule or transition under scrutiny.

In contrast, our dimer and aggregate system, endowed with its inherent plasmonic properties, offers a heightened sensitivity, especially at the single-molecule level. Molecules in the hotspot regions of these configurations receive an amplified Raman signal, drawing a parallel to the resonance enhancement intrinsic to UVRR. However, the specificity in our system emerges from the intricately tailored design of the dimers and aggregates, ensuring a targeted enhancement of specific vibrational modes. Such specificity provides a controlled environment, particularly beneficial for delving into the intricate behaviors of proteins. One of the standout features of our system is the minimized risk of sample degradation, thanks to its design. The plasmonic properties act as a safeguard, allowing prolonged measurements without compromising the integrity of the sample. The capacity to offer insights at the single-molecule level ensures the observation of heterogeneities and nuanced behaviors that might otherwise be concealed in ensemble measurements. This granularity is complemented by the system's flexibility. The inherent modularity of the dimer and aggregate system ensures adaptability, allowing researchers to tailor the system to specific molecules or interactions. However, this system is not without its challenges. While its single-molecule resolution often simplifies spectral interpretation, occasional complexities might arise from the diverse orientations or interactions of molecules within the hotspot regions.
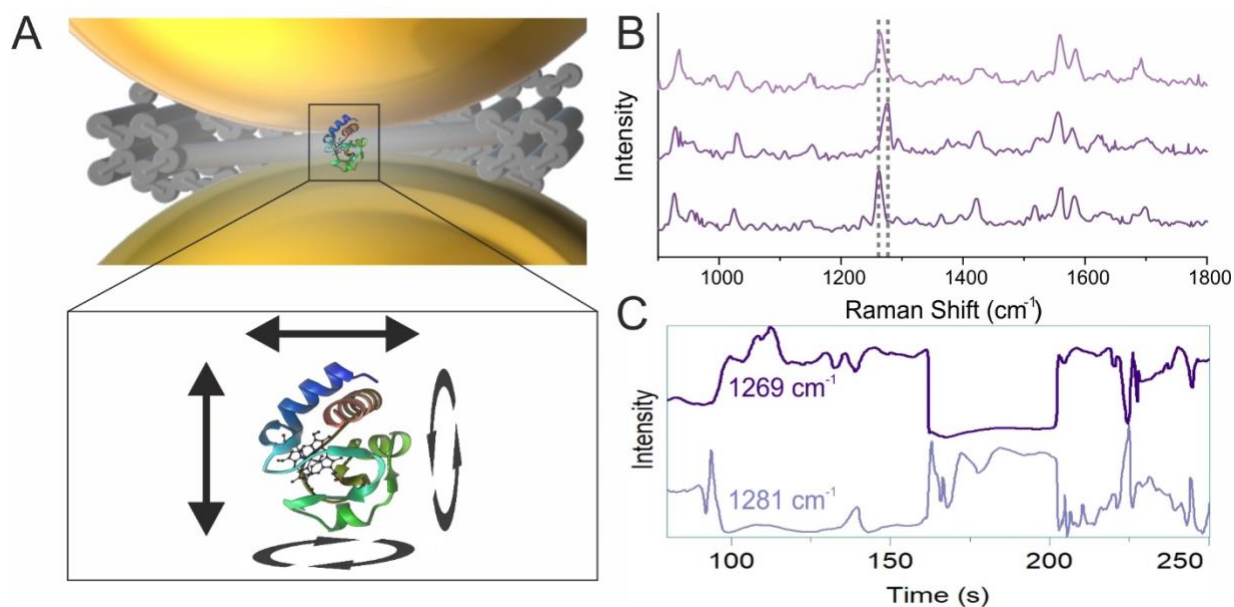
Figure 34 A) Schematic of the probable shift between α-helix and random coil of CytC in the hotspot. B) The change of intensity in time for the peak at 1265, showing the broad drops in intensity which could be attributed to the shift in structure. C) CytC spectra at different time stamps to show the peak shift between 1265 cm^{-1} and 1280 cm^{-1}.

In our analysis, a notable transient shift was observed in the amide III band's frequency, moving from approximately 1269 cm-1 to 1281 cm-1 (Figure 34B), before returning to the original frequency. While this shift falls within the characteristic range for alpha-helical structures (1265 -1300 cm-1), it's important to consider that the Amide III band reflects a complex mix of vibrational modes. The disappearance of peaks over time could indicate a reorientation of molecules within the hotspot, altering the vibrational modes that experience the greatest enhancement.

To gain further insight into the structural conformation of CytC within the aggregates, deconvolution analysis was performed on the SERS reference spectrum (Figure 35) and the average spectrum obtained from the DONA aggregates (Figure 35). The deconvolution analysis revealed three main components in the Amide III band region:

- **1250 cm-1:** Random coil conformations.

- **1269 cm-1:** Alpha-helical secondary structure.

- **1290 cm-1:** Alpha-helical secondary structure.

Table 7 Deconvolution Analysis of the Amide III Band.

Raman Shift (cm^{-1})	SERS ref. Area %	DONA agg. Area %	Amide III band
1250	36.8	4.8	Random coils
1269	14.3	54.9	Alpha-helix
1290	48.8	40.4	Alpha-helix

The deconvolution analysis offers valuable insights into potential structural changes of CytC upon interaction with the DONA aggregates (Figure 35). The decrease in the random coil component (1250 cm-1) from 36.8% in the SERS reference to 4.8% in the DONA aggregates suggests a potential stiffening of CytC's structure. Conversely, the significant increase in the relative abundance of the alpha-helical components (1269 cm-1 and 1290 cm-1) in the DONA aggregates compared to the reference suggests a more prominent alpha-helical character in bound CytC (Table 7).

Figure 35 Left) Deconvolution analysis of the Amide III band. Black line: SERS reference spectrum. Red line: Sum of the deconvoluted peaks. Green lines: Individual deconvolute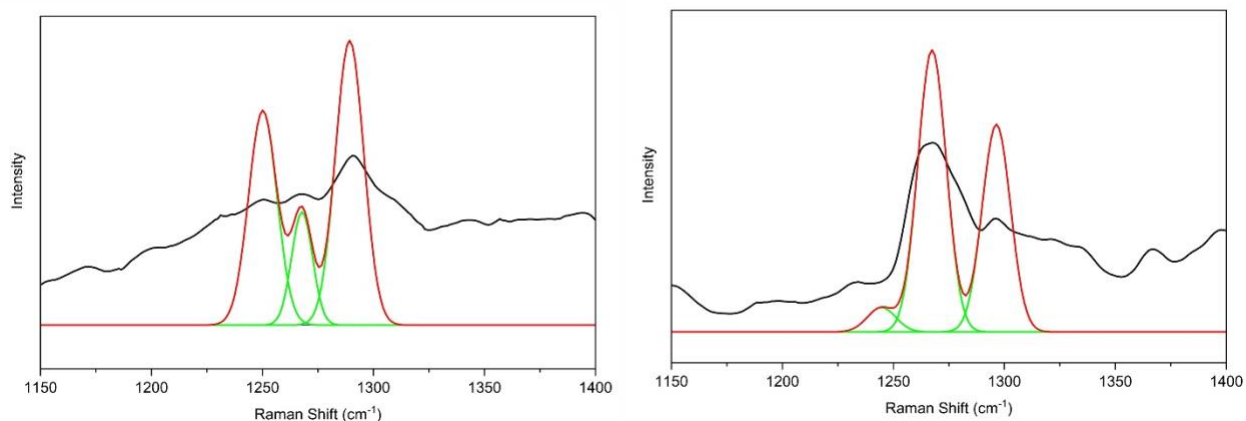d peaks corresponding to 1250 cm^{-1} (random coil), 1269 cm^{-1} (alpha-helix), and 1290 cm^{-1} (alpha-helix). Right) Deconvolution analysis of the Amide III band. Black line: DONA aggregates average spectrum. Red line: Sum of the deconvoluted peaks. Green lines: Individual deconvoluted peaks corresponding to 1250 cm^{-1} (random coil), 1269 cm^{-1} (alpha-helix), and 1290 cm^{-1} (alpha-helix).

Several factors could contribute to such dynamic behavior within our SERS measurements. Within the SERS hotspot, individual protein molecules might reorient or diffuse, altering their interaction with the electromagnetic field and contributing to peak shifts (Figure 34A). Interactions between the protein and the metal surface can involve electron transfer processes, potentially affecting the protein's electronic state and vibrational frequencies. Finally, even minor environmental fluctuations in temperature around the SERS hotspot can influence protein conformation and interactions with the metal surface, possibly contributing to the observed transient peak shift.

Additionally, in the DONA aggregate system, the observed peak shifts could arise from different CytC molecules within the aggregate experiencing varying degrees of enhancement. This variation stems from the likelihood of multiple CytC molecules being present in the hotspot, with their orientations and diffusion determining which molecule receives the greatest enhancement at a given moment. Notably, the transient decrease in the 1269 cm-1 peak intensity around 160 s, coinciding with the emergence of the 1281 cm-1 peak (Figure 34C), suggests that the spectra likely originate from a single CytC molecule. This is due to the matching intensities of the peak decrease and increase. The persistent signal might reflect an increased probability of a single CytC molecule occupying the highest enhancement region within the hotspot due to the presence of multiple CytC molecules within the DONA aggregate.

While the above-mentioned processes offer plausible explanations for the observed peak shifts, further analysis is needed to provide a definitive interpretation. Importantly, our measurements were conducted in a dry state, which limits the observation of protein folding dynamics. Future studies in solution environments, combined with the introduction of controlled stimuli like denaturants or temperature changes, could provide a more complete picture of protein conformational changes detectable through our technique.

Unlike UV resonance Raman techniques, which can lead to protein denaturation, our system maintains the integrity of the protein structure. This is evident from the sharpness of the amide III peaks throughout the measurement, indicating no denaturation of CytC. This capability allows for accurate monitoring of real-time conformational changes and underscores the system's utility in detailed protein studies where preserving the native structure is crucial.

Overall, the dynamic shift in the amide III band frequency, coupled with the maintenance of peak sharpness, underlines the potential of our system in tracking real-time conformational changes in proteins. Such insights are vital for understanding protein functionality and interactions within various environments, offering a window into the dynamic nature of protein structures and their molecular interactions.

4.2.5. Biosensing

In the realm of biosensing, an innovative approach was pictured to harness the capabilities of DONAs for the detection of SARS COV-2 DNA. The initial concept was centered around utilizing DONAs in a sandwich assay format, where the target SARS COV-2 DNA would be captured and identified through Raman reporters. Specifically, the idea was to employ TAMRA-labeled AuNPs on the DONAs as the Raman reporters.

The landscape of point-of-care (POC) diagnostics is rapidly evolving, marked by significant advancements in technology and methodology. These developments are pivotal in providing rapid, accurate, and accessible healthcare solutions, especially in resource-limited settings[145,146,147].

A key area of innovation in POC diagnostics is the integration of microfluidics and nanotechnology. Microfluidic technologies have revolutionized the field by enabling the miniaturization and integration of complex laboratory processes. This has led to the development of compact, efficient, and less costly diagnostic devices suitable for POC settings[148].

Further advancements are seen in the realm of biosensing technologies, particularly in their application to paper-based microfluidic systems. These technologies have been incorporated into user-friendly, cost-effective POC diagnostic devices. The simplicity and affordability of these paper-based systems make them ideal for widespread use, especially in areas with limited access to conventional laboratory facilities[149].

The need for rapid detection and high sensitivity in POC testing is also a crucial aspect. The ability to quickly and accurately detect diseases or medical conditions at the point of care is essential for timely treatment and disease management, especially in remote or underserved areas[145].

An emerging trend in POC diagnostics is the use of smartphone technology, which enhances accessibility and connectivity. Smartphone-based technologies are democratizing POC diagnostics, allowing for remote data analysis and easier sharing of medical data. This integration of mobile technology in healthcare is transforming POC diagnostics into a more connected and patient-centric model[150].

Nanomaterials have also become a critical component in POC devices. The application of nanomaterials in developing sensitive and specific POC devices capable of detecting pathogens in various types of samples, including blood and produce. This use of nanotechnology enhances the detection capabilities of POC devices, making them more reliable and efficient[151].

The integration of molecular diagnostics in POC testing shows the potential for combining molecular diagnostics with mobile technology. This approach is particularly beneficial in the diagnosis of infectious diseases, offering a high level of accuracy and efficiency in POC settings[152].

The envisioned application of our system was particularly in a point-of-care setting, utilizing a Lateral Flow Assay (LFA) system. This setup promised the advantage of detecting viral DNA without the need for amplification processes, thanks to the low limit of detection offered by the Raman reporters on the DONAs. The sensitivity of this system was so refined that it was theoretically capable of detecting single DONA molecules on a surface, making it a highly efficient tool for rapid and accurate detection.
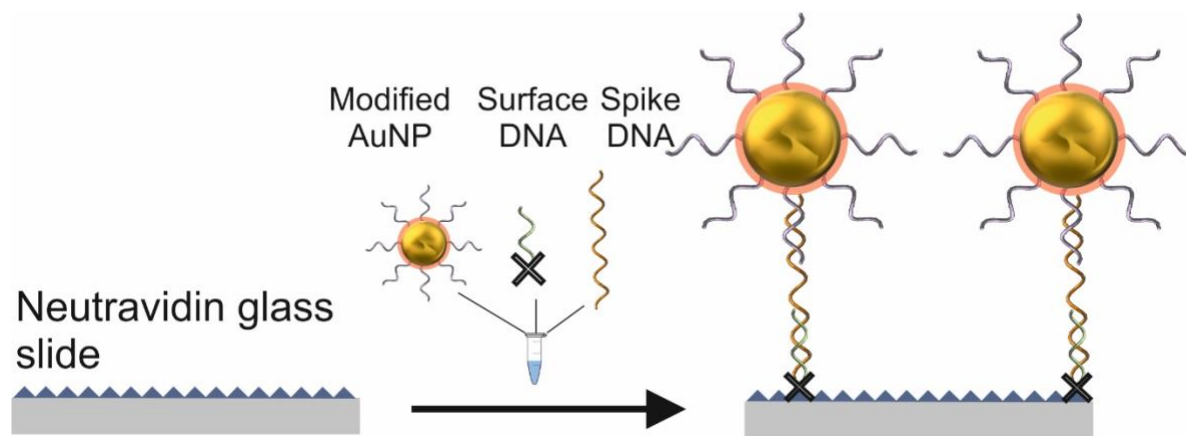
Figure 36 Schematic of sandwich assay.

Practical challenges were encountered regarding the interaction of DONAs with the assay surface. This necessitated a revision of the initial plan to ensure a more reliable and consistent starting point for the assay. As a result, the strategy was adjusted by replacing DONAs with fully coated TAMRA-labeled AuNPs (Figure 36). These nanoparticles were equipped with partially complementary strands to the SARS COV-2

DNA with an internally modified TAMRA molecule (Table 3). In tandem, the surface of the assay was prepared with another set of partially complementary strands with biotin modification at the 3' end (Table 3). This design effectively sandwiches the target SARS COV-2 DNA strand in between the two sets of complementary strands. Such an arrangement not only ensured a more stable and predictable interaction with the surface but also retained the core advantage of the system – the efficient detection of SARS COV-2 DNA.

Following the adaptation of our biosensing system for SARS COV-2 DNA detection, further steps were taken to validate and refine the methodology. Initially, AFM was employed as a tool to ascertain the functionality of the system (Figure 37). The primary objective was to verify the presence of AuNPs on the assay surface, which would indicate the operational success of the system.
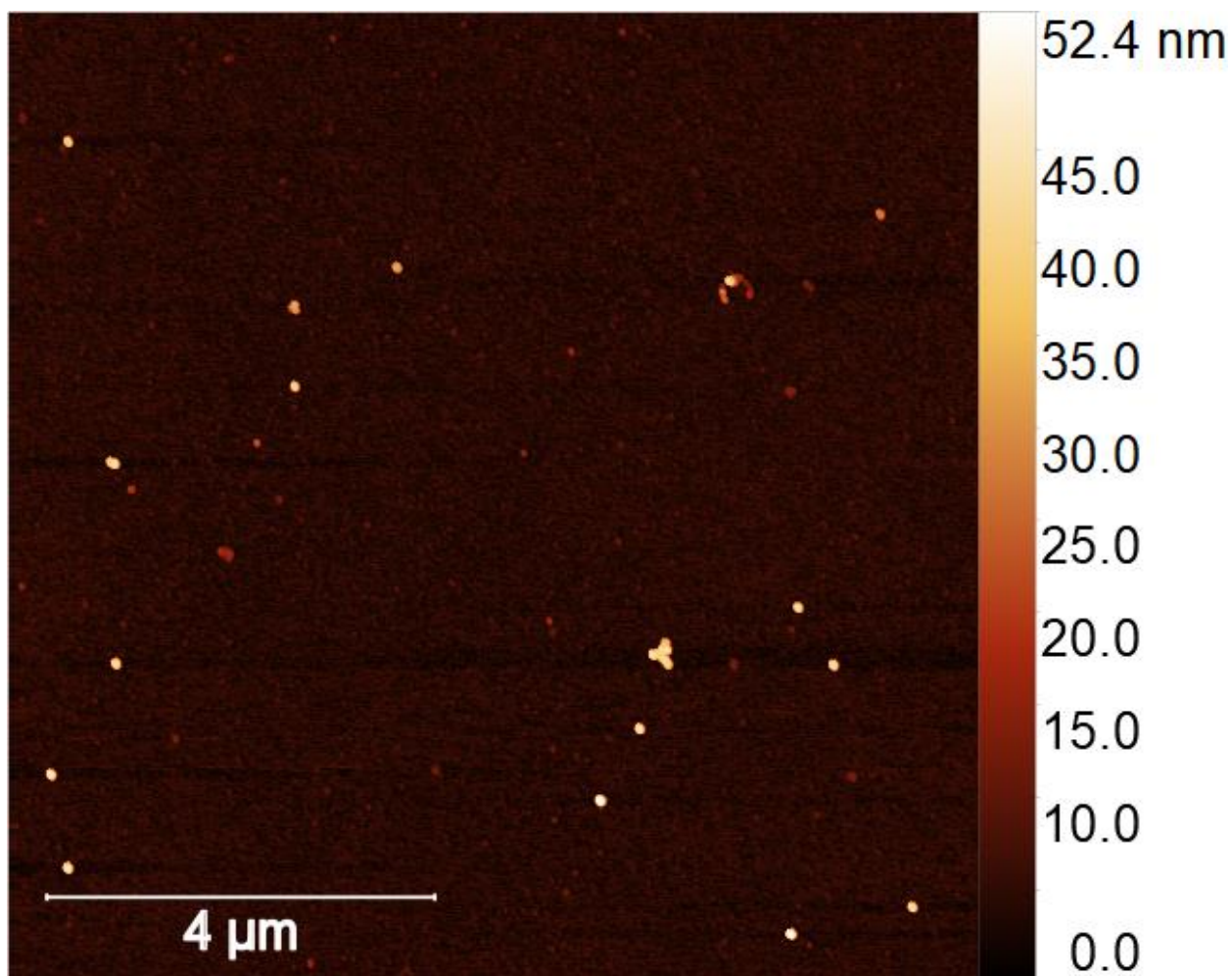
Figure 37 AFM image showing the AuNPs on the surface.

Upon confirming the presence of AuNPs, the next phase involved deciding on the most effective approach for quantitative analysis. Two options were considered: either to continue using AFM for counting the number of AuNPs in each image or to switch to Raman mapping for detecting the TAMRA signal. Initially, it was decided to proceed with the AFM method.
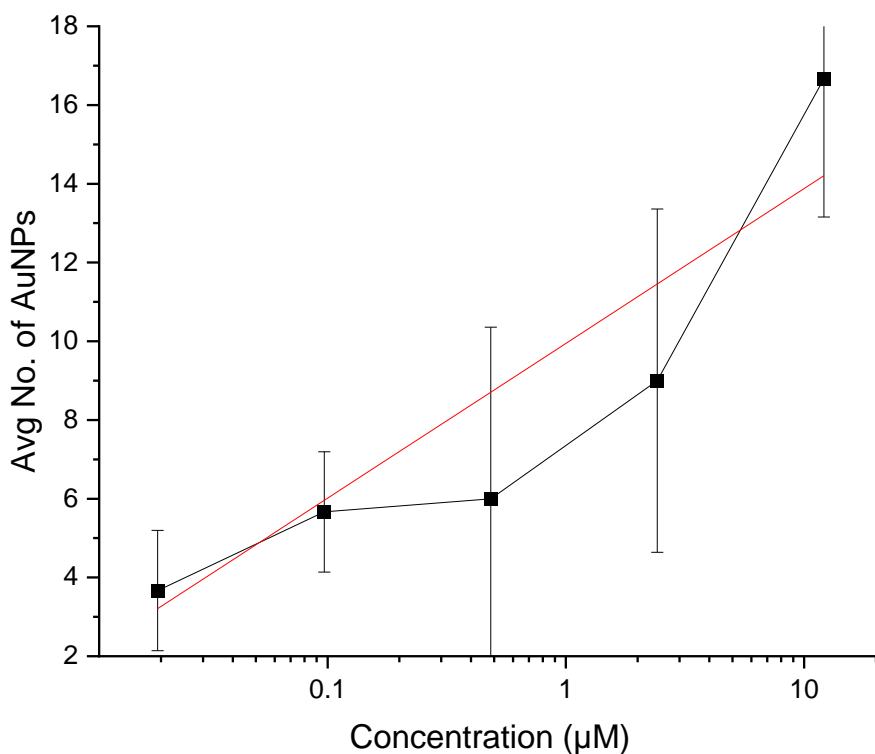
Figure 38 Concentration dependence plot of the number of AuNPs counted on the surface for each concentration.

A concentration dependence assay was conducted using AFM, which revealed a correlation between the concentration of the target DNA and the number of AuNPs observed on the surface (Figure 38). As the concentration increased, there was a noticeable rise in the number of AuNPs. However, it was also observed that the standard deviation in the number of AuNPs increased with higher concentrations. This variability could be attributed to the limited field of view of AFM imaging, which results in each image capturing a different sample area, leading to inconsistencies in the data.

To overcome these limitations and enhance the efficiency and scope of the analysis, the next step involves transitioning to Raman spectroscopy. Raman spectroscopy offers several advantages over AFM, including the ability to scan larger surface areas more rapidly. This approach not only facilitates the counting of

AuNPs but also provides additional information. For instance, the intensity of the TAMRA signal can offer further insights, potentially revealing more about the binding efficiency and the distribution of AuNPs across the surface. As an optical technique, Raman spectroscopy enables the seamless transition of this biosensing approach to an actual point-of-care (POC) setting. This adaptability stems from Raman spectroscopy's non-invasive nature and its capability to provide rapid, precise molecular information without the need for complex sample preparation. Consequently, this aligns perfectly with the requirements of POC diagnostics, where ease of use, speed, and reliability are paramount.

5. Conclusion and Outlook

Central to this research has been the innovative application of DONAs in both dimer and aggregate forms, marking a significant advancement in the field of single-molecule spectroscopy.

The optimization of the DNA origami NF system stands as a cornerstone of this research. The meticulous development and refinement of these nanoscale tools have enabled an unprecedented level of detail in spectroscopic analysis. The DNA origami NF antennas, through their sophisticated design and functionality, have demonstrated an enhanced ability to detect and analyze molecular vibrations, providing insights into the molecular structure and behavior of proteins that were previously unattainable with traditional spectroscopic techniques.

A pivotal aspect of this optimization process involved fine-tuning the structural design of the DNA origami to maximize efficiency and efficacy in spectroscopic applications. This involved careful consideration of factors such as the stability of the structures, their responsiveness to various spectroscopic methods, and their ability to maintain the integrity of the protein samples under study. Through iterative design improvements, the DNA origami NF were optimized to offer an optimal balance of structural rigidity and flexibility, necessary for accurate and reliable spectroscopic analysis.

The results from this optimization phase have highlighted the versatility and efficacy of the DNA origami NF system. This system not only facilitates enhanced sensitivity and specificity at the single-molecule level but also provides a controlled environment for in-depth studies of protein dynamics. The minimized risk of sample degradation, a standout feature of the system, ensures the preservation of the protein's native structure during prolonged measurements, a critical requirement for accurate molecular characterization.

The second critical aspect of this thesis involved a detailed comparison between the DONAs in their dimer and aggregate forms, particularly focusing on single-molecule measurements of CytC. This comparative analysis has yielded insights into the distinct advantages and nuances of each system, contributing to a more comprehensive understanding of protein behavior at the molecular level.

In the analysis of single-molecule spectra, both the dimer and aggregate forms of DONAs demonstrated unique strengths. The dimer system, with its transient nature of signal emission, was instrumental in capturing rapid, dynamic changes in the molecular structure of CytC. These transient signals, although brief, were crucial in indicating momentary alterations in the protein's conformation. However, the aggregate system, characterized by its longer-lasting emission signals, provided a more sustained view of the protein's behavior. This extended duration of signal emission in the aggregates was attributed to the increased number of molecules in each aggregate and the collective hotspot area, which enhanced overall signal stability and sensitivity.

The comparative analysis also revealed that the aggregate system offered a broader range of detectable molecular states compared to the dimer system. This was particularly evident in the study of the amide III band's frequency shifts in CytC. The aggregate system's ability to maintain a longer signal duration allowed for the observation of more comprehensive sets of CytC fingerprint peaks, which were crucial in understanding the protein's secondary structure and hydrogen bonding states.

Furthermore, the study highlighted the potential dynamism within the protein structures, as evidenced by the observed transient shifts in the amide III band frequency. These shifts suggested real-time conformational changes in CytC, indicative of transitions between different protein structures. The aggregate system's ability to capture these shifts over an extended period provided valuable insights into the protein's functional dynamics and interactions within various environments.

The final aspect of this thesis focused on the detailed analysis of the Amide III band using the DONAs in both dimer and aggregate forms. This section of the research has provided significant insights into the secondary structure and hydrogen bonding states of CytC, highlighting the potential of our system in understanding complex protein dynamics.

A key observation in this study was the transient shift in the Amide III band's frequency, which was noted to fluctuate between approximately 1269 wavenumbers and 1281 wavenumbers. This fluctuation, observed over a period of about 40 seconds before returning to the original frequency, suggested dynamic alterations in the secondary structure of CytC. Such shifts indicated potential transitions between α-helix and β-sheet structures or movements towards a random coil formation. This ability to detect real-time conformational changes is pivotal in understanding the functional mechanisms of proteins and their interactions within various biological processes.

Furthermore, the shift to a higher frequency in the Amide III band, specifically to 1281 wavenumbers, implied an increase in hydrogen bonding within the protein's structure. The subsequent return to the original frequency suggested a reversible alteration in the protein's hydrogen bonding state. These observations are crucial as they provide a deeper understanding of the protein's structural dynamics and its adaptive response to environmental stimuli.

An important advantage of our system, in comparison to traditional UV resonance Raman techniques, is its capability to maintain the integrity of the protein structure without inducing denaturation. This was evidenced by the consistent sharpness of the Amide III peaks throughout the measurement period, indicating that the native structure of CytC was preserved. This feature is essential for accurate monitoring of real-time conformational changes and highlights the utility of our system in detailed protein studies.

The insights gained from this research open the door to further exploration and innovation in various aspects of molecular biology and biochemistry.

One promising area of future work involves expanding the scope of DONA applications beyond the realm of proteins to other biomolecules such as nucleic acids and complex cellular components. This expansion would further validate the versatility of DONAs in a wide array of molecular biology studies. Additionally, integrating the DONA system with other emerging technologies, such as nanofluidics or advanced microscopy techniques, could lead to more comprehensive analyses. This could enhance spatial and temporal resolution, providing deeper insights into molecular dynamics and interactions.

Longitudinal studies using the DONA system to observe protein behavior under various physiological conditions could offer invaluable data on protein dynamics over time, leading to a better understanding of protein folding, misfolding, and the molecular basis of related diseases. The insights gained into protein structures and dynamics could also inform therapeutic strategies, particularly in drug design and targeted therapy. The ability to observe proteins at a single-molecule level could aid in the development of more effective and specific drugs.

The development of user-friendly interfaces and protocols for DNA origami-based systems could make these sophisticated tools more accessible for educational purposes, fostering innovation and interdisciplinary research. Meanwhile, addressing the challenges and limitations faced in this research, such as the complexities in spectral interpretation and limitations in sample preparation, will be crucial for improving current methodologies and expanding their applicability.

Furthermore, exploring the application of the DONA system in environmental monitoring and in vivo studies could provide new perspectives on how proteins interact within their natural context. Such explorations could lead to discoveries that are not possible under controlled laboratory conditions.

In conclusion, the groundwork laid by this thesis suggests a vast potential for DNA origami-based systems in molecular biology. Continued exploration and development in this field are poised to yield further groundbreaking discoveries and technological advancements, significantly contributing to our understanding of molecular structures and interactions.

6. References

1.	R.P. Feynman, "There's Plenty of Room at the Bottom," Engineering and Science (Caltech, 1960), www.zyvex.com/nanotech/feynman.html.

2.	N., T. On the Basic Concept of 'Nano-Technology'. *Proc. Intl. Conf. Prod. Eng. Tokyo, Part II, 1974* (1974).

3.	Whitesides, G. M. & Grzybowski, B. Self-Assembly at All Scales. *Science (80-.).* **295**, 2418–2421 (2002).

4.	Xia, Y. & Whitesides, G. M. SOFT LITHOGRAPHY. *https://doi.org/10.1146/annurev.matsci.28.1.153* **28**, 153–184 (2003).

5.	Bhushan, B. Introduction to Nanotechnology. *Springer Handb. Nanotechnol.* 1–13 (2010). doi:10.1007/978-3-642-02525-9_1

6.	Neuman, K. C. & Nagy, A. Single-molecule force spectroscopy: optical tweezers, magnetic tweezers and atomic force microscopy. *Nat. Methods 2008 56* **5**, 491–505 (2008).

7.	Moerner, W. E. & Orrit, M. Illuminating Single Molecules in Condensed Matter. *Science (80-.).* **283**, 1670–1676 (1999).

8.	Glembockyte, V., Grabenhorst, L., Trofymchuk, K. & Tinnefeld, P. DNA Origami Nanoantennas for Fluorescence Enhancement. *Acc. Chem. Res.* **54**, 3338–3348 (2021).

9.	Zlatanova, J. & van Holde, K. Single-Molecule Biology: What Is It and How Does It Work? *Mol. Cell* **24**, 317–329 (2006).

10.	Pinheiro, A. V., Han, D., Shih, W. M. & Yan, H. Challenges and opportunities for structural DNA nanotechnology. *Nat. Nanotechnol.* **6**, 763–772 (2011).

11.	Rothemund, P. W. K. Folding DNA to create nanoscale shapes and patterns. *Nat. 2006 4407082* **440**, 297–302 (2006).

12.	Dey, S. *et al.* DNA origami. *Nat. Rev. Methods Prim. 2021 11* **1**, 1–24 (2021).

13.	Linko, V. At the Dawn of Applied DNA Nanotechnology. *Molecules* **25**, 639 (2020).

14.	Wang, S. *et al.* DNA Origami-Enabled Biosensors. *Sensors (Basel).* **20**, 1–18 (2020).

15.	Kühler, P. *et al.* Plasmonic DNA-origami nanoantennas for surface-enhanced Raman spectroscopy. *Nano Lett.* **14**, 2914–2919 (2014).

16.	Prinz, J., Heck, C., Ellerik, L., Merk, V. & Bald, I. DNA origami based Au–Ag-core–shell nanoparticle dimers with single-molecule SERS sensitivity. *Nanoscale* **8**, 5612–5620 (2016).

17.	Tapio, K. *et al.* A Versatile DNA Origami-Based Plasmonic Nanoantenna for Label-Free Single-Molecule Surface-Enhanced Raman Spectroscopy. *ACS Nano* **15**, 7065–7077 (2021).

18.	Delfino, I., Bizzarri, A. R. & Cannistraro, S. Single-molecule detection of yeast cytochrome c by Surface-Enhanced Raman Spectroscopy. *Biophys. Chem.* **113**, 41–51 (2005).

19.	Kneipp, K. *et al.* Single Molecule Detection Using Surface-Enhanced Raman Scattering (SERS).

Phys. Rev. Lett. **78**, 1667 (1997).

20. Moskovits, M. Surface-enhanced Raman spectroscopy: a brief retrospective. *J. Raman Spectrosc.* **36**, 485–496 (2005).

21. Heck, C. *et al.* Gold Nanolenses Self-Assembled by DNA Origami. *ACS Photonics* **4**, 1123–1130 (2017).

22. Zrimsek, A. B. *et al.* Single-Molecule Chemistry with Surface- and Tip-Enhanced Raman Spectroscopy. *Chem. Rev.* **117**, 7583–7613 (2017).

23. Tanwar, S., Haldar, K. K. & Sen, T. DNA Origami Directed Au Nanostar Dimers for Single-Molecule Surface-Enhanced Raman Scattering. *J. Am. Chem. Soc.* **139**, 17639–17648 (2017).

24. Niemeyer, C. M. Semisynthetic DNA–Protein Conjugates for Biosensing and Nanofabrication. *Angew. Chemie Int. Ed.* **49**, 1200–1216 (2010).

25. Zhan, P. *et al.* Recent Advances in DNA Origami-Engineered Nanomaterials and Applications. *Chem. Rev.* **123**, 3976–4050 (2023).

26. Schreiber, R. *et al.* Chiral plasmonic DNA nanostructures with switchable circular dichroism. *Nat. Commun.* **4**, (2013).

27. Kanehira, Y. *et al.* The Effect of Nanoparticle Composition on the Surface-Enhanced Raman Scattering Performance of Plasmonic DNA Origami Nanoantennas. *ACS Nano* **17**, 21227–21239 (2023).

28. Watson, J. D. & Crick, F. H. C. Molecular Structure of Nucleic Acids: A Structure for Deoxyribose Nucleic Acid. *Nat. 1953 1714356* **171**, 737–738 (1953).

29. Franklin, R. E. & Gosling, R. G. The structure of sodium thymonucleate fibres. I. The influence of water content. *Acta Crystallogr.* **6**, 673–677 (1953).

30. Seeman, N. C. Nucleic acid junctions and lattices. *J. Theor. Biol.* **99**, 237–247 (1982).

31. Seeman, N. C. Nanomaterials Based on DNA. *Annu. Rev. Biochem.* **79**, 65–87 (2010).

32. DNA structure - Labster. Available at: https://theory.labster.com/dna-structure/. (Accessed: 6th May 2024)

33. Deoxyribonucleic Acid (DNA). Available at: https://www.genome.gov/genetics-glossary/Deoxyribonucleic-Acid#:~:text=Definition,known as a double helix. (Accessed: 7th December 2023)

34. Bustin, S. Molecular Biology of the Cell, Sixth Edition; ISBN: 9780815344643; and Molecular Biology of the Cell, Sixth Edition, The Problems Book; ISBN 9780815344537. *Int. J. Mol. Sci.* **16**, 28123 (2015).

35. Berg, J. M., Tymoczko, J. L., Stryer, L. & Gatto, G. J. Biochemestry. 1224 (2011).

36. Bates, A. D. & Maxwell, A. DNA topology. 198 (2005).

37. Rich, A. & Zhang, S. Z-DNA: the long road to biological function. *Nat. Rev. Genet. 2003 47* **4**, 566–572 (2003).

38. Seeman, N. C. DNA in a material world. *Nature* **421**, 427–431 (2003).

39. Tsu-Ju, F. & Seeman, N. C. DNA Double-Crossover Molecules. *Biochemistry* **32**, 3211–3220 (1993).

40. Kogikoski, S., Ameixa, J. O., Mostafa, A. & Bald, I. Lab-on-a-DNA origami: nanoengineered single-molecule platforms. *4726 | Chem. Commun* **59**, 4726 (2023).

41. Douglas, S. M. *et al.* Rapid prototyping of 3D DNA-origami shapes with caDNAno. *Nucleic Acids Res.* **37**, 5001–5006 (2009).

42. Castro, C. E. *et al.* A primer to scaffolded DNA origami. *Nat. Methods* **8**, 221–229 (2011).

43. Šulc, P. *et al.* Sequence-dependent thermodynamics of a coarse-grained DNA model. *J. Chem. Phys.* **137**, (2012).

44. Kim, D. N., Kilchherr, F., Dietz, H. & Bathe, M. Quantitative prediction of 3D solution shape and flexibility of nucleic acid nanostructures. *Nucleic Acids Res.* **40**, 2862 (2012).

45. Funke, J. J. & Dietz, H. Placing molecules with Bohr radius resolution using DNA origami. *Nat. Nanotechnol. 2015 111* **11**, 47–52 (2015).

46. Wang, W. *et al.* Complex wireframe DNA nanostructures from simple building blocks. *Nat. Commun. 2019 101* **10**, 1–8 (2019).

47. Zhang, Q. *et al.* DNA origami as an in vivo drug delivery vehicle for cancer therapy. *ACS Nano* **8**, 6633–6643 (2014).

48. Steinhauer, C., Jungmann, R., Sobey, T. L., Simmel, F. C. & Tinnefeld, P. DNA origami as a nanoscopic ruler for super-resolution microscopy. *Angew. Chem. Int. Ed. Engl.* **48**, 8870–8873 (2009).

49. Choi, Y., Kotthoff, L., Olejko, L., Resch-Genger, U. & Bald, I. DNA Origami-Based Förster Resonance Energy-Transfer Nanoarrays and Their Application as Ratiometric Sensors. *ACS Appl. Mater. Interfaces* **10**, 23295–23302 (2018).

50. Dutta, A. *et al.* Molecular states and spin crossover of hemin studied by DNA origami enabled single-molecule surface-enhanced Raman scattering. *Nanoscale* **14**, 16467–16478 (2022).

51. Wang, C., Ebel, K., Heinze, K., Resch-Genger, U. & Bald, I. Quantum Yield of DNA Strand Breaks under Photoexcitation of a Molecular Ruby. *Chem. – A Eur. J.* **29**, e202203719 (2023).

52. Ebel, K. & Bald, I. Low-Energy (5-20 eV) Electron-Induced Single and Double Strand Breaks in Well-Defined DNA Sequences. *J. Phys. Chem. Lett.* **13**, 4871–4876 (2022).

53. Long, D. A. (Derek A. The Raman effect : a unified treatment of the theory of Raman scattering by molecules. 597 (2002).

54. Ferraro, J. R., Nakamoto, K. & Brown, C. W. Introductory Raman Spectroscopy: Second Edition. *Introd. Raman Spectrosc. Second Ed.* 1–434 (2003). doi:10.1016/B978-0-12-254105-6.X5000-8

55. Hecht, E. Optics / Eugene Hecht. *Optics* 338–387 (2017).

56. Kreibig, U. & Vollmer, M. Optical Properties of Metal Clusters. **25**, (1995).

57. Bohren, C. F. & Huffman, D. R. Absorption and Scattering of Light by Small Particles. *Absorpt.*

Scatt. Light by Small Part. (1998). doi:10.1002/9783527618156

58. Novotny, L. & Hecht, B. Principles of nano-optics. *Princ. Nano-Optics* **9781107005464**, 1–564 (2009).

59. Maier, S. A. Plasmonics: Fundamentals and applications. *Plasmon. Fundam. Appl.* 1–223 (2007). doi:10.1007/0-387-37825-1/COVER

60. Kelly, K. L., Coronado, E., Zhao, L. L. & Schatz, G. C. The optical properties of metal nanoparticles: The influence of size, shape, and dielectric environment. *J. Phys. Chem. B* **107**, 668–677 (2003).

61. Surface-Enhanced Raman Scattering. **103**, (2006).

62. Le Ru, E. C. & Etchegoin, P. G. Principles of Surface-Enhanced Raman Spectroscopy. *Princ. Surface-Enhanced Raman Spectrosc.* (2009). doi:10.1016/B978-0-444-52779-0.X0001-3

63. Moskovits, M. Surface-enhanced spectroscopy. *Rev. Mod. Phys.* **57**, 783 (1985).

64. Smith, E. & Dent, G. Modern raman spectroscopy: A practical approach. *Mod. Raman Spectrosc. A Pract. Approach* 1–241 (2019). doi:10.1002/0470011831

65. Schlücker, S. Surface enhanced Raman spectroscopy : analytical, biophysical and life science applications. 331 (2011).

66. Liu, N. & Liedl, T. DNA-Assembled Advanced Plasmonic Architectures. *Chem. Rev.* **118**, 3032–3053 (2018).

67. Acuna, G. P. *et al.* Fluorescence enhancement at docking sites of DNA-directed self-assembled nanoantennas. *Science* **338**, 506–510 (2012).

68. Mirkin, C. A., Letsinger, R. L., Mucic, R. C. & Storhoff, J. J. A DNA-based method for rationally assembling nanoparticles into macroscopic materials. *Nat. 1996 3826592* **382**, 607–609 (1996).

69. Yan, H., Park, S. H., Finkelstein, G., Reif, J. H. & LaBean, T. H. DNA-templated self-assembly of protein arrays and highly conductive nanowires. *Science* **301**, 1882–1884 (2003).

70. Heck, C., Kanehira, Y., Kneipp, J. & Bald, I. Platzierung einzelner Proteine in den SERS-Hot-Spots selbstorganisierter Silbernanolinsen. *Angew. Chemie* **130**, 7566–7569 (2018).

71. Endo, M. & Sugiyama, H. Chemical Approaches to DNA Nanotechnology. *ChemBioChem* **10**, 2420–2443 (2009).

72. Somorjai, G. A. & Park, J. Y. Evolution of the Surface Science of Catalysis From Single Crystals to Metal Nanoparticles Under Pressure. (2008). doi:10.1063/1.2888970

73. Mahapatra, G. *et al.* Phosphorylation of Cytochrome C Threonine 28 Regulates Electron Transport Chain Activity in Kidney. (2017). doi:10.1074/jbc.m116.744664

74. Wilson, D. F. Oxidative Phosphorylation: Unique Regulatory Mechanism and Role in Metabolic Homeostasis. (2017). doi:10.1152/japplphysiol.00715.2016

75. Fetrow, J. S., Cardillo, T. S. & Sherman, F. Deletions and Replacements of Omega Loops in Yeast Iso-1-Cytochromec. (1989). doi:10.1002/prot.340060404

76. Pace, N. R., Walker, T. A., Pace, B. & Erikson, R. L. The Nucleotide Sequence of Chicken 5S

Ribosomal RNA. (1974). doi:10.1007/bf01796560

77. Guerra-Castellano, A. *et al.* Post-Translational Modifications of Cytochrome C in Cell Life and Disease. (2020). doi:10.3390/ijms21228483

78. Ow, Y. L. P., Green, D. R., Hao, Z. & Mak, T. W. Cytochrome c: functions beyond respiration. *Nat. Rev. Mol. Cell Biol. 2008 97* **9**, 532–542 (2008).

79. Kharbanda, S. *et al.* Role for BCL-X$_L$as an Inhibitor of Cytosolic Cytochrome C Accumulation in DNA Damage-Induced apoptosis. *Proc. Natl. Acad. Sci.* (1997). doi:10.1073/pnas.94.13.6939

80. Martínez-Fábregas, J. *et al.* New Arabidopsis Thaliana Cytochrome C Partners: A Look Into the Elusive Role of Cytochrome C in Programmed Cell Death in Plants. *Mol. Cell. Proteomics* (2013). doi:10.1074/mcp.m113.030692

81. Babbitt, S. E., Sutherland, M. C., Francisco, B. S., Mendez, D. L. & Kranz, R. G. Mitochondrial Cytochrome C Biogenesis: No Longer an Enigma. *Trends Biochem. Sci.* (2015). doi:10.1016/j.tibs.2015.05.006

82. Ma, J.-G. *et al.* The Structural Origin of Nonplanar Heme Distortions in Tetraheme Ferricytochromes *c*$_3$. *Biochemistry* (1998). doi:10.1021/bi981189i

83. Oellerich, S., Wackerbarth, H. & Hildebrandt, P. Spectroscopic Characterization of Nonnative Conformational States of Cytochrome *c*. (2002). doi:10.1021/jp013841g

84. Brazhe, N. A. *et al.* SERS uncovers the link between conformation of cytochrome c heme and mitochondrial membrane potential. *bioRxiv* 2021.01.03.425119 (2022). doi:10.1101/2021.01.03.425119

85. Ong, Y. H., Lim, M. & Liu, Q. Comparison of Principal Component Analysis and Biochemical Component Analysis in Raman Spectroscopy for the Discrimination of Apoptosis and Necrosis in K562 Leukemia Cells. (2012). doi:10.1364/oe.20.022158

86. Tapio, K. *et al.* A Versatile DNA Origami-Based Plasmonic Nanoantenna for Label-Free Single-Molecule Surface-Enhanced Raman Spectroscopy. *ACS Nano* **15**, 7065–7077 (2021).

87. Okada, M. *et al.* Label-Free Raman Observation of Cytochrome C Dynamics During Apoptosis. *Proc. Natl. Acad. Sci.* (2011). doi:10.1073/pnas.1107524108

88. Rocha-Mendoza, I. *et al.* Sum Frequency Vibrational Spectroscopy: The Molecular Origins of the Optical Second-Order Nonlinearity of Collagen. (2007). doi:10.1529/biophysj.107.111047

89. Kuku, G., Altunbek, M. & Culha, M. Surface-Enhanced Raman Scattering for Label-Free Living Single Cell Analysis. *Anal. Chem.* **89**, 11160–11166 (2017).

90. Smith, R., Wright, K. L. & Ashton, L. Raman Spectroscopy: An Evolving Technique for Live Cell Studies. (2016). doi:10.1039/c6an00152a

91. Dorninger, F., Werner, E. R., Berger, J. & Watschinger, K. Regulation of Plasmalogen Metabolism and Traffic in Mammals: The Fog Begins to Lift. (2022). doi:10.3389/fcell.2022.946393

92. Castell, O. K., Dijkman, P. M., Wiseman, D. N. & Goddard, A. D. Single Molecule Fluorescence for Membrane Proteins. (2018). doi:10.1016/j.ymeth.2018.05.024

93.   Garcia-Parajo, M. F., Segers-Nolten, G. M. J., Veerman, J.-A., Greve, J. & van Hulst, N. F. Real-Time Light-Driven Dynamics of the Fluorescence Emission in Single Green Fluorescent Protein Molecules. (2000). doi:10.1073/pnas.97.13.7237

94.   Delfino, I., Bizzarri, A. R. & Cannistraro, S. Time-dependent study of single-molecule SERS signal from yeast cytochrome c. *Chem. Phys.* **326**, 356–362 (2006).

95.   Zhou, J. *et al.* Single Molecule Protein Segments Sequencing by a Plasmonic Nanopore. *Nano Lett.* **23**, 44 (2023).

96.   Treffer, R. *et al.* Advances in TERS (Tip-Enhanced Raman Scattering) for Biochemical Applications. (2012). doi:10.1042/bst20120033

97.   Mostafa, A., Kanehira, Y., Dutta, A., Kogikoski, S. & Bald, I. Single-Molecule Surface-Enhanced Raman Scattering Measurements Enabled by Plasmonic DNA Origami Nanoantennas. *JoVE (Journal Vis. Exp.* **2023**, e65310 (2023).

98.   Liu, B. & Liu, J. Freezing-Driven DNA Adsorption on Gold Nanoparticles: Tolerating Extremely Low Salt Concentration but Requiring High DNA Concentration. *Langmuir* **35**, 6476–6482 (2019).

99.   Shen, J., Li, Y., Gu, H., Xia, F. & Zuo, X. Recent development of sandwich assay based on the nanobiotechnologies for proteins, nucleic acids, small molecules, and ions. *Chem. Rev.* **114**, 7631–7677 (2014).

100. Benson, E. *et al.* DNA rendering of polyhedral meshes at the nanoscale. *Nat. 2015 5237561* **523**, 441–444 (2015).

101. Veneziano, R. *et al.* Designer nanoscale DNA assemblies programmed from the top down. *Science (80-.).* **352**, (2016).

102. Tikhomirov, G., Petersen, P. & Qian, L. Fractal assembly of micrometre-scale DNA origami arrays with arbitrary patterns. *Nature* **552**, 67–71 (2017).

103. He, Z., Shi, K., Li, J. & Chao, J. Self-assembly of DNA origami for nanofabrication, biosensing, drug delivery, and computational storage. *iScience* **26**, 106638 (2023).

104. Winfree, E., Liu, F., Wenzler, L. A. & Seeman, N. C. Design and self-assembly of two-dimensional DNA crystals. *Nature* **394**, 539–544 (1998).

105. Dietz, H., Douglas, S. M. & Shih, W. M. Folding DNA into twisted and curved nanoscale shapes. *Science* **325**, 725–730 (2009).

106. Chandrasekaran, A. R., Pushpanathan, M. & Halvorsen, K. Evolution of DNA origami scaffolds. *Mater. Lett.* **170**, 221–224 (2016).

107. Linko, V. & Dietz, H. The enabled state of DNA nanotechnology. *Curr. Opin. Biotechnol.* **24**, 555–561 (2013).

108. Marchi, A. N., Saaem, I., Vogen, B. N., Brown, S. & Labean, T. H. Toward larger DNA origami. *Nano Lett.* **14**, 5740–5747 (2014).

109. Zhao, Z., Liu, Y. & Yan, H. Organizing DNA origami tiles into larger structures using preformed scaffold frames. *Nano Lett.* **11**, 2997–3002 (2011).

110. Ke, Y., Ong, L. L., Shih, W. M. & Yin, P. Three-dimensional structures self-assembled from DNA

bricks. *Science (80-.).* **338**, 1177–1183 (2012).

111. Douglas, S. M., Bachelet, I. & Church, G. M. A logic-gated nanorobot for targeted transport of molecular payloads. *Science* **335**, 831–834 (2012).

112. Fu, J., Liu, M., Liu, Y., Woodbury, N. W. & Yan, H. Interenzyme substrate diffusion for an enzyme cascade organized on spatially addressable DNA nanostructures. *J. Am. Chem. Soc.* **134**, 5516–5519 (2012).

113. Liedl, T., Högberg, B., Tytell, J., Ingber, D. E. & Shih, W. M. Self-assembly of three-dimensional prestressed tensegrity structures from DNA. *Nat. Nanotechnol. 2010 57* **5**, 520–524 (2010).

114. Perrault, S. D. & Shih, W. M. Virus-inspired membrane encapsulation of DNA nanostructures to achieve in vivo stability. *ACS Nano* **8**, 5132–5140 (2014).

115. Rajendran, A., Endo, M. & Sugiyama, H. Single-Molecule Analysis Using DNA Origami. *Angew. Chemie Int. Ed.* **51**, 874–890 (2012).

116. Kuzyk, A. *et al.* DNA-based self-assembly of chiral plasmonic nanostructures with tailored optical response. *Nature* **483**, 311–314 (2012).

117. Tapio, K. *et al.* A Versatile DNA Origami-Based Plasmonic Nanoantenna for Label-Free Single-Molecule Surface-Enhanced Raman Spectroscopy. *ACS Nano* **15**, 7065–7077 (2021).

118. Hu, S., Spiro, T. G., Morris, I. K., Singh, J. P. & Smith, K. M. Complete Assignment of Cytochrome c Resonance Raman Spectra via Enzymatic Reconstitution with Isotopically Labeled Hemes. *J. Am. Chem. Soc.* **115**, 12446–12458 (1993).

119. Jordan, T., Eads, J. C. & Spiro, T. G. Secondary and tertiary structure of the A-state of cytochrome c from resonance Raman spectroscopy. *Protein Sci.* **4**, 716–728 (1995).

120. Delfino, I., Bizzarri, A. R. & Cannistraro, S. Single-molecule detection of yeast cytochrome c by Surface-Enhanced Raman Spectroscopy. *Biophys. Chem.* **113**, 41–51 (2005).

121. Yeo, B. S., Mädler, S., Schmid, T., Zhang, W. & Zenobi, R. Tip-Enhanced Raman Spectroscopy Can See More: The Case of Cytochrome c. *J. Phys. Chem. C* **112**, 4867–4873 (2008).

122. Keating, C. D., Kovaleski, K. K. & Natan, M. J. Heightened electromagnetic fields between metal nanoparticles: Surface enhanced raman scattering from metal - Cytochrome c-metal sandwiches. *J. Phys. Chem. B* **102**, 9414–9425 (1998).

123. Brazhe, N. A. *et al.* Probing cytochrome c in living mitochondria with surface-enhanced Raman spectroscopy. *Sci. Reports 2015 51* **5**, 1–13 (2015).

124. Spiro, T. G. & Strekas, T. C. Resonance Raman spectra of hemoglobin and cytochrome c: inverse polarization and vibronic scattering. *Proc. Natl. Acad. Sci. U. S. A.* **69**, 2622–2626 (1972).

125. Hu, S., Smith, K. M. & Spiro, T. G. Assignment of Protoheme Resonance Raman Spectrum by Heme Labeling in Myoglobin. *J. Am. Chem. Soc.* **118**, 12638–12646 (1996).

126. Spiro, T. G. Resonance Raman spectroscopy as a probe of heme protein structure and dynamics. *Adv. Protein Chem.* **37**, 111–159 (1985).

127. Asher, S. A. UV resonance Raman spectroscopy for analytical, physical, and biophysical chemistry. Part 2. *Anal. Chem.* **65**, (1993).

128. Haris, P. I. & Severcan, F. FTIR spectroscopic characterization of protein structure in aqueous and non-aqueous media. *J. Mol. Catal. B Enzym.* **7**, 207–221 (1999).

129. Zhou, J. *et al.* Single Molecule Protein Segments Sequencing by a Plasmonic Nanopore. *Nano Lett.* **23**, 2800–2807 (2023).

130. Nie, S. & Emory, S. R. Probing Single Molecules and Single Nanoparticles by Surface-Enhanced Raman Scattering. *Science* **275**, 1102–1106 (1997).

131. Haynes, C. L. & Van Duyne, R. P. Nanosphere lithography: A versatile nanofabrication tool for studies of size-dependent nanoparticle optics. *J. Phys. Chem. B* **105**, 5599–5611 (2001).

132. Li, J. F. *et al.* Shell-isolated nanoparticle-enhanced Raman spectroscopy. *Nat. 2010 4647287* **464**, 392–395 (2010).

133. Berghian-Grosan, C. & Magdas, D. A. Application of Raman spectroscopy and Machine Learning algorithms for fruit distillates discrimination. *Sci. Rep.* **10**, (2020).

134. Qian, X. M. & Nie, S. M. Single-molecule and single-nanoparticle SERS: from fundamental mechanisms to biomedical applications. *Chem. Soc. Rev.* **37**, 912–920 (2008).

135. Bizzarri, A. R. & Cannistraro, S. Surface-enhanced Raman spectroscopy combined with atomic force microscopy for ultrasensitive detection of thrombin. *Anal. Biochem.* **393**, 149–154 (2009).

136. Stiles, P. L., Dieringer, J. A., Shah, N. C. & Van Duyne, R. P. Surface-Enhanced Raman Spectroscopy. *https://doi.org/10.1146/annurev.anchem.1.031207.112814* **1**, 601–626 (2008).

137. Rygula, A. *et al.* Raman spectroscopy of proteins: a review. *J. Raman Spectrosc.* **44**, 1061–1076 (2013).

138. Mikhonin, A. V., Myshakina, N. S., Bykov, S. V. & Asher, S. A. UV resonance Raman determination of polyproline II, extended 2.5 1-helix, and β-sheet ψ angle energy landscape in poly-L-lysine and poly-L-glutamic acid. *J. Am. Chem. Soc.* **127**, 7712–7720 (2005).

139. Asher, S. A. UV Resonance Raman Studies of Molecular Structure and Dynamics: Applications in Physical and Biophysical Chemistry. *https://doi.org/10.1146/annurev.pc.39.100188.002541* **39**, 537–588 (2003).

140. Wu, Q., Balakrishnan, G., Pevsner, A. & Spiro, T. G. Histidine Photodegradation during UV Resonance Raman Spectroscopy†. *J. Phys. Chem. A* **107**, 8047–8051 (2003).

141. Carey, P. R. *Biochemical applications of Raman and resonance Raman spectroscopies*. (Academic Press, 1982).

142. Spiro, T. G. & Gaber, B. P. Laser Raman Scattering as a Probe of Protein Structure. *https://doi.org/10.1146/annurev.bi.46.070177.003005* **46**, 553–572 (2003).

143. Jakubek, R. S., Handen, J., White, S. E., Asher, S. A. & Lednev, I. K. Ultraviolet resonance Raman spectroscopic markers for protein structure and dynamics. *TrAC Trends Anal. Chem.* **103**, 223–229 (2018).

144. Asamoto, D. A. K. & Kim, J. E. UV Resonance Raman Spectroscopy as a Tool to Probe Membrane Protein Structure and Dynamics. *Methods Mol. Biol.* **2003**, 327–349 (2019).

145. Yager, P., Domingo, G. J. & Gerdes, J. Point-of-care diagnostics for global health. *Annu. Rev.*

Biomed. Eng. **10**, 107–144 (2008).

146. Pai, N. P., Vadnais, C., Denkinger, C., Engel, N. & Pai, M. Point-of-Care Testing for Infectious Diseases: Diversity, Complexity, and Barriers in Low- And Middle-Income Countries. *PLOS Med.* **9**, e1001306 (2012).

147. Peeling, R. W. & Mabey, D. Point-of-care tests for diagnosing infections in the developing world. *Clin. Microbiol. Infect.* **16**, 1062–1069 (2010).

148. Whitesides, G. M. The origins and the future of microfluidics. *Nat. 2006 4427101* **442**, 368–373 (2006).

149. Yetisen, A. K., Akram, M. S. & Lowe, C. R. Paper-based microfluidic point-of-care diagnostic devices. *Lab Chip* **13**, 2210–2251 (2013).

150. Ozcan, A. Mobile phones democratize and cultivate next-generation imaging, diagnostics and measurement tools. *Lab Chip* **14**, 3187–3194 (2014).

151. Wang, S. Q. *et al.* Portable microfluidic chip for detection of Escherichia coli in produce and blood. *Int. J. Nanomedicine* **7**, 2591 (2012).

152. Laksanasopin, T. *et al.* A smartphone dongle for diagnosis of infectious diseases at the point of care. *Sci. Transl. Med.* **7**, 273re1 (2015).

7. Appendix

Table 8 List of fork staples.

Strand #	Sequence	Length
1	TTTGACCAGCGGATAATCAAAAGTTCAGGTAATAGTGCAAAACTCG	46
2	TATAAGTATAGCCGCCTGT	19
3	AAATTTTTATACCAAACCCACTACAGTGAGCGGAAGCAAACTCC	44
4	CACGACGAATTCGTTGTTATTTATTAATCGTATTACATTTTGACG	45
5	GTGCCACGTAGACCGTGTGA	20
6	CGGGACAGATTTACTTAGCCGCCGCTCTGAATTGCGAA	38
7	AGACGTTGAAAATCTCCAAAAAAATAAATCCAAACAGGGAGCACG	45
8	AGCCTAACTCCCGAAGAACGGGTATTAAAATGCAGTTCGAGCACCGTT	48
9	ATCAATAGGATTGTATAAGCAAAAGCCCCAAGAGGGGAAAACGAGA	46
10	AGCCCGAAAGACTTCCACGCCAAAGAACATCCAA	34
11	GTACAGAAGTAATCAACGACGATTAAGT	28
12	AGCGGAGTGAGAATATACATGTATTAGATATCATT	35
13	AGAGAGTACCTTTAATTGCTTTTTTTT	27
14	GTTAAACTTAGGTTGACTAGCATACTGC	28
15	CACCCTCAGAGCATGTACC	19
16	AGATGATGAATTATCACAGGGCGATTTGCTCAGT	34
17	TTTTTTTTTCCTTTTGATAATTTTGCGGGTCAATAACCTGTTAGATACTTAATTG	55
18	GAAATCGGCGGCTTATCAAGCCGTTTTTATTAAATTCTGTCC	42
19	TGACCATTTAGCTATGACCCTACGCAAGGATAA AACAACAACAACAACAACAAC	57
20	ATGGGATTTTGCTACGGGGTC	21
21	AAAAGATAGGCGAAAAAAGGTAAAGTCAGAAAGGCGG	37
22	ATAGCTAATCAGAGCATAATTTATACAA	28
23	CGTGAACCATCACCCAAATCAAGTCGCCAGGGTGGTTTTTCTTTTCAC	48
24	GTAATCGAAAGCCTAATTGAGAACACCC	28
25	TACATCATGGCTTAGAGCATTTCGCAATTTGATGTA	36
26	TGGTTTAATTATTTTAAGTATCGGGGCGCAT	31
27	ATCTACAAACGGAGACAGTCAAATACCGACAATCCTG	37
28	TATAACGATACGAGTGTGTCGCATAGGCTG	30
29	CCCAGCTGGGCTTTCCGGCACCGAAGATCGAATTACCCAGGTAGAA	46
30	AGGTGAATTTCTTAAGGCCGCTTTATAAGTAACCA AAC AAC AAC AAC AAC AAC AAC AAC	59
31	ATCACATCGCCATTAAAAACTGAGAGCCAGATGTA	36
32	GCTCATTCAGAACGCGGGCCTTGCCGGA	28
33	CTGAATAGTGGACTCCAACGGTCATTTTTGCGGTTTTTTTT	41

34	GAACAACATTTAGGTGGGAACTGGCCTTCCTGTAGTTTTTGTGACGAT	48
35	AGGGTTGCGGTGTCTGGAACGCCCAATAGAATAGCCAAGCGGTCAAATAT	50
36	AAAAGAACGTCCAATGTCAATATGAACG	28
37	TATCGGCCTTGCTGACGGTACAGCAGCGTACAGAG	35
38	TCCTTATTCAACAATGTAATTTATGCGTACTAGAATATCTTCTGAC	46
39	ATCACATCGCCATTAAAAACTGAGAGCCAGATGTA	35
40	GGCTTAATTGACAGAGAGCTACAACCACCCTCAT	34
41	AAATGCTGATAATCATAAGCTTAGCGCTATTATAA	35
42	CCATTACTACCAGTATGTTTGAGGGGACCAAAGCGAAGGGCGCGCCAG	48
43	AACAATATTATTAAAGGAATTCACAAACAAAAGGCTCC	38
44	AAAAGGAGCCTTTAGCATCGGGATTTTAGCGTACT	35
45	TTTAAACAATCAGGGGGGTAGCCAATATG	28
46	TGCCTTGAGTAATTTCTGT	19
47	ATGTAAATATATTTCCCTTTTAATAGCA	28
48	AGACGACGAGAACAAGCCGGTATTCTAAGAAGTGGTGGTTCC	42
49	CAGAGCCTCAATCACAATTCATCAATTGGTAACATCTTTACATGAAATG	49
50	AGTTTGATTTCCTGCGAGGCGCAACTTTGAAAGAGATATTCATACCCAGT	50
51	AAAGGAAGCTGGCAAGAGTCTCTTCTTT	28
52	GTAACACCCAAACAGGAGCCTTTAGAATCGAAATAATATCCCATCCT	47
53	ATTGTCATTAATTTGGGATAGCAGCCTTTAGCGCGTTTGGAGCCA	45
54	TAACTTATTTGTTATACTTTATCAGACAAAGATGAGGATGCAGATT	46
55	AAA AAA AAA AAA AAA AAA AAA AAA AACGGGTGAATACATGGCGAG	45
56	TGGGTAAATCGGTGAGTAGTAAATTGTTAACGTAAGAAC	39
57	CGAGCTCGTTGTAATTGACAACAAAGCT	28
58	AAAAACGGGCCAAAACATTCAAAAAACGACTCATTACAGGCTTGAGA	47
59	CCATTCACAATTTCCAGGACGTTGGGTAAATCACCCGTCACCCGTTTT	48
60	AGTTAATGCCCCGTTAGTA	19
61	AGGATTAGCGGGATAGTTA	19
62	GGCAAAAAAATACTCGGTCGGCGCCGACAAT GACAACAACCATCGCTTTTTTTT	55
63	CATTAAAAACCTCCAAGACTCAATACCC	28
64	TGAACAAATAAGAAAGGCATTAACGCGCCTGTTTACATTCCACTTGCGG	49
65	AATCCCTTCTGACCTGAAAGAAAGGAA	27
66	AGTAGTACGGTTTCATTCCATATAACAGTCAATTCGCCTCAGGCAATGC	49
67	AAACAAGCCGGAGATCTTTACCCTGATCTCCCCCTTGGATAGCTCAAAAT	50
68	AAAAAAAAAAAAAAAAAAAAAAAAAAACAGGTAAAACCGAACATTATATTTTC	52
69	GGTTTTGATTTTCAGGCGCAACCCGGAAAAGTAGCA	36
70	CCACCGAGGGAACCGTAGCCCCAACAGAAGTCAGAT	36
71	TTTTAGTAAGAGTTGAGATTATTATTATGCGTCAA	35
72	GGAAGGTTAAAATGGAAGGG	20

73	ACCGTACTCAGGAGTACAA	19
74	CCTCGTGCCCGAACGCCGCTCACTCCATGGAACGGT	36
75	TGGCTTCGCTCAAGGCGGCCAGTGGGATCCCACACAACTGCTTT	44
76	CGGTCAAACTGACCAGACGGGCCACCAAAGCGTCAGAAAGGAACA	45
77	ATCTCAAGAATATTCATCTGATTGCAG	27
78	TACATCACCAACCTAAAAAAGCGAAAGTTTGATGTA	36
79	TACATCTCTTTAGGAGTCAGAAGGAGCGGAGATGTA	36
80	AGCCCTCGTCATTCAAACCAGCGAAATCGTATTA	34
81	TAAATCATTTCATCAATCAGATATAGAAAAAATCCCCCCAGCTAAGAGGA	50
82	ACCCCGAACGAACCACCAGCCGCCTGC	27
83	GAGGTTTGAGCGTCTTTGTTTTTAACTGCGCTAATTCGTCATAAATAT	48
84	CCTGTAAGAATACGTGGCACAGTTGGC	27
85	CGCGTTTTAATTCTGAGAGACAATAAATACTAAT	34
86	CACCACGCGCAGTAGAGACTATAACTAT	28
87	ATTTCAAAGGTTATACCTTTTTTGTCCTTGAAAA	34
88	GGTTTATCAGCTTCACCCTCGCCAGAACTTAATG	34
89	CCACACCATTGCGTCCCAGCGATTATACGGACTAAGGATCGTGCTTTCG	49
90	TTTTTTAACCGTTGTAGCAATAGTCCATCGATATATGTAATGCCACTACGAAGGCTTTTT	60
91	CCAGAAGATAAACAGAGGTGAGGCGG	27
92	TATCTATTAGTCTTTAATGTGCTGAAC	27
93	CAATCAAACAAGAACCATATTCCAGTATATAAACATGGTTTGTTTC	46
94	AACAGGAGGGAGCTTCATTAAGGCAGGT	28
95	ATATTCACAGTAATTTATCCCGTTACAAAATAAACACGCGAGACCGCAC	49
96	CAGACGAGATAAATCCGGAAGAGGTCGA	28
97	TTGGAACTTTAAATCCAATTC	21
98	ATCAAAAGCAAGCAGTAGGAATCATTACGCATTAATTAGCAAGGTAAAG	49
99	AGCGAGAGGCTTTTAAAATGTTGATAACTGGAGC	34
100	TCAATAGATATACTGGTAATAA	22
101	CATCGGACCCAAATCAGCAAGGTGTTGGGCCATTCG	36
102	ATTCTTATAACAACAAAATGATTACCAACGCTAACTGAAGCCCTGTCTT	49
103	GATTATTTACATTGTTAGAAGGCTTTTGCCACCCT	35
104	TGATAAGAAAGGAAACCAAACGTAAAGAAACATGGTTTCCG	41
105	ATTCAAAAGGGTGAGGCAAGGTGGTTTGCTTATAA	35
106	GATTAGTAATAACAGGCCACCTTGCAGGTCCATTA	35
107	CGTAACCTTCTCCGAATACCAGGAATTA	28
108	CTTGAAACACCAGTGAACATCAAGCCAGGCGAAATCCGAGGTTGAAGCC	49
109	AGAAGCAAATATTATAAGAGAACAACATGTTCAGCTACCAAGTGCGTTTT	50
110	GGGAGAAAACGTCAGCCAACATAGATAAGTCCTGATAATCGGTTAAATC	49
111	TGATACCGATAGTTCTGAGGCGAGTAAAAGTGTAGAACAACAACAACAACAACAACAAC	59

112	GTTTATATACATAACCATGATTGGATTCG	29
113	GGAACCCCATTTTATCGTTGCTATAGAAAC	30
114	GAATATACTTTGAACCATCGAATTAGAG	28
115	TTTTTTTTAGAAGCCTTTATTTCAGTAATACGAGTCAAAGGGCGACAGGATT	52
116	AATAGTGAATCATACATCAAAGTTGGAATAGGTG	34
117	CTCTAGACCAAGCTTGACCTTTAAGGCTTG	30
118	AATGAATCACACCCTCTCAGAGCTTCCTGATCTG	34
119	GAGGCTGAGACTGATCTAA	19
120	GGCGAATAACAAAAAAATTATAGGGAGGGAAGGTAAATAGAATTTCCC	48
121	ACCTGGCCAACAGAGATAGATCTAAAATAGATGTA	35
122	TACATCAAAGAACGCGAGAGATAGCAATAAGAGTTTAGTACCGCGATGTA	50
123	ACGTTAAACCCCGGTTTAGACCAAATGC	28
124	TACATCGCAGCAAATGAACAATCGCAAGACGATGTA	36
125	CATAGCGATGGTCTGATGTTAGCGAGGAAACGCAATAACCGAAGTAGTTA	50
126	GCTGCATGCAGGGGGATGTGCTGATTACGCCTGACGATAATCATTG	46
127	CTGAGTAATGTGTAAATTAAGGTTGCAGCCGAGAT	35
128	CGCCGCTTGAGTGAGAAACAAAGTACAACAACGGCAAAGACAATTGTATC	50
129	AAA AAA AAA AAA AAA AAA AAA AAA TTTTTGGGGTCGAGGTGCCGTAGAGGCGGTTTGCGTATTGGG AAC AAC AAC AAC AAC AAC AAC AAC	42
130	GGAAATACCTAAATCCTGCGCAGTCCAGCAT	31
131	TGCCTAAACAGGGCGACAGGAGTAATATCCAG	32
132	CGTCACCAGGCAAGAAAATTGAGAATAAGAAAAG	34
133	AACCAGGGACGACAGAACTGGACTAACG	28
134	TACATCACCTATTATTCTGATCGTCTT	27
135	TAATAGAGACCAGTAATAAAAGGGACATCACTAACA	36
136	AGAACCGCGTGCCCGTATA	19
137	ACAGTACAATTAATAATTCATGCAAAGA	28
138	CTAAATTTAACCGGAATAGATAACATTAGAC	31
139	TTGATACGAGGGTAGCGGAGATCCTGGGG	29
140	CTGCCATTGAATTACAGCGAGTAGTTTGTCACAATCAAAAGAAAAAT	47
141	TTGCTTCTGTCCAAAGAGTGGCAAGTCGAGAGGG	34
142	ACTAAAGGAATTTACCGCGACAACTTTTAAA	31
143	GCCATAAAGCTTTGACAGGCCGACCGCCAGCCATTGC	37
144	AAGATTACTGAATCAAATAGCGAAGCGCCCACAAGACAA	39
145	GGAATCTTATAACGGCTTATTAGAATAA	28
146	AGTTTTGAAAGTTTGCACCGTAAGATTCGCTTCA	34
147	GTTACACTGTTTAACATAAAGAGCATAATCCTGATT	36
148	ATTTGGGGAGTAGAGTAGCTCAACATGTAAGAGTCCACTAT	41
149	AACCTACCATTTCATAAAGAATCACATGAAAGTA	34

150	TACGAGCATGTTTTGCAC	18
151	AATATCAAGGGTGAGTGAAT	20
152	AGCCGTAATCCATCAAAAATAATTTTTAACCATAACCGAAGTTTTG	46
153	TTAGAATGCTTTTTTCATTTAAGGAAATCGCGCAGA	36
154	CCTGAGTAGAAGAAAGTGTTTTTTGCGAGACTTT	35
155	GTTTGGACACGTAACTTATTAGTCAGACTGTAGCGAATGAAATACCAA	48
156	TCATCGACAATAAATATAAAGTCACCATTATTTTTTGAGAGTTCAG	46
157	CATCACCTCGCGCTGAGAAG	20
158	TCATATATTTTAAATAGCATAATCACCGCTTCCAGT	36
159	GCGTAACCCTGAGCCAAGGTGAAACAAACAAATA	34
160	CTACGTTAATCTAATGCAACAACCTCATCAA	31
161	AAAGCACTAAATCGGAACCCTTGAATCGGCCAACGCGCGGGG	42
162	TGACAGGCGACCTGCAATTCCCGGGTAC	28
163	CGAGGCAACCAGACTAAATCAATTGTAA	28
164	GGCGGATAAGTGCACAGAC	19
165	TAAAGTAAGTGTTGCTGGCCCGAGCTTCAAAGCGA	35
166	TGCGAACGCGCGAGTCGGTTGGAACCCAACAACAACAACAACAACAACAAC	51
167	TAAAGAACTAATGCTTTTAGTT	22
168	ATGGTTGTGTAAAGTTGTATCATCGCCTTTGGCC	34
169	TAAGGCGTTATTAAGCCAACATAAACCCTCAGAA	34
170	CGGTCACGACGGGGCTAAAACACTCATCGGAAGTTGAGTTAAAACAGCT	49
171	ACTACAACCACCAGAAAGTAAGCAAAACTTAAAT	34
172	GTTTTAAAACAACTTTCAAAGGAGTGATACATTAACC	37
173	AAA AAA AAA AAA AAA AAA AAA AAA AAAGGGAGCCCCCGATTTAGAGCTTAAACCTGTCGTGCCAGCTGCATTAA AAC AAC AAC AAC AAC AAC AAC AAC	50
174	TATTAACACAACGCTCAACA	20
175	CAACAGTTGCTTTACATCGG	20
176	CTCAATCGTCAACAATTTTCCAGTGAACCAC	31
177	ATTGACAATATTTTTGAATACCCTCAA	27
178	AACAATAACGTCAGTAGACCGACTTCAAGAGAAG	34
179	AGGGATAGCAAGCCCAATA	19
180	AGCATTCCCCATATAAGAAAATATTATCAAGCAA	34
181	AAAAAAAAAAAAAAAAAAAAAAAAAACCAGACTTGCCCTAGC TAAACTGAAAAGGTGGCATTGATTCATGCAAC	73
182	TTGCGGAATGATGGTAGAACCGCCTCCCAGAGCCAATGATACCAGTTTC	49
183	CCAGCAATTGACGGTTAATTAAATGGAA	28
184	TACATCCACCCTCAGAACCGTGAGTTT	27
185	CACCAGTCACACTTAGAGC	19
186	TTTTTTTTCCACGCATAACCACGCAAAGCGGGCGCTA GGGCGGGAAGACGAAAGA	55

| 187	AGCGAACTTTGCCAAATCCAAAGCTATTATAGTC	34
188	TGCACTCCATAGGTCACGTTGGTGGATTGAATTCATCAGCAACACT	46
189	TATCTGGTCAACCTGAGCAA	20
190	AAATATTTAAGCTCATTTCGCGTCAAACGGCGTAGATGCCTCAGGCTTC	49
191	GCTTTGACAAGCGCGCTAACTCACATTACGCCGCGTCCTGAGCTCAAAC	49
192	TCATTGAAAGAGGGTGTGATAAATTAATGAGAATCGCATATGTTATTTT	49
193	AAAAAAAAAAAAAAAAAAAAAAAAATTCATGATTTGACCTGCGCTC	45
194	TACATCATTATCATCATACGCCACCAATCACCGCCTATTTCGGAGATGTA	49
195	CATTAAACCAGCTTCGTCGGAGTGCAT	27
196	TCCAGACCTGGAACCACCATCTTATCAAAAAGTA	34
197	CTAGCTTTAGTATCATAGGCAGACGATTTTTTCCAG	36
198	TAATAATTTTTTCAATGGAAATTTAGAATCAGAGCAAAACGCTCAT	46
199	CACCAGAGCCGGAATGTGAAATAATCATGGTCATAAATTGCGTTCATTTT	50
200	AGACGAACTGATAGCCCTAAAAAATCT	27
201	AGTCGGGGCTGCGCTCAGTGATCACTTG	28
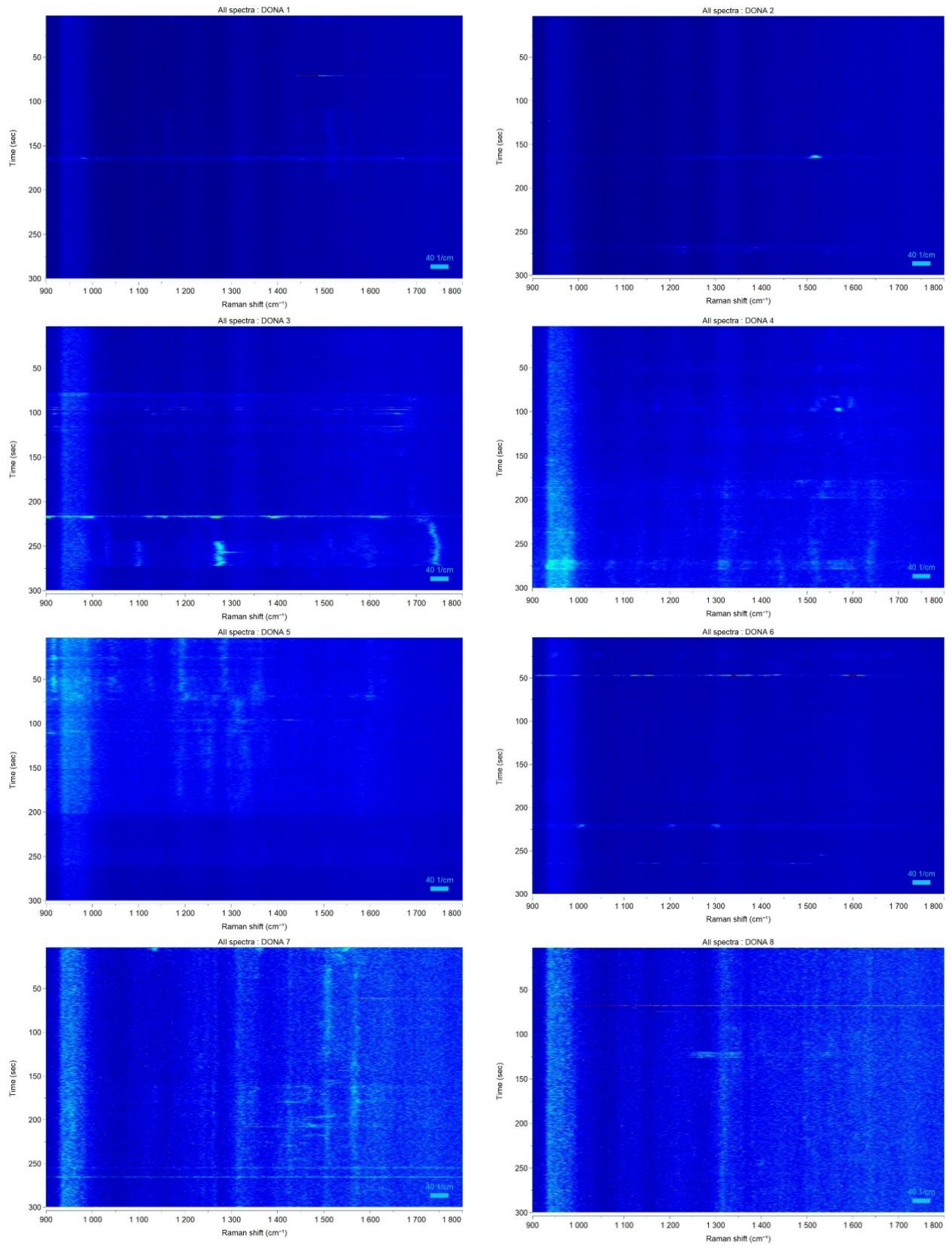
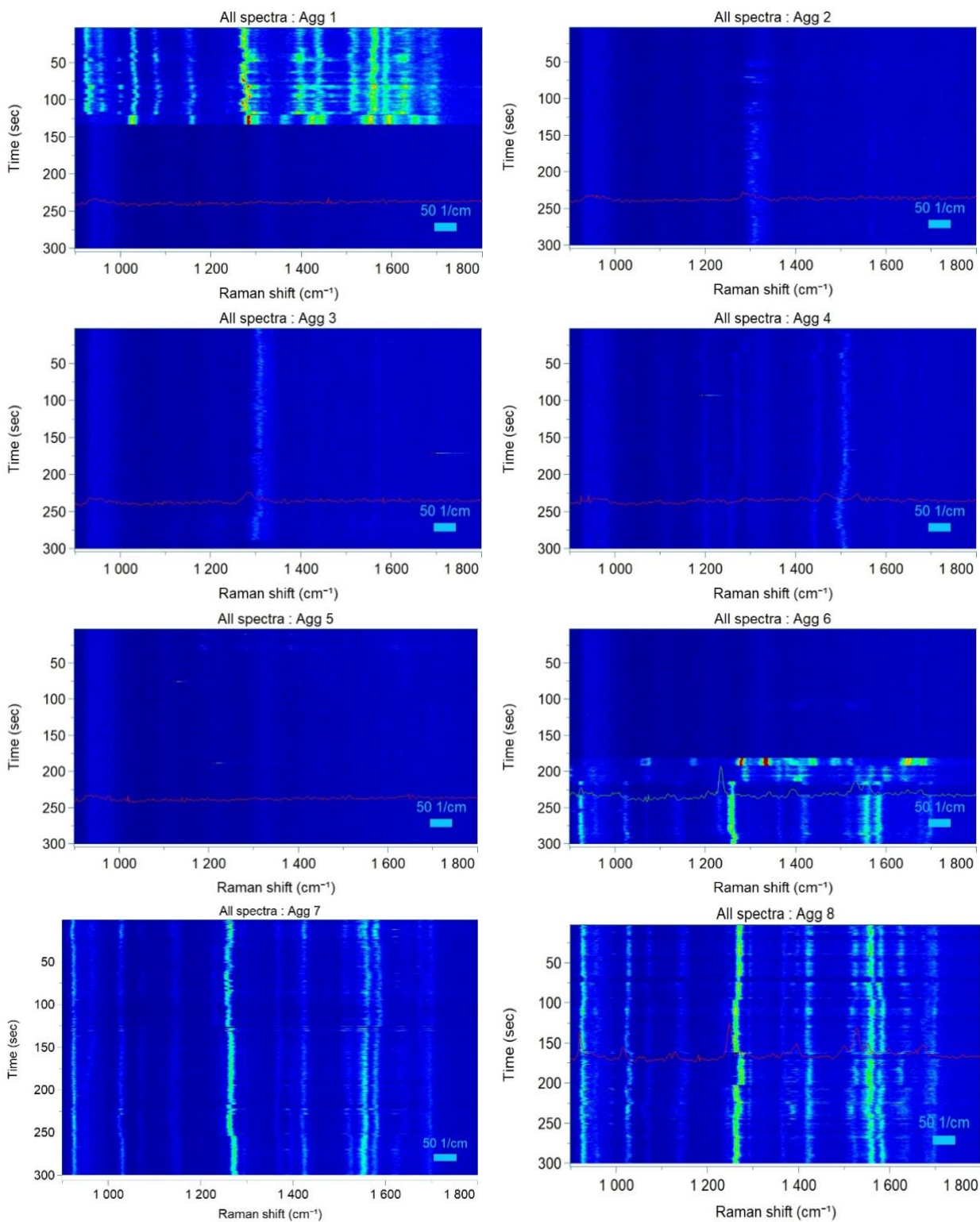*Figure 39 Heat maps of all DONA measurements.*

89

Figure 40 Heat maps of all Aggregate measurements.

List of Publications

- Tapio, K., Mostafa, A., Kanehira, Y., Suma, A., Dutta, A., & Bald, I. (2021). A versatile DNA origami-based plasmonic nanoantenna for label-free single-molecule surface-enhanced Raman spectroscopy. ACS Nano, 15(4), 7065–7077.

- Mostafa, A., Kanehira, Y., Dutta, A., Kogikoski, S., Jr, & Bald, I. (2023). Single-Molecule Surface-Enhanced Raman Scattering Measurements Enabled by Plasmonic DNA Origami Nanoantennas. JoVE (Journal of Visualized Experiments), (197), e65310.

- Mostafa, A., Kanehira, Y., Tapio, K. & Bald, I. From bulk to single-molecule spectra - Surface-enhanced Raman scattering of cytochrome c using plasmonic DNA origami nanoantennas. [Manuscript in preparation]

- Mostafa, A., Shasavar, K., Hosseini, M. & Bald, I. Quantitative SERS based Sandwich-hybridization assay for SARS-CoV2 detection. [Manuscript in preparation]

- Kogikoski, S., Ameixa, J., Mostafa, A., & Bald, I. (2023). Lab-on-a-DNA origami: nanoengineered single-molecule platforms. Chemical Communications, 59(32), 4726–4741.

- Dutta, A., Tapio, K., Suma, A., Mostafa, A., Kanehira, Y., Carnevale, V., … Bald, I. (2022). Molecular states and spin crossover of hemin studied by DNA origami enabled single-molecule surface-enhanced Raman scattering. Nanoscale, 14(44), 16467–16478.

- Kanehira, Y., Tapio, K., Mostafa, A., & Bald, I. The detection of the catalysis reaction from single HRP molecule under the non-resonance excitation condition. [Manuscript in preparation]

- Koopman, W., Titov, E., Sarhan, R. M., Gaebel, T., Schürmann, R., Mostafa, A., … Others. (2021). The Role of Structural Flexibility in Plasmon-Driven Coupling Reactions: Kinetic Limitations in the Dimerization of Nitro-Benzenes. Advanced Materials Interfaces, 8(22), 2101344.

- Schneider, M., Fritzsche, N., Puciul-Malinowska, A., Baliś, A., Mostafa, A., Bald, I., … Taubert, A. (2020). Surface etching of 3D printed poly (lactic acid) with NaOH: a systematic approach. Polymers, 12(8), 1711.

- Schürmann, R., Titov, E., Ebel, K., Kogikoski, S., Mostafa, A., Saalfrank, P., … Bald, I. (2022). The electronic structure of the metal--organic interface of isolated ligand coated gold nanoparticles. Nanoscale Advances, 4(6), 1599–1607.

Tscheuschner, G., Ponader, M., Raab, C., Weider, P. S., Hartfiel, R., Kaufmann, J. O., Mostafa, A … Others. (2023). Efficient purification of cowpea chlorotic mottle virus by a novel peptide aptamer. Viruses, 15(3), 697.

List of Talks and Posters

Talks

DNA 3-periodic weaving, DNA MittelDeutschland, Dresden 2022

SERS for Cytochrome C, DNA MittelDeutschland, Jena 2019

Posters

Yuya Kanehira, Amr Mostafa, Sergio Kogikoski Jr, Ilko Bald, Single molecule detection by DNA origami technique with correlation of Raman and AFM imaging, 2023.

K. Tapio, A . Mostafa , Y. Kanehira , A. Suma , A. Dutta, I. Bald A Versatile DNA Origami Based Plasmonic Nanoantenna for Label Free Single Molecule Surface Enhanced Raman Spectroscopy (SERS), 2021.

A. Mostafa, K. Tapio, A. Dutta, I. Bald, DNA Origami Forks for Single Molecule SERS, 2019.

A. Mostafa, K. Tapio, I. Bald, DNA Encapsulation of Particles, 2019.

Acknowledgement

I would like to express my heartfelt gratitude to the many people who have supported and guided me throughout my journey to complete this PhD thesis.

First and foremost, I extend my deepest appreciation to my advisor, Ilko Bald, for their unwavering guidance, patience, and mentorship. Their expertise and insightful feedback have been invaluable in shaping this thesis and my overall academic growth.

I would like to thank my family for their unending support, encouragement, and understanding during the ups and downs of this challenging journey. Their belief in me kept me motivated and determined to reach this milestone.

My colleagues have been an essential source of inspiration and camaraderie throughout this process. Their encouragement, discussions, and shared experiences have been a vital part of my academic life.

Lastly, I want to acknowledge the countless individuals whose work, publications, and contributions have enriched my research. The academic community and the broader network of scholars have been instrumental in shaping my ideas and perspectives.

This thesis would not have been possible without the collective support and encouragement of all these individuals. Thank you all for being a part of this significant chapter in my life.

Declaration

I declare that this thesis has been composed solely by myself and that it has not been submitted, in whole or in part, in any previous application for a degree. Except where stated otherwise by reference or acknowledgement, the work presented is entirely my own.